Metals and Ceramics Division

Heavy Vehicle Propulsion Materials Program
Quarterly Progress Report for
October through December 2004

D. R. Johnson
Technical Project Manager

Prepared for
U.S. Department of Energy
Assistant Secretary for Energy Efficiency and Renewable Energy
Office of FreedomCAR and Vehicle Technologies Program
VT 05 01 020

Prepared by the
OAK RIDGE NATIONAL LABORATORY
Oak Ridge, Tennessee 37831-6066
Managed by
UT-Battelle, LLC
for the Department of Energy
Under contract DE-AC05-00OR22725

CONTENTS

Materials for Fuel Systems

High Toughness Materials (ORNL)

Materials for Exhaust Aftertreatment

Materials for Exhaust Aftertreatment (Caterpillar Inc.)

Development of NO_x Sensor for Heavy Vehicle Applications (ORNL and Ford Motor Company)

Ultra-High Resolution Electron Microscopy for Characterization of Catalyst Microstructures and De-activation Mechanisms (ORNL)

Catalysts via First Principles (ORNL)

Durability of Particulate Filters (ORNL)

Materials for Air Handling, Hot Section, and Structural Components

Lightweight Valve Train Materials (Caterpillar Inc.)

Cermet Composites for Wear Applications (Cummins Inc.)

Nanoengineered Materials (North Carolina A&T State University)

NDE of Diesel Engine Components (Argonne National Laboratory)

Durability of Diesel Engine Component Materials (ORNL)

Life Prediction of Diesel Engine Components (ORNL and Caterpillar)

Low-Cost Manufacturing of Precision Diesel Engine Components (ORNL)

Advanced Machining and Sensor Concepts (University of Michigan)

Advanced Cast Austenitic Stainless Steels for High-Temperature Components (ORNL and Caterpillar Inc.)

TiAl Nanolaminate Composites (Lawrence Livermore National Laboratory)

High-Density Infrared Surface Treatment of Materials for Heavy-Duty Vehicles (ORNL)

High Temperature Aluminum Alloys (Cummins)

Titanium Alloys for Heavy-Duty Vehicles (ORNL)

Mechanical Behavior of Ceramic Materials for Heavy Duty Diesel Engines (ORNL)

Powder Processing of Nanostructured Alloys Produced by Machining (Purdue University)

Deformation Processes for the Next Generation Ceramics (ORNL)

Synthesis of Nanocrystalline Ceramics (Pennsylvania State University)

Development of Titanium Components for a Heavy-Duty Diesel Engine Turbocharger (Caterpillar Inc.)

Test and Materials Standards

IEA – Rolling Contact Fatigue (ORNL)

IEA Implementing Agreement for a Programme of Research and Development on Advanced Materials for Transportation Applications (ORNL)

Testing Standards (NIST)

Surface Modification of Engineering Materials for Heavy Vehicle Applications (NIST)

Low Cost-High Toughness Ceramics

T. N. Tiegs, F. C. Montgomery, and P. A. Menchhofer
Oak Ridge National Laboratory

Objective/Scope

Significant improvement in the reliability of structural ceramics for advanced diesel engine applications could be attained if the critical fracture toughness (K_{Ic}) were increased without strength degradation. Currently, the project is examining toughening of ceramics by incorporation of ductile intermetallic phases.

Technical Highlights

Previous studies have shown that the properties of the aluminide-bonded ceramics are attractive for diesel engine applications and consequently, development of these materials was started. At the present time, TiC-based composites with 40-60 vol. % Ni_3Al are being developed because they have expansion characteristics very close to those for steel. The development effort is being done in collaboration with CoorsTek, Inc.

A new NiAl commercial source has been identified and powder procured. Characterization of the powder ob x-ray diffraction indicated it was stoiciometric and had a pattern identical to earlier material from a different supplier. Particle size analysis showed the mean particle size was ~9.8 µm, which was similar to the previous material. However, the size distribution was broader than the earlier NiAl.

A large batch of TiC-50 vol. % Ni_3Al has been processed with the new NiAl powder and shipped to CoorTek for injection molding trials. Test parts were fabricated and shipped back to ORNL. Initial sintering results indicated the densification behavior is nearly identical to the earlier composites.

Status of Milestones

On schedule.

Communications/Visits/Travel

None.

Problems Encountered

None.

Publications

None.

Advanced Diesel Aftertreatment Program

Paul W. Park, Herbert DaCosta, Svetlana Zemskova, Christie Ragle and Craig F. Habeger
Caterpillar Inc.

Objective/Scope

The objective of the effort is to develop and evaluate materials that will be utilized in aftertreatment systems for diesel engine applications. These materials include catalysts for NO_x reduction, filtration media for particulate abatement, and materials to improve NO_x sensing capabilities in the exhaust system. This project is part of a Caterpillar strategy to meet EPA requirements for regulated emissions in 2007 and beyond.

This year's focus is to assess durability of various catalyst technologies in terms of phosphorous, sulfur and thermal degradation, to identify diesel particulate trapping materials that have high durability and filtration efficiency, and to develop novel NO_x sensor materials with improved sensitivity and selectivity to comply with future emission regulations for heavy-duty diesel engines.

Technical Highlights

Lean-NO_x. A reductant study over the selected combination catalyst has demonstrated much lower activity when diesel fuel was used as a reductant compared to the desired reductant (dodecane). The influence of diesel fuel components on NO_x reduction performance has been investigated using a bench test system in order to determine the source of the activity loss (test condition: 500 ppm NO_x, 3000 ppm hydrocarbon as C_1, 7% H_2O, 9% O_2, 50 ppm propene, 500 ppm CO and 8% CO_2 with 35,000 h^{-1} space velocity). Mixtures were prepared such as 80% of dodecane and 20% of various organic classes including paraffin, isoparaffin, aromatic, diaromatic, and combinations thereof. Isoparaffins (max. 74% NOx reduction) showed NO_x reduction performance at a similar level to dodecane (77%). Monoaromatics and variations on paraffins had a neutral effect on the NO_x reduction performance. Among the types of reductants tested, diaromatics strongly hindered the performance of the combination catalyst (56%), also shifting the operation temperature to a higher temperature range. Understanding the effects of fuel components provides insight into the development of catalyst materials as well as a fuel processor to obtain the proper reductant from diesel fuel to supply to the catalyst for maximum performance.

***Diesel Particulate Filter (DPF)*.** Collaboration efforts have been initiated with an identified supplier in order to obtain catalyzed and non-catalyzed DPF samples. A non-disclosure agreement (NDA) is in its final stages.

NO_x Sensor. The collaboration with a NO_x sensor developer to evaluate its sensor performance was continued. The sensor has been tested in a bench test system and showed an accurate reading of 20 ppm NO_x in the presence of 1500 ppm CO (CO is known to affect NO_x sensor performance). The results indicated that the sensor has a potential to meet the performance requirement of government regulations (30 ppm NO_x monitoring is mandated by EPA). A test protocol for further evaluation of the NO_x sensor under simulated diesel exhaust environment has been finalized.

Future Plans

1. Capture intellectual properties and document technical reports (Lean- NO_x project).
2. Study catalyst durability (P, S and thermal sintering) of various de NO_x catalyst technologies.
3. Continue searching for and testing new materials for DPF filters.
4. Conduct an accelerated sulfur aging test to identify a degradation mechanism of a NO_x sensor.

Travel

None

Status of FY 2005 Milestones

1. Lean- NO_x project has been completed. The durability study of various catalyst technologies begins.
2. Finalizing non-disclosure agreement with a supplier to obtain samples of its new DPF material.
3. The computational molecular modeling concept has been developed to evaluate NO_x selectivity of a sensor material in the presence of CO and O_2.

Development of NOx Sensors for Heavy Vehicle Applications

Timothy R. Armstrong, David L. West, Fred C. Montgomery
Oak Ridge National Laboratory

CRADA No. ORNL 01-0627
with Ford Motor Company

Objective

The proposed project seeks to develop technologies and materials that will facilitate the development of NOx and ammonia sensors. The development of low-cost, simple NO_x will facilitate the development of ultra-low NO_x emission engines, directly supporting the OHVT goals.

Technical Highlights

- Initiated round robin testing with collaborators by fabricating a large lot (15) of prototype sensing elements.
- Initiated collaboration with 2 universities to study surface of electrode materials with XPS and Raman scattering. Data should shed light on sensing mechanism.
- Modified test equipment and procedures to study effect of H_2O on sensing element performance and stability.
- Demonstrated that one candidate electrode material was unstable under DC electrical bias in the presence of H_2O.
- Discovery points out need for multiple test stands, as degradation occurs slowly over time spans of a week or more.

Future Plans

- Initiate and complete Raman investigation of reaction mechanisms.
- Determine roles of electrode composition and processing in observed H_2O vapor instability.
- Construct 2nd test stand dedicated to long-duration testing.
- Develop rapid screening test for electrode sensitivity to H_2O vapor.
- Investigate use of low-frequency AC bias and its potential for ameliorating electrode instability in the presence of H_2O vapor.

Status of FY 2005 Milestones

(1) Optimize the electrode design (geometry) to maximize output signal. **(03/05)**
(2) Optimize the electrode morphology for the current class of lanthanum chromite electrocatalysts to maximize output signal. **(05/05)**
(3) Evaluate sensor sensitivity to steam and develop protocol to minimize. **(09/05)**

Ford recently indicated during a phone call that milestone 3 is to be the focus of this year's activity. They further indicated that humidity has been the major cause of failure in most NO_x sensors developed to date and they wish us to develop an understanding of humidities effects on our materials immediately.

Communications/Visits/Travel

1. Biweekly teleconferences were initiated this quarter between DOE, Ford, LLNL, and ORNL.

2. A meeting was held at Ford in November with all members attending to discuss technical progress and continue to define the path towards commercialization.

Problems Encountered

None to date.

Publications

1. D. L. West, F. C. Montgomery, and T. R. Armstrong. **"NO-Selective NO_x Sensing Elements for Combustion Exhausts,"** accepted by *Eurosensors XVIII*, Rome, Italy, 2004.

2. D. L. West, F. C. Montgomery, and T. R. Armstrong. **"High-T NO_x Sensing Elements Using Conductive Oxides and Pt,"** *Proceedings of ICEF: Engines for Mobile, Marine, Rail, Power Generation and Stationary Applications*, Long Beach, CA, 2004.

Intellectual Property Filed

NO_x Sensing Devices having Coplanar Electrodes, U. S. Patent filed this quarter

Ultra-High Resolution Electron Microscopy for Characterization of Catalyst Microstructures and De-activation Mechanisms

L.F. Allard, D.A. Blom, D.W. Coffey, C.K. Narula, M.A. O'Keefe and J. Hoard
Oak Ridge National Laboratory

Objective/Scope

The objective of the research is to characterize the microstructures of catalyst materials of interest for the treatment of NO_X emissions in diesel and lean-burn gasoline engine exhaust systems. The research heavily utilizes new capabilities and techniques for ultra-high resolution transmission electron microscopy (UHR-TEM). The research is focused on understanding the effects of reaction conditions on the changes in morphology of heavy metal species on "real" catalyst support materials (typically oxides). These changes are being studied utilizing samples treated in both steady-state bench reactors and a special *ex-situ* catalyst reactor system especially constructed to allow appropriate control of the reaction. Samples of vehicle-tested lean NO_x-trap catalysts (LNT) and diesel particulate NO_x reduction (DPNR) catalysts provided by research partners such as Ford Research Laboratories are also being studied to determine the effects of vehicle aging on catalyst morphology and chemistry.

Technical Progress

In collaboration with Dr. John Hoard of Ford Research Laboratory, and colleagues at the National Transportation Research Center including Drs. Stuart Daw, Bill Shelton and Jim Parks, we are characterizing LNT and DPNR catalysts taken from Toyota Avensis 2.0-litre D-4D turbo diesel vehicles, and a LNT GDI catalyst marketed by Umicore Co. Toyota's new Avensis is the first vehicle where all engines, including diesel, comply with the new EURO IV emissions standards. It also introduces "D-CAT," Toyota's new concept in clean diesel technology, which makes the D-4D even cleaner - well within the EURO IV standards. "Fresh" (as received) samples were characterized, prior to the subsequent examination of samples to be "de-greened" using a bench-top reactor, and finally samples treated under systematic aging conditions. Microstructural results from the Fresh catalysts are reported here.

Monolith core samples were mounted in epoxy, with the "downstream" face exposed, and were polished using standard metallographic techniques. Thin slices (<500μm) were cut from the polished faces, and used for preparation of ion-milled TEM thin sections. The remaining epoxy-mounted specimens were re-polished and submitted for quantitative analysis using electron microprobe techniques.

The TEM samples were examined in the HTML's Hitachi HF-2000 field emission TEM and in HD-2000 dedicated scanning transmission electron microscope (STEM). Preliminary backscattered electron images were recorded using the JEOL 8200 electron

microprobe, prior to full quantitative compositional analysis (to be reported in the next quarterly).

Figure 1-3 show backscattered electron images at two magnifications each of the three Fresh samples. In these images, the higher atomic number phases show brighter

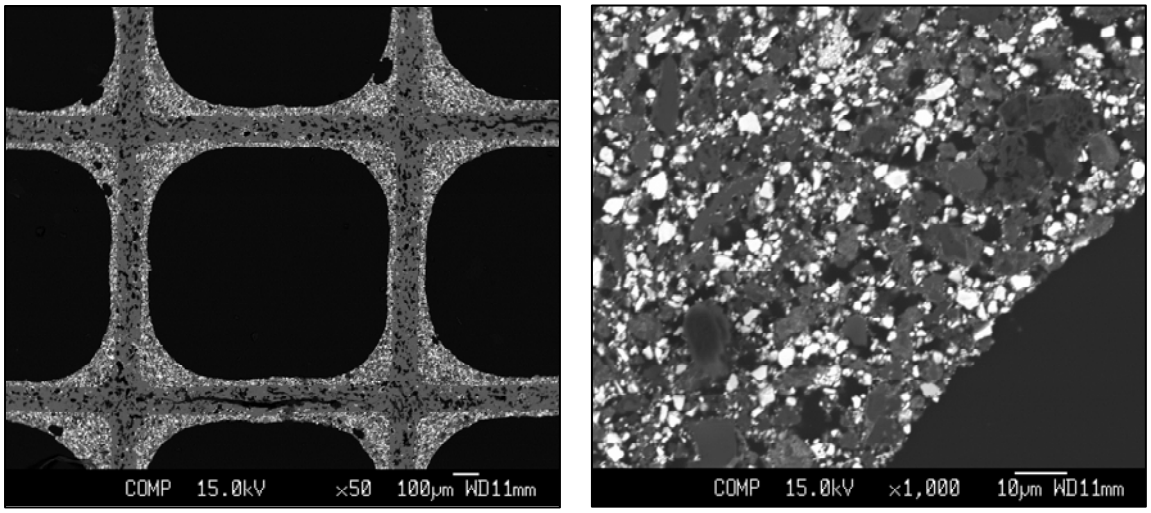

Fig. 1 Umicore GDI LNT "Fresh"

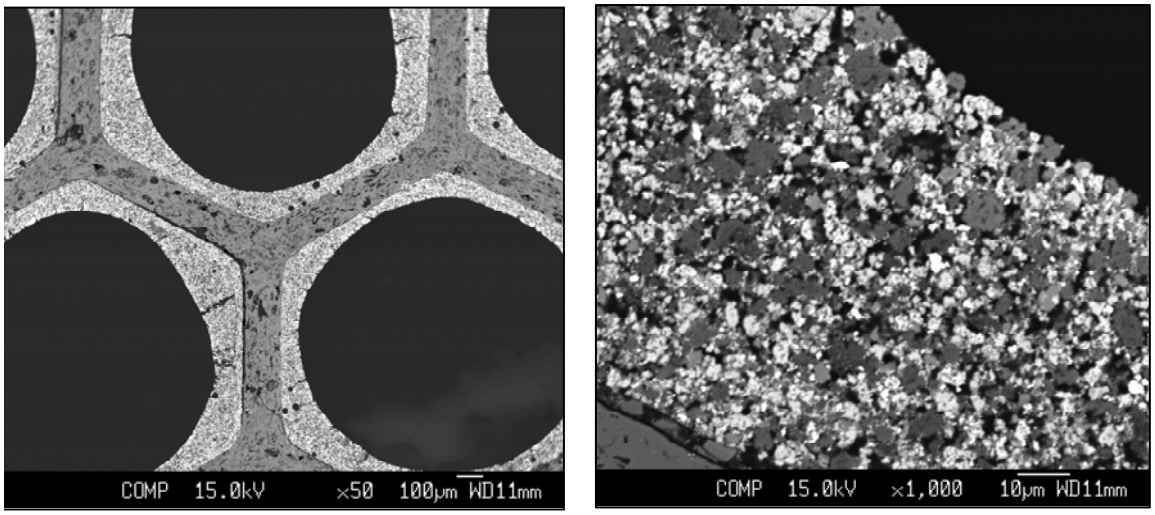

Fig. 2 Toyota "D-Cat" LNT "Fresh"

contrast than lower average atomic number phases. Note that the LNT catalysts from both Umicore and Toyota show a structure of a single-layer washcoat on the monolith, but that the Toyota LNT structure has a hexagonal-shaped cell. This gives a more uniform thickness of washcoat material around the circumference of the channel, rather than a thick coating in the corner and thinner washcoat on the side walls as found in the square-shaped cell structure. The unique feature of the Toyota DPNR catalyst is that the monolith has a very porous structure, and the washcoat is actually totally contained within the pores of the monolith. Also noted it that the washcoat of the DPNR catalyst

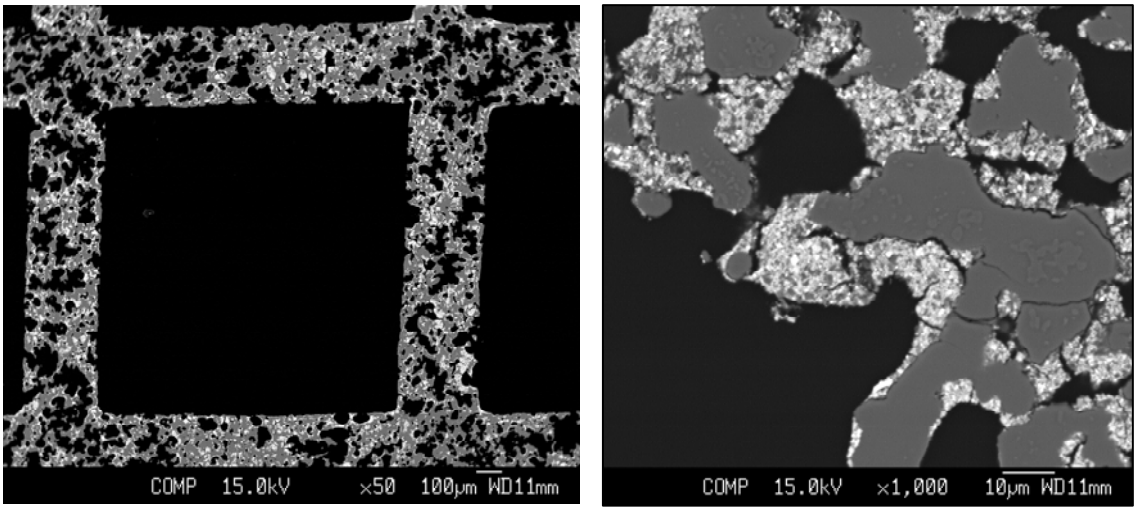

Fig. 3 Toyota “D-Cat” DPNR “Fresh”

has an extremely fine grain size with respect to the LNT catalysts. The LNT catalyst washcoat shows three primary phases: a light grey phase, a dark grey phase, and a bright white phase in the BSE images. Details of the ultrastructure of these phases, and of the distribution of platinum in the washcoat structure were obtained from electron microscopy of the Umicore LNT sample.

Figure 4a and 4b are bright-field TEM images of the washcoat of the Umicore sample. Energy-dispersive x-ray spectra from areas A, B, and C are shown in Fig. 5a-c, respectively. The fine-grain area A is primarily alumina, with a significant Mg composition. Area B is coarser grained, and the dark contrast in the BF TEM image is consistent with its composition, cerium-rich ceria-zirconia. Area C is typical of a medium-grain-size alumina-baria composition. Relative to the BSE images from the

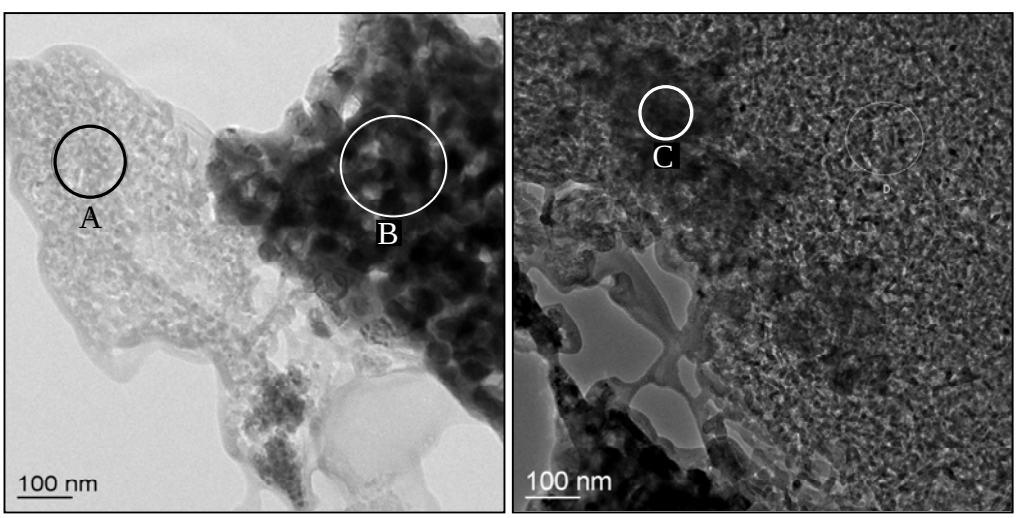

Fig. 4 a, b) Bright-field TEM images of Umicore LNT thin section. The respective phase compositions are given in the EDS spectra of Fig. 5.

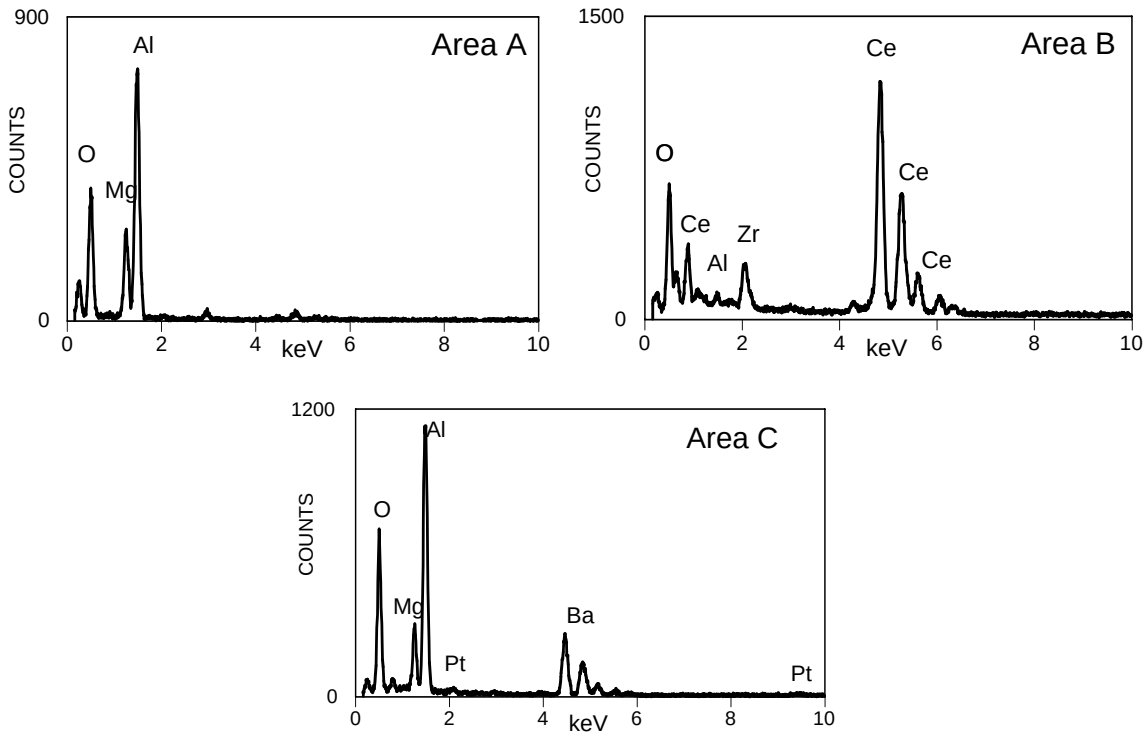

Fig. 5 EDS spectra showing A) alumina-magnesia composition of fine-grained phase in Fig. 4; B) ceria-zirconia composition of coarse-grained phase; C) alumina-baria composition of medium-grained phase.

electron microprobe, the alumina phase is the dark-grey phase, the alumina-baria phase is the medium-grey phase, and the ceria-zirconia phase is the phase in brightest contrast.

The catalytically active phase in the Umicore sample was determined to be primarily Pt, as indicated by the EDS spectrum of Fig. 6, a long acquisition time from an area of the alumina phase. However, it was difficult to determine from BF TEM images exactly the size and distribution of the Pt particles/clusters, so the Umicore sample was examined using the new JEOL 2200FS-AC aberration-corrected electron microscope (ACEM). Figure 7 is an annular dark-field image of an area of baria-alumina and alumina phases

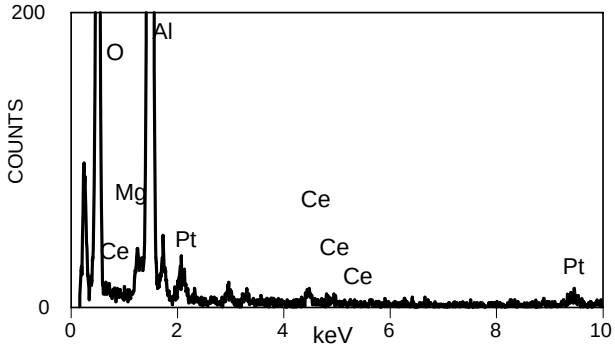

Fig. 6 EDS spectrum from alumina phase shown on expanded vertical scale to show presence of Pt catalytic species.

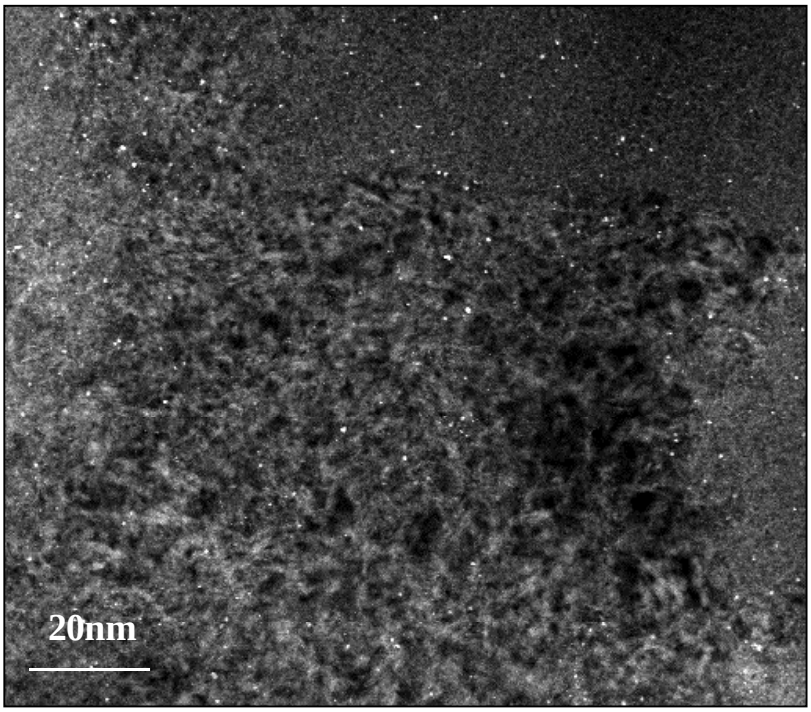

Fig. 7 Annular dark-field (ADF) image of area of baria-alumina and alumina (upper left) phases in Umicore LNT sample, showing Pt particles in bright contrast.

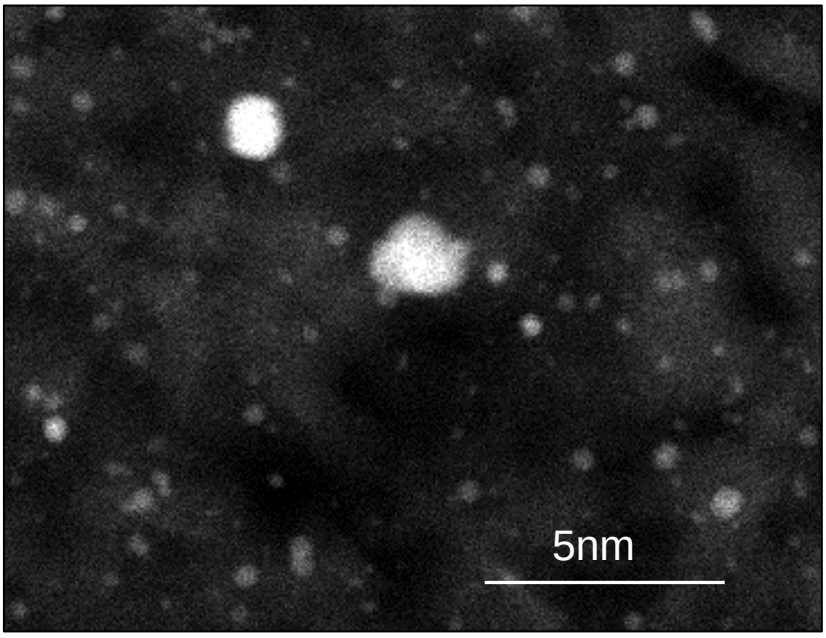

Fig. 8 ADF image at high resolution showing larger (1-2nm) Pt particles, and uniform distribution of fine Pt clusters down to the level of single atoms.

showing particles of Pt in bright contrast (due to high atomic number). The Pt particles are evenly distributed in both phases, and are about 1-2nm in average size. However, at highest resolution (in the range of 0.1nm for the image) as in Fig. 8, it is clearly seen that Pt species are present in very small clusters, even down to single atoms. It is only with the exceptional resolution provided by the new ACEM in dark-field mode that images such as these can be recorded showing the actual distribution and size of catalytic species. The Pt catalyst particles were found primarily in the alumina and baria-alumina; in further work a systematic determination will be made to confirm the distribution of Pt (and any other heavy-metal species found) within the various washcoat components.

Status of Milestones

On schedule

Communications/Visits/Travel

None this period

Publications

"HRTEM Imaging of Atoms at Sub-Ångström Resolution," M. A. O'Keefe, L. F. Allard and D. A. Blom, submitted for publication to *Journal of Electron Microscopy*, Special Issue in Memory of Prof. John M. Cowley

References

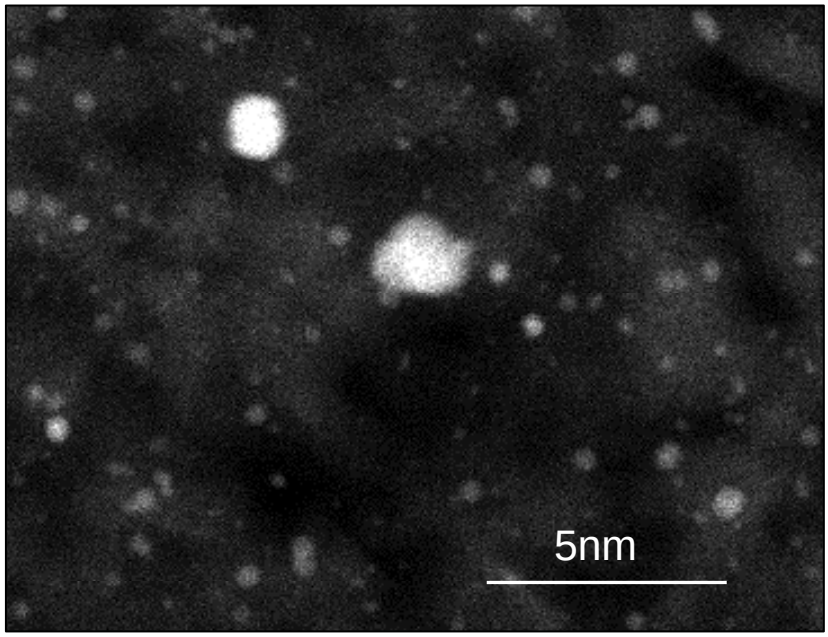

Fig. 8 ADF image at high resolution showing larger (1-2nm) Pt particles, and uniform distribution of fine Pt clusters down to the level of single atoms.

Catalysts via First Principles

(Can Theoretical Modeling and Experiments Play a Complimentary Role in Catalysis?)

C. Narula, W. Shelton, Y. Xu, M. Moses, L. Allard
Oak Ridge National Laboratory
Prof. B. Gates, University of California, Davis
Prof. W. Schneider, University of Notre Dame

Objective/Scope

This research focuses on an integrated approach between computational modeling and experimental development, design and testing of new catalyst materials, that we believe will rapidly identify the key physiochemical parameters necessary for improving the catalytic efficiency of these materials.

The typical solid catalyst consists of nano-particles on porous supports. The development of new catalytic materials is still dominated by trial and error methods, even though the experimental and theoretical bases for their characterization have improved dramatically in recent years. Although it has been successful, the empirical development of catalytic materials is time consuming and expensive and brings no guarantees of success. Part of the difficulty is that most catalytic materials are highly non-uniform and complex, and most characterization methods provide only average structural data. Now, with improved capabilities for synthesis of nearly uniform catalysts, which offer the prospects of high selectivities as well as susceptibility to incisive characterization combined with state-of-the science characterization methods, including those that allow imaging of individual catalytic sites, we have compelling opportunity to markedly accelerate the advancement of the science and technology of catalysis.

Computational approaches, on the other hand, have been limited to examining processes and phenomena using models that had been much simplified in comparison to real materials. This limitation was mainly a consequence of limitations in computer hardware and in the development of sophisticated algorithms that are computationally efficient. In particular, experimental catalysis has not benefited from the recent advances in high performance computing that enables more realistic simulations (empirical and first-principles) of large ensemble atoms including the local environment of a catalyst site in heterogeneous catalysis. These types of simulations, when combined with incisive microscopic and spectroscopic characterization of catalysts, can lead to a much deeper understanding of the reaction chemistry that is difficult to decipher from experimental work alone.

Thus, a protocol to systematically find the optimum catalyst can be developed that combines the power of theory and experiment for atomistic design of catalytically active sites and can translate the fundamental insights gained directly to a complete catalyst system that can be technically deployed.

Although it is beyond doubt computationally challenging, the study of surface, nanometer-sized, metallic clusters may be accomplished by merging state-of-the-art, density-functional-based,

electronic-structure techniques and molecular-dynamic techniques. These techniques provide accurate energetics, force, and electronic information. Theoretical work must be based electronic-structure methods, as opposed to more empirical-based techniques, so as to provide realistic energetics and direct electronic information.

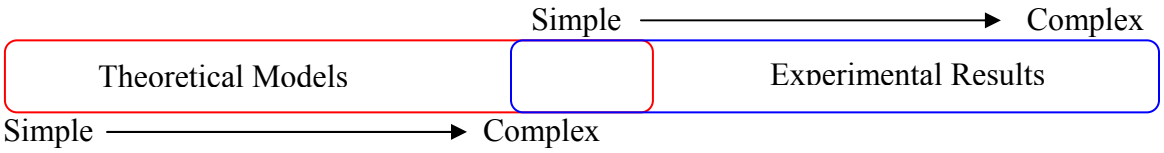

A computationally complex system, in principle, will be a model of a simple catalyst that can be synthesized and evaluated in the laboratory. It is important to point out that such a system for experimentalist will be an idealized simple model catalyst system that will probably model a "real-world" catalyst.

Thus it is conceivable that "computationally complex but experimentally simple" system can be examined by both theoretical models and experimental work to forecast improvements to obtain optimum catalyst systems.

Our Goals are as follows:

- Our initial theoretical goal will be to carry out the calculation and simulation of realistic Pt nanoparticle systems (i.e., those equivalent to experiment), in particular by addressing the issues of complex cluster geometries on local bonding effects that determine reactivity. As such, we expect in combination with experiment to identify relevant clusters, and to determine the electronic properties of these clusters.
- Our initial experimental goal will be to prepare metal carbonyl clusters, decarbonylated metal clusters, sub-nanometer metal particles, and metallic particles (~5nm) on alumina (commercial high surface area, sol-gel processed, and mesoporous molecular sieve). We will then evaluate these systems for CO-conversion efficiencies to determine the species that participates in CO-oxidation.

Technical Highlights

Platinum-Alumina System:
A variety of Pt clusters ($[Pt_{15}(CO)_{30}]^{2-}$, $[Pt_6(CO)_{12}]^{2-}$, $[Pt_9(CO)_{18}]^{2-}$) on MgO are known but not on aluminas [1]. We plan to prepare these clusters on a variety of aluminas (commercial γ–alumina, sol-gel alumina [2], and molecular sieve alumina [3]). We will also prepare decarbonylated clusters, nanoclusters (~10nm) and metallic particles (100nm) on thse alumina. We have initiated our efforts in the synthesis of these materials and have isolated nanocluster Pt/commercial γ–alumina. Thermal treatment of this material furnishes metallic Pt/ commercial γ–alumina.

The Density Functional Theory code DACAPO has been used to study the trends in the oxidation behavior of Pt systems that range from gas-phase clusters to the bulk and in the adsorption of atomic and molecular species relevant to this project, including O, O_2, and CO. Pt

systems studied so far include gas-phase Pt, Pt_2, Pt_3, Pt_4, Pt_{10}, as well the Pt(111) and Pt(211) surfaces, the former being a close-packed flat facet of the bulk fcc lattice, and the latter being a model of step edges and defects.

Partially oxidized Pt systems are defined here as those that have a stoichiometry of 1 Pt : 1 O (i.e., Pt_xO_x). The energy of the PtO unit is found to decrease (i.e., energy becoming more negative and system more stable) with increasing system size, from PtO, Pt_2O_2, to bulk PtO. The data available right now form a smooth, continuously decreasing function (energy vs. the total number of O atoms). On the other hand, the heat of formation of the oxides with respect to the most stable pure Pt systems of the corresponding sizes (i.e., PtO with respect to Pt, Pt_2O_2 with respect to Pt_2, and bulk PtO with respect to bulk Pt) is found to increase (i.e., becoming less exothermic) with increasing system size. With respect to the O_2 molecule, the oxidation energy ranges from -1.52 eV/O for PtO to -0.43 eV/O for bulk PtO (spanning ~1.1 eV). When the oxidation energies are plotted against the total numbers of O atoms in the systems studied, a rising curve is thus observed, with Pt_2O_2 bucking the trend.

The fully oxidized Pt systems (Pt_xO_{2x}) studied so far exhibit very similar behavior. The energy of the PtO_2 unit also decreases with increasing system size, and the heat of formation increases from -1.65 eV/O for PtO_2 to ~-0.6 eV/O for bulk PtO_2, again spanning ~1.1 eV.

From available data, it appears that for the Pt_xO_x clusters it is preferable to attach O atoms to the outside of the cluster so that no Pt-Pt bond is broken, whereas for the Pt_xO_{2x} clusters it is more favorable to insert O atoms in between the Pt atoms, thus partially or completely severing the Pt-Pt bonds. The trend for Pt_xO_x will likely be broken when a Pt cluster gets sufficiently large, because then some Pt atoms will no longer be exposed and thus would not be directly available to bind O atoms. In that case the structure of the cluster will have to change substantially even upon partial oxidation.

The adsorption energy of a single O atom decreases (i.e., becoming more exothermic) as the size of the Pt cluster increases. The trend must undergo a reversal because the adsorption energy of O on an extended Pt surface (value on (211) surface used) is lower than on a single Pt atom. The point of reversal is unknown due to insufficient data. There are also insufficient data for conclusively identifying trends in O_2 and CO adsorption. For CO, its adsorption energy roughly increases with system size. Both O_2-Pt_2 and CO-Pt_2 appear to buck the respective trends.

$H_3Re_3(CO)_{12}/\gamma$-Al_2O_3 System:

We initiated this work by successfully synthesizing $H_3Re_3(CO)_{12}$ by using literature methods and confirmed its formation by IR spectroscopy [4]. The γ-Al_2O_3 support, acquired from Degussa, was mixed with DI water and dried for 24 h at 393 K. This was followed by calcination at 773 K under flowing O_2 for 2 h followed by evacuation for 14 h at the same temperature. This support was then brought in contact with $H_3Re_3(CO)_{12}$ in *n*-pentane solution, giving a sample with 1 wt% Re after evacuation of the solvent. The $H_3Re_3(CO)_{12}/\gamma$-Al_2O_3 was then treated under flowing H_2 at 673 K, resulting in complete removal of CO ligands and formation trirhenium clusters [5]. All the synthesis procedures were done under inert atmospheres.

The IR spectra of the sample formed after adsorption of the precursor on partially dehydroxylated γ-Al_2O_3 match the one reported for the $H_3Re_3(CO)_{12}$ itself, indicating the presence of the intact precursor on the support surface. IR spectroscopy was used to follow decarbonylation of this sample in H_2; the removal of the CO ligands was followed as the temperature was raised, and at 673 K, the Re was completely decarbonylated.

The structural parameters determined for the as-prepared sample are consistent with the presence of the intact precursor $H_3Re_3(CO)_{12}$ on the support, consistent with the IR data. EXAFS spectroscopy was measured as this sample was decarbonylated in H_2 at 673 K. The EXAFS parameters support the IR results indicating complete decarbonylation of the rhenium. The data indicate the formation of trinuclear Re rafts, Re_3. The decarbonylated samples, modeled as trirhenium rafts, are shown by the XANES data to incorporate electron-deficient (cationic) rhenium. On the basis of a comparison of the observed XANES signature with various XANES of various reference materials, we tentatively identify the oxidation state of Re to be +4.

These samples will be examined by high-resolution TEM and by aberration corrected electron microscope (ACEM) at ORNL.

Next Steps:
We plan to carry out following tasks:

1. Synthesize sol-gel and molecular sieve alumina, silica, and magnesia. Prepare Pt, Rh, Re clusters on these substrate and decarbonylate them. Prepare nanoclusters of Pt, Rh, and Re also on these substrates.
2. Try to resolve the apparent dependence of total energy as well as adsorption energy on the size of the unit cell used in the calculation. Use NWChem or some other quantum chemistry code to verify energy and electronic states of key species. Use MD to perform coarse-grain calculations to tackle the larger systems, such as Pt_4O_8, $Pt_{10}O_{10}$, and $Pt_{10}O_{20}$. Try to decide on a Pt oxide model (involving OH or not?) and start to study the adsorption of O, CO, and O_2 on Pt oxide clusters.

Other Activities
The synthesis laboratory has been equipped to enable preparation materials under inert atmosphere to enable preparation of cluster materials as well as materials by sol-gel type processes. Melanie Moses, a post-doctoral student with C. Narula has started working on synthesis of substrate materials. Ye Xu, a post-doctoral student with W. Shelton and W. Schneider, joined the group in October 2003 and is carrying out theoretical calculations. Vinesh A. Bhirud, a post-doctoral fellow with B. Gates, is synthesizing new clusters based on rhenium.

Communication/Visitors/Travel
W. Schneider visited ORNL to present a seminar and discuss theoretical work in support of this program. B. Gates will present a paper entitled "γ–Al_2O_3-Supported Trirhenium Rafts: Spectroscopic and Microscopic Characterization" at the American Catalysis Society meeting in Philadelphia, May 21-28, 2005.

References
1. Gates, B.C., Chem. Rev., 1995, 95, 511

2. Narula, C.K.; Nakouzi, S.R., Wu, R., Goralski, C.T., Allard, L.F., AIChE Journal, 2001, 47, 744.
3. Deng, W.; Toepke, M.W., Shanks, B.H. Adv. Func. Mater., 2003, 13, 61.
4. Andrews, M. A., Kirtley, S. W., Kaesz, H. D., *Inorg. Synth.* **1977**, 17, 16.
5. Fung, A. S., Tooley, P. A., Kelley, M. J., Koningsberger, D. C., Gates, B. C. *J. Phys. Chem.* **1991**, 95, 225.

Durability and Reliability of Ceramic Substrates for Diesel Particulate Filters

Edgar Lara-Curzio, Amit Shyam, Claire R. Luttrell and H-T. Lin
Oak Ridge National Laboratory

Objectives/Scope

To develop/implement test techniques to characterize the physical and mechanical properties of ceramic Diesel particulate filters (DPFs). To implement a probabilistic-based analysis to quantify the durability and reliability of DPFs.

Highlights

A round-robin testing program was organized to determine the precision in the determination of the flexural strength of cordierite DPFs. Participants included Cummins, Corning and ORNL.

Technical Progress

During the reporting period a round-robin testing program was organized to determine the precision in the determination of the 4-pt flexural strength of Corning-made cordierite DPFs. Program participants included Cummins, Corning and ORNL. Each laboratory was responsible for testing forty test specimens with nominal dimensions of 100 mm x 26 mm x 13.5 mm. Tests were carried out at ambient conditions under a constant crosshead displacement of 0.25 mm/min using inner and outer spans of 19 and 89 mm. Figure 1 shows the experimental set-up. The test results, which were analyzed using Weibull statistics, are presented in Figure 2. It was found that the average and standard deviation of all tests were 24.16 and 2.19 MPa, respectively and that the repeatability and reproducibility standard deviations were 1.2 and 2.5 MPa, respectively. The Weibull modulus, which was determined according to the maximum likelihood method, was found to be 24.1

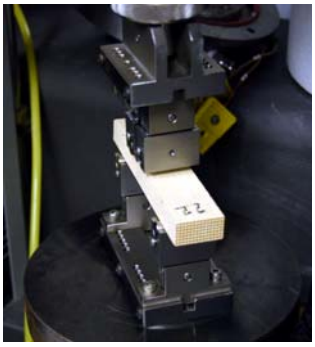

Figure 1. Experimental set-up used to evaluate the flexural strength of cordierite cellular test specimens

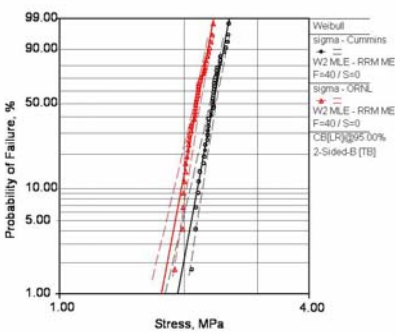

Figure 2. Distribution of flexural strengths for cordierite cellular test specimens obtained by two of the participants.

Milestones

To organize a round-robin testing program to determine the precision in the determination of flexural strength of cordierite cellular ceramics used as DPFs. June 2005. (Completed)

Meetings

A meeting was held on January 26, 2005, in Cocoa Beach, FL, to review the CRADA program between ORNL and Cummins. In attendance were personnel from Cummins, Corning and ORNL.

Lightweight Valve Train Materials

Jeremy S. Trethewey, John. A. Grassi, and Matt P. Fletcher
Caterpillar Inc.

Introduction

Valve train components in heavy-duty engines operate under high stresses and temperatures, and in severe corrosive environments. In contrast, the valve train components in the light-duty engine market require cost-effective reliable materials that are wear resistant and lightweight in order to achieve high power density. For both engine classes, better valve train materials need to be identified to meet market demand for high reliability and improved performance while providing the consumer lower operating costs.

Advanced ceramics and emerging intermetallic materials are highly corrosion and oxidation resistant, and possess high strength and hardness at elevated temperatures. These properties are expected to allow higher engine operating temperatures, lower wear, and enhanced reliability. In addition, the lighter weight of these materials (about 1/3 of production alloys) will lead to lower reciprocating valve train mass that could improve fuel efficiency. This research and development program is an in-depth investigation of the potential for use of these materials in heavy-duty engine environments.

The overall valve train effort will provide the materials, design, manufacturing, and economic information necessary to bring these new materials and technologies to commercial realization. With this information, component designs will be optimized using computer-based lifetime prediction models, and validated in rig bench tests and short-and long-term engine tests.

Program Overview

Information presented in this report is based on previous proprietary research conducted under Cooperative Agreement DE-FC05-97OR22579.

Ceramic Materials

Silicon nitride materials have been targeted for valve train materials in automotive and diesel industries since the early 1980's. Some silicon nitride material grades have reached a mature level of materials processing, and are capable of being implemented into production. Commercial realizations have been reported in both automotive and diesel valve trains, with large-scale production underway. The silicon nitride valve train components in production are used in high rolling contact stress applications and have exhibited superior wear resistance, and longevity.

Intermetallic Materials

Titanium aluminide based intermetallics retain their strength to elevated temperature and are highly corrosion-resistant. They are lightweight, and posses high fracture toughness. These alloys are actively being investigated for several aerospace and automotive applications.

Summary

Engine Testing of Silicon Nitride, TiAl and Production Valves

Arrangements have been made to perform engine tests at the National Transportation Research Center (NTRC) located in Oak Ridge, TN. These tests will be executed with the intention to compare valve performance and reliability of advanced materials to current production materials. The engine

platform that the valves will be tested in is the Caterpillar G3406 Natural Gas genset. A G3406 cylinder head was procured and instrumented for these tests. It was outfitted with 32 thermocouples embedded in four intake and four exhaust valve seat inserts. Pressure transducers were installed in each of the six cylinders, the intake manifold and exhaust manifold. The head was shipped to NTRC for installation in the G3406 engine in early January 2005.

A test plan has been generated to evaluate Silicon Nitride, Titanium Aluminide and production valves performance in parallel. The material responses that will be studied are as follows: wear rates will be evaluated via profilometry and micrographic analysis; crack initiation and propagation will be evaluated using J.G. Sun's NDE laser scattering technique and ultrasonic NDE; deposition formation will be evaluated via chemical analysis. The valves will be evaluated at various time intervals while accumulating 1000 hrs. of engine test exposure.

Forty-eight silicon nitride valve blanks will be finish machined to tolerance by the end of 1Q05. As previously reported, a supplier error resulted in incorrect finish machining. Two finish machining suppliers are being considered to perform corrective finish machining to meet the original print specifications. Request for quotes have been delivered and a response is expected early 1Q05. A subset of these valves will be used in the G3406 engine test while others will be directly fractured to obtain baseline strength data.

In 2004, ten γ-TiAl valve head blanks were formed and successfully friction welded to Ti-6V-4Al valve stems. Finish machining had been delayed in order to determine correct finishing specifications. Now that specifications have been determined, the prototype valves will be finish machined and returned to Caterpillar in 1Q05. These valves will be used in the G3406 engine test.

Life Prediction of Ceramic Valves

In order to rigorously evaluate the performance of a component made from a brittle material it is necessary to consider the component's lifetime as a function of thermal stresses, mechanical stresses, the cyclic nature of the stresses and number of cycles. With Caterpillar's input, Jadaan Engineering & Consulting has been developing a lifetime prediction model (using NASA/CARES) for a silicon nitride valve subjected to the typical stresses seen in a G3406 engine environment. A FEA model of a modified silicon nitride valves has been provided along with the material's statistical mechanical properties (collected in the specimen tests performed in 2003 and 2004).

Initial results show that the steady-state thermal stresses (with minimal mechanical induced boundary conditions) account for moderate stresses in the fillet region due to the valve head's tendency to dome. After this initial thermal analysis, steady-state mechanical boundary conditions were included (i.e. constant cylinder pressure). The result of the fast fracture probability analysis revealed that under **constant** stress there is essentially zero probability of failure. The next step will be to perform a **transient** reliability analysis that will simulate the cyclic nature of the mechanical loading. This is expected to substantially increase the probability of failure. Results from the transient analysis are expected in 1Q05.

Test Rig Evaluation of Advanced Material Valves

The valve bench rig continues to extend the impact and wear study for the baseline production valves. Over 200 hours have been accumulated on a set of production valves. The intent is to evaluate baseline valve performance to correlate the wear rate of current production valves to the wear rate of

advanced materials. Modifications (i.e. custom valve seat inserts, custom bridge and head modifications) were designed such that the valve bench may accept natural gas valves in addition to the current diesel valves.

A second valve test rig capable of simulating cyclic thermal and combustion loads has been relocated internally at the Caterpillar Technical Center. This test rig, designed and built at Caterpillar, can accommodate 3400 and 3500 series engine valves. The rig is designed to apply a cyclical hydraulic load to the valve face to simulate the combustion pressure loading and unloading. The rig uses standard Caterpillar seat insert components, and can allow various seat-to-valve offsets to simulate seat angle misalignment. The rig can also apply a cyclic thermal load through induction heating to metallic valves. Full installation and operator training will be completed by mid 1Q05.

Valve Seal Performance Investigation

Silicon nitride and production valve stem samples were prepared and sent to a valve stem seal supplier for compatibility testing of the valve materials with valve stem seals. In 2004, rig testing with silicon nitride valves revealed that the elastomer used in the valve stem seals was torn away. The supplier will run trials with the stems to evaluate material compatibility between the advanced valve materials and the elastomer used in their valve stem seals. The supplier will also quantify the level of oil blow-back (leakage) in the standard and advanced materials.

Cermet Composites for Wear Applications

R. J. Stafford
Cummins Inc.

Objective/Scope

TiC/Ni_3Al is a composite of TiC powder in a Ni_3Al matrix which was developed in collaboration with Oak Ridge National Laboratory (ORNL) and CoorsTek. Its composition was established to match the unique properties required for Cummins Fuel Systems applications. CoorsTek and ORNL have developed the processing methods to make the material, while Cummins has been responsible to finding an application for it and testing the material as fuel system components and evaluating their performance versus other materials. The objectives of this work are to characterize the material and optimize the composition and processing. Specific objectives are:

- Optimize injection molding binder composition and sintering cycles to achieve 99+% density. This will include the determination of the shrink rate during sintering for prototype tool construction and demonstration.
- Determine production viable sources for all raw components in the composition.
- Test prototype components in intended application on Cummins' fuel system test rigs to show viability of material in an application.

Approach

- A prototype injection-molding tool of a proposed Cummins Fuel Systems component will be made and test pieces of the TiC/Ni_3Al cermet will be produced to near-net shape for evaluation of shrinkage, microstructure uniformity, and density.
- Prototypes machined from isostatically pressed rods of the TiC/Ni_3Al cermet will be tested on abuse tests at Cummins Fuel Systems.
- Production source for NiAl powder will be identified and processing parameters for the new powder determined to ensure the properties of the final composition do not vary from the properties of the composition using the original NiAl powder.

Technical Highlights

Ni_3Al/TiC Composite

Testing and pending approval of a new source of the critical NiAl raw material from Accumet is underway. ORNL (Tiegs) has sintered test parts from first prototype design successfully to the same density as the previous material (from X-Form, now out of business). A test lot of powder has been processed through milling at ORNL, compounded into feedstock, molded and debound at CoorsTek, it is waiting for a new sintering trial at Colorado School of Mines (CSM). Some initial parts sintered at CSM were 97.7% dense; whereas, the parts sintered at ORNL were 98.8% dense.

From these tests, we will measure a final shrinkage to create the mold for the revised prototype part. The part was redesigned to add stock for fixturing during the finish grinding operations at Cummins.

.

Additional rig testing of the parts machined from isostatically pressed rods may be complete, however, information on the results is not yet available.

Future Work

Analysis of test results from rig tests using parts machined from isostatically pressed rods.

Compounding new powder lot with Accumet NiAl powder, molding using new tooling, debinding and sintering prototype parts at CoorsTek.

Finish grinding, assembly and rig testing of new prototype parts at Cummins.

.

Processing and Characterization of Structural and Functional Materials for Heavy Vehicle Applications

J. Sankar, Z. Xu, and S. Yarmolenko
North Carolina A & T State University

Objective/Scope

Study electrophoretic deposition technique for YSZ coatings as the electrolyte for solid oxide fuel cells (SOFCs).

Task

Deposit YSZ thin films using electrophoretic deposition technique on the substrates of stainless steel. Study the deposition behavior in the different suspensions.

Technical Highlights

Electrophoretic deposition (EPD) is a process in which the charged particles in an appropriate solvent move under the influence of the direct electric field towards an oppositely charged electrode and coagulate thereon to form a stable deposit. In the past research and applications, it was used to prepare ceramic laminates [1, 2], components in electrochemical cells [3], and ceramic superconductors [4], etc. It was recently introduced to the area of the manufacturing SOFCs, since thin film electrolytes are highly desired for the fuel cells to work at reduced temperatures and higher efficiencies. This deposition technique is especially attractive for SOFC application owing to simple, low cost equipment and ease of deposition of films of controlled thickness on substrates with even complex shape.

The suspensions were prepared by dispersing the powders in the mixture of two organic solvents, i.e., acetylacetone and ethanol at different ratios ranging from pure acac to pure ethanol. The powder concentrations used were 5, 10, 25, and 40g/l. All the suspensions were subjected to ball milling for 48 h and ultrasonic agitation for o.5h before use. Stainless steel with the size of 15×15×0.3 mm substrates was used for all the depositions for parametric studies.

Results and Discussion

Effect of the suspension solvent

To produce a dense, homogeneous green from with EPD, a dilute, well dispersed and stable colloidal suspension is of great importance. According to Yuan [5], EPD of composite Al/YSZ particles was achieved using suspension of the mixture of Al and YSZ powders dispersed in acac. It was suggested that the reaction between acac and YSZ produce free protons. The free protons would be absorbed on the particle surface and consequently YSZ particles would be positively charged. Successful EPD of YSZ in pure ethanol was also reported [2]. A positive Zeta potential (1.96 mV) of YSZ particles in ethanol was measured, even though Zeta potentials were high in other alcohols with larger molecular weights [6]. It was believed that the residual water in the commercial ethanol generated free protons and hydroxyls and the YSZ particles could be positively charged by absorbing the free protons. However, the present authors postulate the charge density of the YSZ particles is limited when high purity ethanol is used. A mixture of ethanol and acac was found to be an effective medium for particle suspensions. Different materials, such as YSZ [7], $BaTiO_3$ [8, 9] had been deposited.

Figure 1 shows the weight gains as a function of the fraction of ethanol in its mixture with acac. It can be noticed that deposits were obtained in all the different mixtures. It is interesting to notice that the weight gain in pure acac is obviously much higher than in any other mixtures in constant current deposition mode (curve a). However, the advantage is much less in constant voltage mode (curve b). If we examine the voltage required for pure acac in Figure 2, it is more than 10 times of the lowest one. We can suggest that the amount of the free proton is much less in pure acac than in any other mixtures and even in pure ethanol. High electrical energy input led to the high yield. At the constant voltage mode, even though the input power (see Table 1) in pure acac is the lowest, the deposition yield was still the highest one. In constant voltage mode, the power inputs in all the mixtures are higher than either in pure acac and ethanol. Nevertheless, the deposition yields were gradually decreased with the increase of the fraction of ethanol in the mixture. It is recommended that in these mixtures, there are free protons in addition to those absorbed by the YSZ particles. The moving of these free protons partially contribute to the total electric current, the deposition rates were hence lower than the expectations.

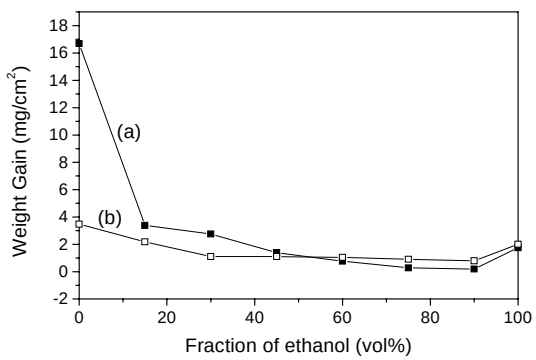

Figure 1. Weigh gains as functions of the volume fraction of ethanol in its mixture with acac. Depositions were carried out at (a) a constant current density of 0.20 mA/cm^2 and (b) a constant voltage of 50 V. Deposition time was 120 s with a powder concentration of 5g/l.

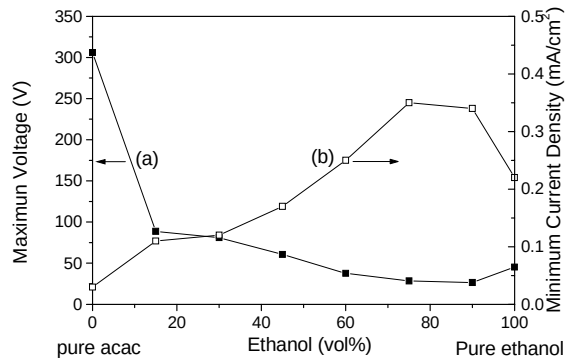

Figure 2. Current and voltage as functions of the mixing ratios of ethanol and acac during the 120 s depositions. (a) Maximun voltage required to maintain a constant current density of 0.20 mA/cm^2, and (b) minimum current density when a constant voltage of 50 V was applied.

The microstructures were examined with SEM. Figure 3 shows the micrographs taken from the surfaces of the deposited green forms at the constant voltage of 50V. Figure 3(a) and (c) show poorly packed green forms from the suspensions with pure acac and pure ethanol. The poor packing was resulted from the large agglomerates in the suspensions. This means that in the solvents of either pure acac or pure ethanol, the YSZ particles were not well dispersed because of the low free proton levels. Figure 3(b) shows a homogeneous packed deposit in the suspension with 45vol. % ethanol/55 vol. % acac as the solvent. The particle sizes are much smaller than in the other samples. Therefore, the deposition behavior was further studied for suspension in the solvent with the mixing ratio of ethanol and acac 1:1.

Table 1. Electrical Power Inputs for EPD in different suspension solvents.

Mixing ratio ethanol (vol. %)/acac (vol. %)	Input electrical power	
	Constant Current Mode (mW/cm^2)	Constant Voltage Mode (mW/cm^2)
0/100	61.2	1.5
15/85	17.7	5.5
30/70	16.2	6.1
45/55	12.1	8.5
60/40	7.5	12.5
75/25	5.7	17.5
90/10	5.3	17.2
100/0	9.1	11.1

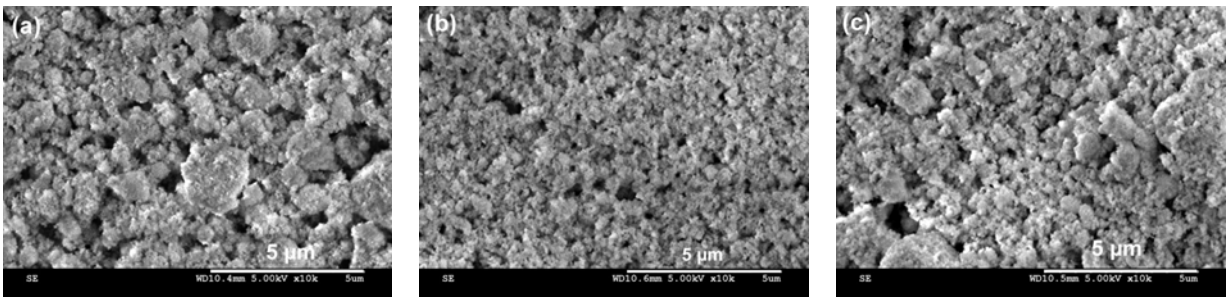

Figure 3. Micro graphs of the dried green forms deposited on stainless steel substrates at a constant voltage of 50 V for 120 s. The depositions were conducted in the suspensions of 5g/l YSZ in solvents of (a) pure acac, (b) 45vol% ethanol /55vol% acac, and (c) pure ethanol for 120 s.

Conclusions

The EPD behaviors in the suspension with acac and ethanol at different ratios were investigated. Even through depositions can be achieved in any of the mixing compositions, microstructure suggested that deposits obtained in the suspensions with ratio of ethanol to acac at about 1:1 outcome homogeneously packed green form that may form dense coatings after sintering.

References

1. P. Sarkar, X. Huang, and P. Nicholson, *J. Am. Ceram. Soc.*, **76**, 1055 (1993).
2. P.S. Nicholson, P. Sarkar, and X. Haung, *J. Mater. Sci*, **28**, 6274 (1993).
3. C.E. Baumgartner, V.J. Decarlo, P.G. Glugla, and J. Grimaldi, *J. Electrochem. Soc*. **132**, 57 (1985).
4. C.T. Chu and B. Dunn, *Appl. Phys. Lett*., **55**, 492-94(1993).
5. Y. Yuan, X. Wang, and P. Xiao, *J. Euro. Ceram. Soc.*, **24,** 2233 (2004).
6. H. Negishi, K. Yamaji, N. Sakai, T. Horita, H. Yanagishita and H. Yokokawa, *J. Mater. Sci*, **39,** 833 (2004).
7. Z. Wang, J. Shemilt, and P. Xiao, *J. Euro. Ceram. Soc.* **22,** (2002).
8. M. Naigai, K. Yamashita, T. Umegaki, and Y. Takuma, *J. Am. Ceram. Soc.*, **76**, 253 (1993).
9. R. Louh, Y. Hsu, *Mater. Chem. Phy*. 79, 226 (2003).

Communications/Visitors/Travel

None

Problems Encountered

None

NDE Development for Ceramic Valves for Diesel Engines

J. G. Sun, J.M. Zhang, J. S. Tretheway,* and J. A. Grassi*
Argonne National Laboratory
***Caterpillar, Inc.**

Objective/Scope

Emission reduction in diesel engines designated to burn fuels from several sources has lead to the need to assess ceramic valves to reduce corrosion and emission. The objective of this work is to evaluate several nondestructive evaluation (NDE) methods to detect defect/damage in structural ceramic valves for diesel engines. One primary NDE method to be addressed is elastic optical scattering. The end target is to demonstrate that NDE data can be correlated to material damage as well as used to predict material microstructural and mechanical properties. There are three tasks to be carried out: (1) Characterize subsurface defects and machining damage in flexure-bar specimens of NT551 and SN235 silicon nitrides to be used as valve materials. Laser-scattering studies will be conducted at various wavelengths using a He-Ne laser and a tunable-wavelength solid-state laser to optimize detection sensitivity. NDE studies will be coupled with examination of surface/subsurface microstructure and fracture surface to determine defect/damage depth and fracture origin. NDE data will also be correlated with mechanical properties. (2) Assess and evaluate subsurface damage in ceramic valves to be run in bench test and in a single-cylinder-engine test. All valves will be examined at ANL prior to test, during periodic scheduled shut downs, and at the end of the planned test runs. (3) Evaluate healing of subsurface damage by laser glazing on machined surfaces of GS44 ceramics. ANL will perform laser-scattering characterization on machining surfaces at before and after glazing treatment. NDE data will be correlated with glazing parameters and mechanical properties.

Technical Highlights

Work during this period (October-December 2004) focused on optimizing the full-valve laser-scatter system by using a photomultiplier tube (PMT) for detection of back-scattered signal instead of the silicon detector. Compared with the silicon detector, the PMT detector has two major advantages: (1) after equipped with appropriate data acquisition hardware, the data acquisition speed can be up to 20 KHz, more than 6 times faster than the silicon detector and, (2) detection sensitivity is as high as 0.2 pW, 5 times higher than the silicon detector.

Figure 1 is a photograph of the new system setup. Major changes include (1) delivering the back-scattered light to the PMT detector using a multimode optical fiber (Model: BFL37-200, Thorlabs Inc., Newton, NJ); (2) replacing the silicon detector by a PMT detector (Model: H5784-20, Hamamatsu Corporation, Bridgewater, NJ); and (3) acquiring data from the PMT through a 200 kHz 16-bit data acquisition board (Model: PCI-6052E, National Instruments Corporation, Austin, TX).

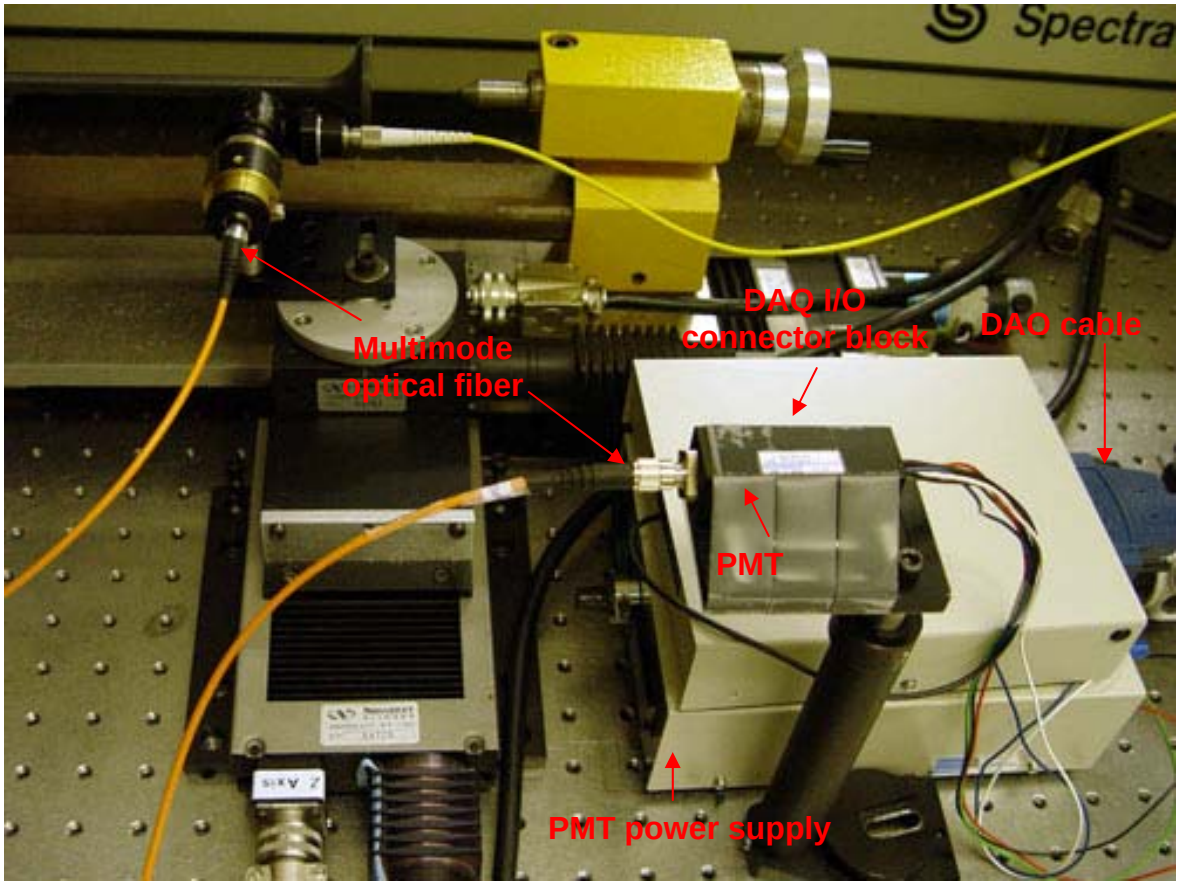

Fig. 1. Photograph of the new laser-scattering system.

This new system has been used to scan the entire valve-head section of SN235P diesel intake valve #2. The scan time for the entire valve head at a 10-μm-scan resolution is about 1 hour. Compared with the scan time of over 6 hours using the old system (with a silicon detector), the scanning efficiency is improved by >6 times. It should also be pointed out that, with this fast speed system, finer scan resolutions (i.e., 2 μm) can be achieved; while the highest scan resolution for the old system is ~10 μm, because of the speed limitations of the rotation stage.

Figure 2 shows the laser-scattering scan data of SN235P diesel intake valve #2 using the new system. The scanned region (valve head) is illustrated in Fig. 2a. The scan image of the entire valve-head section at a 10-μm-scan resolution is shown in Fig. 2b. Detailed scatter images at different locations are enlarged in Fig. 2c. This result is comparable to that obtained by the old system. It should be noted that this valve was machined by three different machining conditions (in contact surface, fillet surface, and stem surface), which can be distinguished from the laser scattering image.

We are continuing to develop and optimize the system setup. The following work will be done in the next period: (1) replacing the 100- and 50-mm range translation stages in the current system by 200- and 100-mm range translation stages, respectively, in order to examine the whole valve in a continuous scan (each valve is ~200-mm long) and, (2) making a fixture to hold the incident fiber collimator so system alignment will become easier and more accurate.

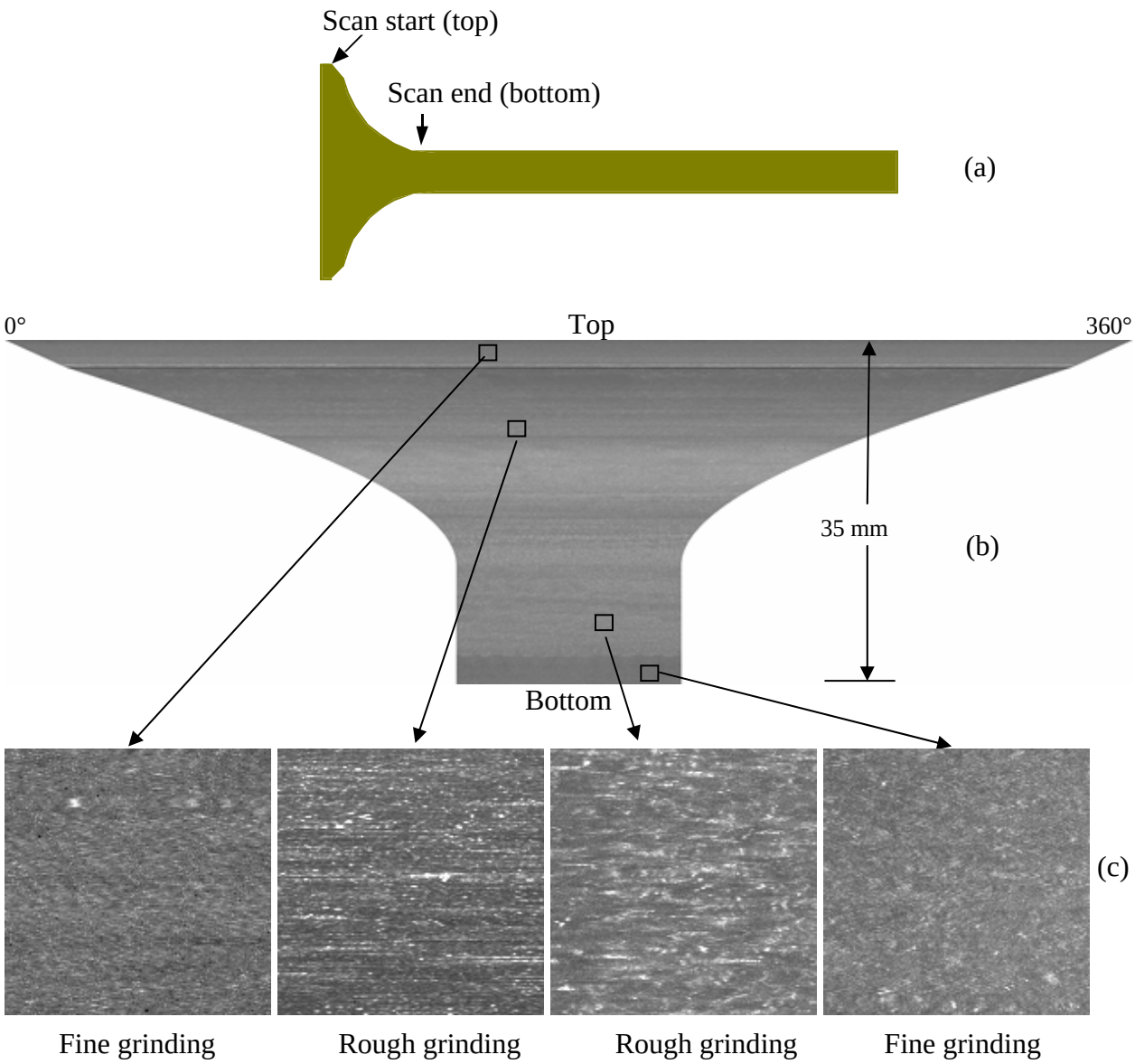

Fig. 2. (a) Illustration of scanned valve-head region (between top and bottom); (b) laser-scattering image of SN235P diesel intake valve #2; and (c) enlarged areas from (b) (image size is 1.5 mm × 1.5 mm).

Status of Milestones
Current ANL milestones are on schedule.

Communications/Visits/Travel
J. G. Sun plans to attend the American Ceramic Society's 29th International Cocoa Beach Conference and Exposition on Advanced Ceramics & Composites, Cocoa Beach, FL, January 23-28, 2005.

Problems Encountered
None this period.

Publications
- Sun, J. G., Zhang, J. M., Tretheway, J. S., Grassi, J. A., Fletcher, M. P., and Andrews, M. J., 2005, "Nondestructive Evaluation of Machining and Bench-Test Damage in Silicon-Nitride Ceramic Valves," full paper is submitted to the 29th International Cocoa Beach Conference and Exposition on Advanced Ceramics & Composites, Cocoa Beach, FL, Jan. 23-28, 2005.
- Zhang, J. M., and Sun, J. G., 2005, "Quantitative Assessment of Subsurface Damage Depth in Silicon Wafers Based on Optical Transmission Properties," full paper is submitted to International Journal of Manufacturing Technology and Management.

Durability of Diesel Engine Component Materials

Peter Blau and Jun Qu
Oak Ridge National Laboratory
and
John Truhan
University of Tennessee, Knoxville, TN

Objective/Scope

The objective of this effort is to enable the development and use of more durable, low-friction moving parts in diesel engines for heavy vehicle propulsion systems. The scope of candidate materials and coatings broadly includes metallic alloys, intermetallic compounds, ceramics, or composite materials depending on which is best-suited for each application. Parts of current interest include scuffing-critical components, like fuel injector plungers and exhaust gas recirculation (EGR) waste gate bushings. Bench-scale simulations of the rubbing conditions in diesel engine environments are developed and used to study the accumulation of surface damage, and to correlate it with the properties and compositions of the surface species. The effects of mechanical, thermal, and chemical factors on scuffing and reciprocating sliding wear are being determined. Results are used to develop graphical methods for scuffing performance mapping and to select materials for durability-critical engine components. In FY 2005 an analytical model for selecting materials for scuffing-critical applications is being developed and validated. Also in FY 2005, a new task was initiated to determine how to engineer the surfaces of titanium alloys to make them more suitable for friction- and wear-sensitive engine components. Approaches include laser surface treatment and thermal oxidation to create thin lubricating layers.

Technical Highlights

Scuffing model development. In a recent project milestone report [1] we introduced an integrated process model to help selection material combinations for scuffing resistance. The model considers both lubricant and materials effects. First, a boundary lubricating film fails and produces solid contact. Then the solids' tendency to scuff is calculated. During the first quarter of FY 2005, the latter part of the model was revised and made more explicit.

The earlier model for a dimensionless measure for scuffing tendency is given in Eqn. (1).

$$f_{scuff} = f_{tr}\, f_{def} = \left[p\left(\frac{H_h}{1.2H_s}\right) + f_{ad} \right]\left(\frac{\mu P}{\tau A}\right) \qquad (1)$$

In Eqn. (1), f_{tr} = traction factor, f_{def} = deformation factor, f_{ad} = adhesion factor, μ = friction coefficient, P = normal load, A= nominal contact area, τ = shear strength of the weaker surface of the contact pair, p = the penetration factor, H_h = scratch hardness of the harder surface, H_s = scratch hardness of softer surface. Scratch hardness incorporates dynamic effects not adequately represented by quasi-static hardness numbers such as the Vickers, Knoop, Brinell, Rockwell, etc.

In the revised model, the Hertzian contact stress (σ_c) replaces the average contact pressure (P/A). Also, since the friction coefficient μ and the traction factor f_{tr} are correlated and proportional to each other, we can restate μ in a more direct way; namely:

$$f_{scuff} = \frac{\mu \sigma_c}{\tau_y} \tag{2}$$

Based on the classical friction theory of Bowden and Tabor [2], friction can be separated into two components: (1) abrasive interaction (i.e., the mechanical grip of contacting asperities that can result in plowing), and (2) physico-chemical adhesion. The friction between two contacting asperities can be considered both with and without interpenetration, as illustrated in Fig.1 (a,b).

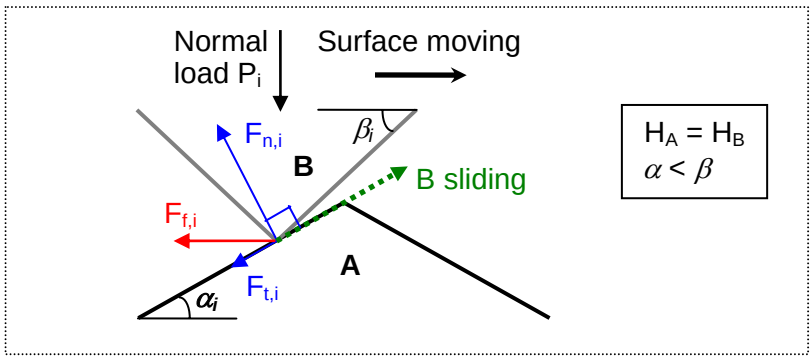

(a) Without penetration.

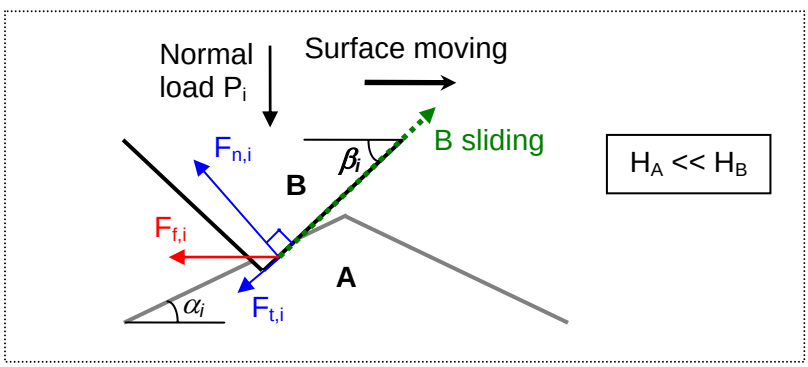

(b)With penetration.

Figure 1. Friction between two contact asperities.

Case I. Without penetration. From Fig. 1(a), the sharper asperity B slides on the slope of the blunter one A ($\alpha_i < \beta_i$). Considering F_t as purely adhesive traction (i.e., no subscale asperities), then $F_{t,i} = \mu_{ad} F_{n,i}$, where μ_{ad} is the adhesion component of the friction coefficient. It can be shown that the nominal friction coefficient at this single asperity contact is:

$$\mu_i = \frac{F_{f,i}}{P_i} = \frac{\tan\alpha_i + \mu_{ad}}{1 - \mu_{ad}\tan\alpha_i} \tag{3}$$

where $\mu_{ad} \tan\alpha_i < 1$. When $\mu_{ad} \tan\alpha_i \geq 1$, there is no relative movement between the two asperities. The contact stress will cause elastic and then plastic deformation, and eventually will either change the slopes to be low enough ($\mu_{ad} \tan\alpha_i < 1$, if $\alpha_i < \beta_i$) to allow sliding or will break the weaker of the two asperities. Note that when there is no penetration, it is the sharpness of the *blunter* of the two asperities determines the contribution of the abrasion traction to friction. When the blunter surface is smooth and flat (α is very small), μ_i will approach to μ_{ad}, indicating pure adhesion without mechanical grip. The average friction coefficient between the two sliding surfaces, composed of numerous asperity contacts, can then be approximated as

$$\mu_I = \frac{F_f}{P} \approx \frac{\Delta_{q,\min} + \mu_{ad}}{1 - \mu_{ad} \cdot \Delta_{q,\min}} \tag{4}$$

where $\mu_{ad}\Delta_{q,\min} < 1$ and $\Delta_{q,\min} = \min(\Delta_{q,h}, \Delta_{q,s})$. $\Delta_{q,h}$ and $\Delta_{q,s}$ are root mean square slopes of the harder and softer surfaces, respectively. Δ_q is a standard, measurable surface roughness parameter for the root-mean-square slope of the asperities.

Case II. With penetration. If one surface is much harder than the other, its asperities will penetrate the other one, as illustrated in Fig. 1(b). In this case, the relative motion between asperities A and B follows the slope of the harder one (no matter whether it is sharper or blunter). Using a derivation similar to that for Case I, the friction coefficient for Case II can be obtained,

$$\mu_{II} \approx \frac{\Delta_{q,h} + \mu_{ad}}{1 - \mu_{ad} \cdot \Delta_{q,h}} \tag{5}$$

As shown in Eqn. (5), *the sharpness of the harder asperity controls the abrasion factor*: the sharper the harder asperities, the greater the likelihood that they will penetrate and produce higher traction. In an extreme case that the harder surface is perfectly smooth ($\Delta_{q,h} = 0$), no penetration will occur and the friction will be merely contributed by adhesion ($\mu_{II} = \mu_{ad}$).

Considering Eqns. (4) and (5), we can allow for both cases as follows:

$$\mu = \mu_I\left(\frac{H_s}{H_h}\right) + \mu_{II}\left(1 - \frac{H_s}{H_h}\right) \approx \left(\frac{\Delta_{q,\min} + \mu_{ad}}{1 - \mu_{ad} \cdot \Delta_{q,\min}}\right)\left(\frac{H_s}{H_h}\right) + \left(\frac{\Delta_{q,h} + \mu_{ad}}{1 - \mu_{ad} \cdot \Delta_{q,h}}\right)\left(1 - \frac{H_s}{H_h}\right) \tag{6}$$

If the harder surface is the blunter of the two, Eqn. (6) can be simplified to $\mu = \mu_I = \mu_{II}$. Note that the hardness and root mean square slopes can be measured; however, the adhesion factor μ_{ad} is not as straightforward to obtain because the phenomenon of adhesion is much less understood.

In one approach, Rabinowicz [3] claims that adhesion is high when contact surfaces have high surface energy and low hardness. For certain crystal structures the adhesive contribution to friction is roughly proportional to the ratio of the energy of adhesion to the hardness of the softer surface. It is also observed that smooth, clean surfaces can experience severe adhesion. Future

reports will describe our derivation of μ_{ad} and how one can incorporate the Coulomb-Mohr theory (internal-friction theory) of failure to estimate the yield strength in shear for the model, τ_y [4]. It may also be necessary to modify the model to account for the findings of Tabor [5] who noted that abrasion tends to occur when (hardness of material 1: material 2) $\geq$ (1.2:1).

Future Plans

1) Refine and test the scuffing model using both actual material properties and materials of interest for diesel engine components.

2) Continue to seek and test surface engineering methods, such as thermal oxidation and texturing, to reduce the friction and wear of titanium alloys for engine applications.

Travel

None.

Status of Milestones

1) Prepare transition diagrams for current and promising, new fuel system materials that exemplify the relationship between real contact pressure, surface finish, and the onset of scuffing in diesel fuel environments. (March 31, 2004 - completed)

2) Develop a model for selecting materials and their optimal surface finishes for scuffing applications in diesel engines. (September 30, 2004**)**

3) Report on the results of research to improve the friction and wear characteristics of titanium alloys by applying surface engineering methods like thermal oxidation and controlled surface patterning. (June 30, 2005)

4) Develop mechanistic model for scuffing processes in boundary-lubricated fuel injector plunger materials. (September 30, 2005)

Publications

Qu, J., Truhan, J .J., Blau, P. J., "Detecting the Onset of Localized Scuffing with the Pin-on-Twin Fuel-Lubricated Test for Heavy Duty Diesel Fuel Injectors," *SAE International Journal of Engine Research*, Vol. 6, No. 1, Mar. 2005 (in press).

Qu, J., Truhan, J. J., Blau, P. J., "Evaluating Candidate Materials for Heavy Duty Diesel Fuel Injectors Using a 'Pin-On-Twin' Scuffing Test," *Tribology International*, Vol. 38, 2005 (now available online).

Numbered References

1. P. J. Blau, J. Qu, and J.J. Truhan, Jr., "On the Definition and Mechanisms of Scuffing in Fuel System Components: an Integrated Process Model," Project milestone report, Sept. 30, 2004.
2. F. P. Bowden and D. Tabor, Friction and Lubrication of Solids, Oxford Press, 1986.
3. E. Rabinowicz, Friction and Wear of Materials, John Wiley & Sons, Inc., 1965.
4. C. R. Mischke and J. E. Shigley, Mechanical Engineering Design, 5th Ed., 1989, p. 246-251.
5. D. Tabor, The Hardness of Metals, Oxford Press, 1951.

Life Prediction of Diesel Engine Components

H. T. Lin, T. P. Kirkland, A. A. Wereszczak, M. K. Ferber
Oak Ridge National Laboratory
and Jeremy Trethewey
Caterpillar

Objective/Scope

The valid prediction of mechanical reliability and service life is a prerequisite for the successful implementation of structural ceramics and advanced intermetallic alloys as internal combustion engine components. There are three primary goals of this research project which contribute toward that implementation: the generation of mechanical engineering data from ambient to high temperatures of candidate structural ceramics and intermetallic alloys; the microstructural characterization of failure phenomena in these ceramics and alloys and components fabricated from them; and the application and verification of probabilistic life prediction methods using diesel engine components as test cases. For all three stages, results are provided to both the material suppliers and component end-users.

The systematic study of candidate structural ceramics (primarily silicon nitride) for internal combustion engine components is undertaken as a function of temperature (< 1200°C), environment, time, and machining conditions. Properties such as strength and fatigue will be characterized via flexure and rotary bend testing.

The second goal of the program is to characterize the evolution and role of damage mechanisms, and changes in microstructure linked to the ceramic's mechanical performance, at representative engine component service conditions. These will be examined using several analytical techniques including optical and scanning electron microscopy. Specifically, several microstructural aspects of failure will be characterized:

(1) strength-limiting flaw-type identification;
(2) edge, surface, and volume effects on strength and fatigue size-scaling
(3) changes in failure mechanism as a function of temperature;
(4) the nature of slow crack growth; and
(5) what role residual stresses may have in these processes.

Lastly, numerical probabilistic models (i.e., life prediction codes) will be used in conjunction with the generated strength and fatigue data to predict the failure probability and reliability of complex-shaped components subjected to mechanical loading, such as a silicon nitride diesel engine valve. The predicted results will then be compared to actual component performance measured experimentally or from field service data. As a consequence of these efforts, the data generated in this program will not only provide a critically needed base for component utilization in internal combustion engines, but will also facilitate the maturation of candidate ceramic materials and a design algorithm for ceramic components subjected to mechanical loading in general.

Technical Highlights

Studies of dynamic fatigue behavior of a commercial grade silicon nitride, i.e., SN147-31E, manufactured by Ceradyne Advanced Ceramic, Inc., CA, were completed during this quarterly report period. The SN147-31E was processed with similar sintering additives (i.e., Al_2O_3 and Y_2O_3) to those employed for SN147-31N evaluated and reported previously. However, the SN147-31E contains a crystalline secondary phase achieved by a post heat treatment. Thus, it is anticipated that SN147-31E would exhibit a higher temperature mechanical reliability than SN147-31N due to the presence of crystalline secondary phase. The SN147-31E silicon nitride bend bars were longitudinally and transversely machined per the revised ASTM C116 standard with 600 grit surface finish. The dynamic fatigue tests were carried out at 20 and 850°C and at stressing rate of 30 and 0.003 MPa/s in air per ASTM C1465. The 30 MPa/s is used to evaluate the inert characteristic strength as a function of temperature, and 0.003 MPa/s is applied to measure the slow crack growth (SCG) susceptibility at temperatures. Some of the samples were tested at 1000°C and at 30 MPa/s to evaluate its high temperature application limit.

Dynamic fatigue results at 30 MPa/s showed that the transversely machined SN147-31E silicon nitride exhibited little or no decrease in characteristic strength at temperature up to 1000°C as compared to those obtained at 20°C (shown in Table 1 and Figs. 1-5). However, the SN147-31E samples exhibited the higher Weibull moduli at elevated temperatures then the value obtained at 20°C. Also, results at 850°C indicated that there is apparent decrease in characteristic strengths (about 19%) when tested at 0.003 MPa/s (Fig. 2). In addition, the fatigue exponent of transversely machined SN147-31E decreased from 338 at 20°C to 39 at 850°C (as shown in Fig. 6), indicative of an increased susceptibility to SCG process. On the other hand, for the longitudinally machined SN147-31E samples there was no apparent strength degradation when test temperature increased from 850 to 1000°C (Table 1 and Fig. 3 and 5), similar to that observed for the transversely machined samples. The detailed SEM examinations will be carried out to elucidate the change in fatigue exponent at 850°C and the possible cause of the increased susceptibility to SCG.

Sixteen NT551 silicon nitride valves, 14 with 30° and 4 with 45° valve seat angle, after 500 h bend rig test at Caterpillar have been received for mechanical strength evaluation (Fig. 7). In general, the optical microscopy examinations showed that there were no apparent surface damages/flaws observed after the bench rig test, except the distinct valve seat markings at the valve and stainless steel valve seat contact point. Strength testing will be carried out at room temperature to evaluate the effect of 500 h bench rig test on the mechanical performance, especially due to the presence of subsurface damages (flaws) introduced due to the contact and wear. The result will be summarized in the next quarterly report.

Status of Milestones

Milestone: “Complete testing and analysis of prototype silicon nitride valves after bench rig testing.” On schedule.

Communications / Visitors / Travel

Communication with Jeremy Trethewey at Caterpillar on the on the update of the dynamic fatigue test results of Ceradyne SN147-31E silicon nitride.

Communication with Jeremy Trethewey at Caterpillar on the on the update of the preliminary examination of NT1551 valves received after 500 h bench rig test.

Problems Encountered

None.

Publications

H. T. Lin, T. P. Kirkland, A. A. Wereszczak, and M. J. Andrews, "Strength Retention of Silicon Nitride After Long-Term Oil Immersion Exposure," submitted to *J. Mater. Sci*.

References

[1] H. T. Lin, T. P. Kirkland, M. K. Ferber, and M. J. Andrews, "Life Prediction of Diesel Engine Components," Heavy Vehicle Propulsion System Materials Program Quarterly Technical Progress Report to DOE Office of Transportation Technologies, Oct. – Dec., 2003.
[2] H. T. Lin, T. P. Kirkland, M. K. Ferber, and M. J. Andrews, "Life Prediction of Diesel Engine Components," Heavy Vehicle Propulsion System Materials Program Quarterly Technical Progress Report to DOE Office of Transportation Technologies, Jan. – March, 2004.
[3] H. T. Lin, T. P. Kirkland, M. K. Ferber, and M. J. Andrews, "Life Prediction of Diesel Engine Components," Heavy Vehicle Propulsion System Materials Program Quarterly Technical Progress Report to DOE Office of Transportation Technologies, Apr. – June, 2004.

Table 1. Summary of uncensored Weibull and strength distributions for Ceradyne SN147-31E silicon nitride specimens longitudinally and transversely machined per ASTM C1161. Data of SN147-31N machined longitudinally as well as transversely is used for reference.

Material	# of Spmns. Tested	Stressing Rate (MPa/s)	Temp. (°C)	Uncens. Weibull Modulus	± 95% Uncens. Weibull Modulus	Uncens. Chrctstic Strength (MPa)	± 95% Uncens. Chrctstic Strength (MPa)
SN147-31N-Long	15	30	20	21.73	14.07. 31.09	836	814, 858
SN147-31N-Long	15	30	850	20.35	13.58, 28.20	777	755, 799
SN147-31N-Long	15	0.003	850	16.19	10.57, 23.02	732	706, 757
SN147-31N-Trans	15	30	20	13.76	8.96, 19.59	677	649, 705
SN147-31N-Trans	15	30	850	18.26	11.67, 26.47	639	619, 659
SN147-31N-Trans	15	0.003	850	19.95	12.83, 28.63	620	602, 638
SN147-31E-Long	15	30	20	17.30	10.86, 25.58	668	645, 690
SN147-31E-Long	15	0.003	20	16.19	10.60, 22.98	620	598, 642
SN147-31E-Long	15	30	850	9.36	6.01, 13.62	604	567, 641
SN147-31E-Long	15	0.003	850	12.06	7.70, 17.52	509	485, 533
SN147-31E-Long	15	30	1000	16.49	10.61, 23.66	585	564, 605
SN147-31E-Trans	15	30	20	7.44	4.89, 10.58	623	575, 671
SN147-31E-Trans	15	0.003	20	8.99	5.61, 13.45	607	568, 646
SN147-31E-Trans	15	30	850	43.94	28.37, 62.78	642	634, 651
SN147-31E-Trans	15	0.003	850	18.02	11.93, 25.18	521	505, 538
SN147-31E-Trans	15	30	1000	34.66	21.97, 50.70	602	591, 611

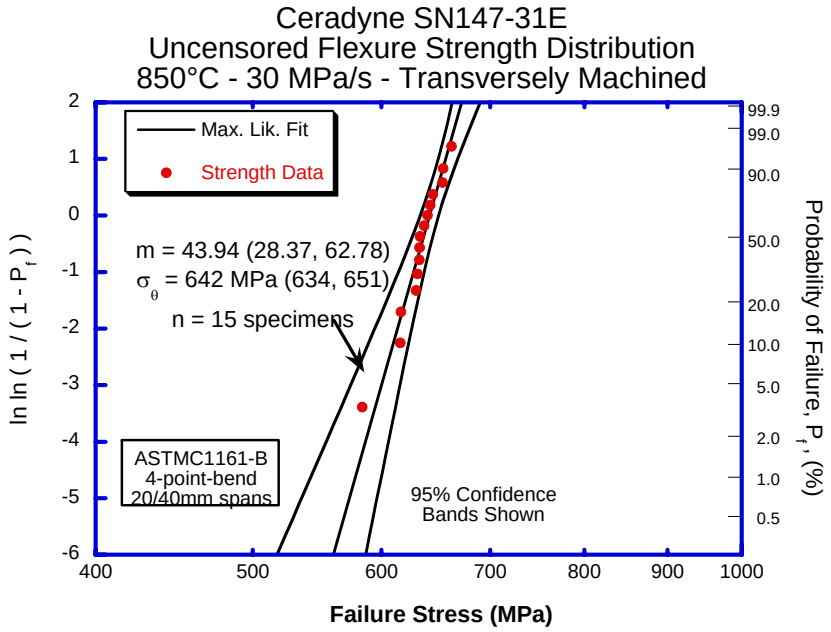

Figure 1. Strength distribution of Ceradyne SN147-31E longitudinally machined and tested at 850°C and at 30 MPa/s.

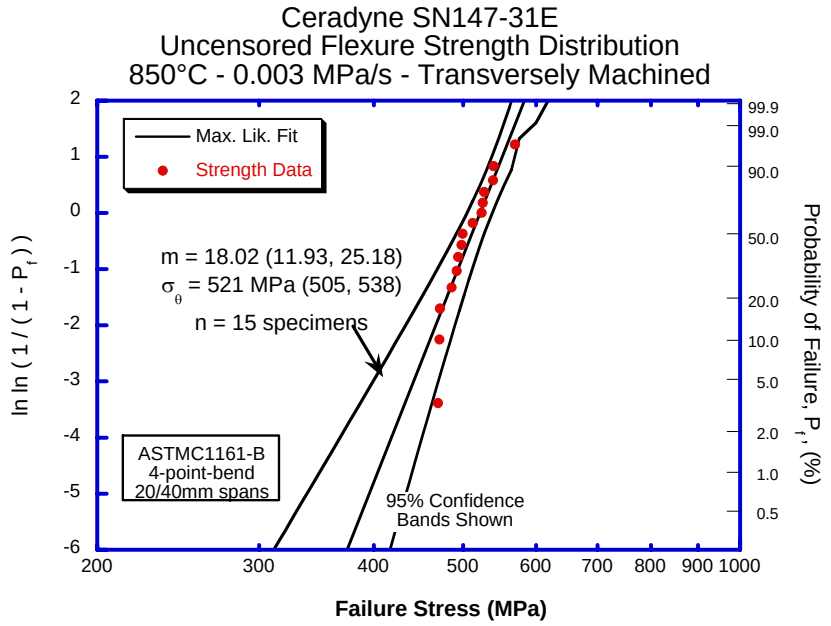

Figure 2. Strength distribution of Ceradyne SN147-31E transversely machined and tested at 8500°C and at 0.003 MPa/s.

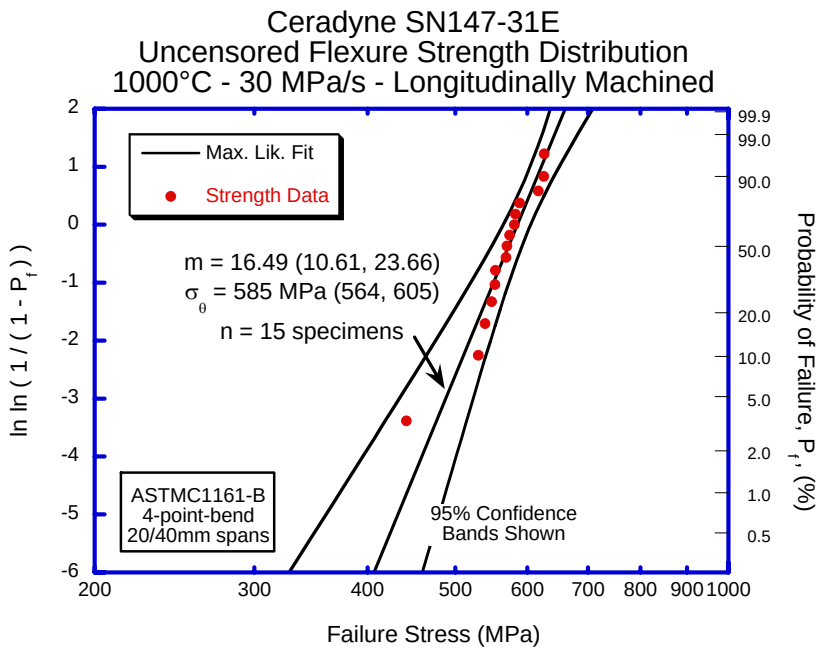

Figure 3. Strength distribution of Ceradyne SN147-31E longitudinally machined and tested at 1000°C and at 30 MPa/s.

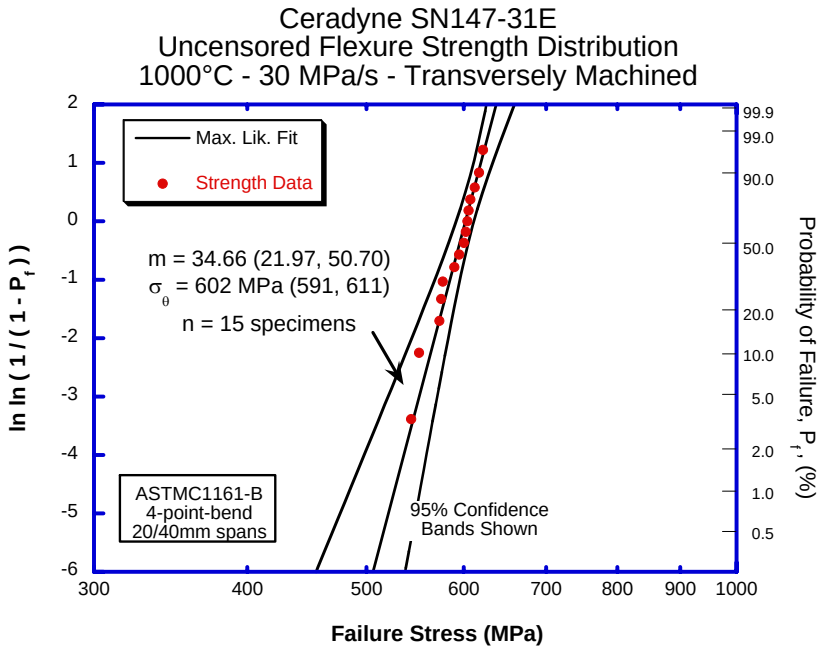

Figure 4. Strength distribution of Ceradyne SN147-31E transversely machined and tested at 1000°C and at 30 MPa/s.

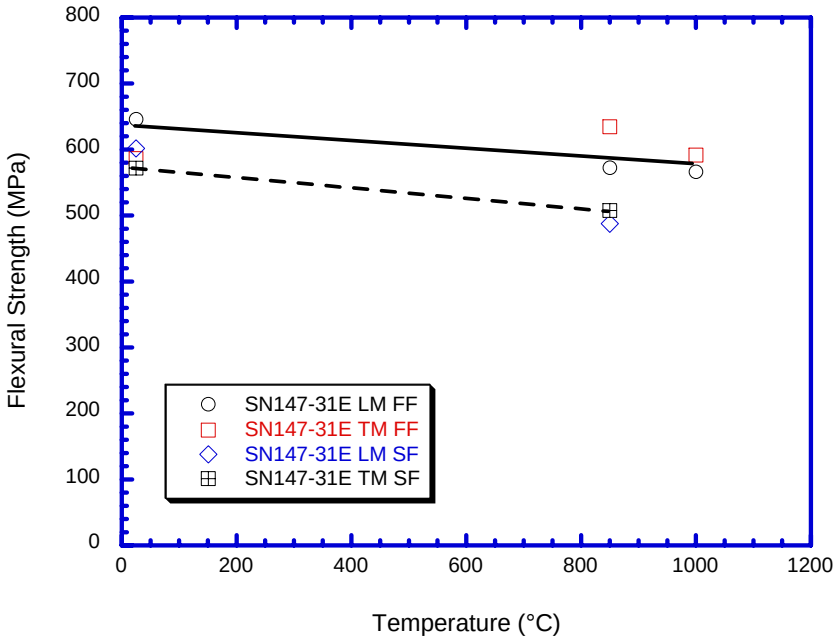

Figure 5. Flexure strength of Ceradyne SN147-31E longitudinally and transversely machined as a function of test temperature in air. FF denotes 30 MPa/s and SF denotes 0.003 MPa/s stressing rate.

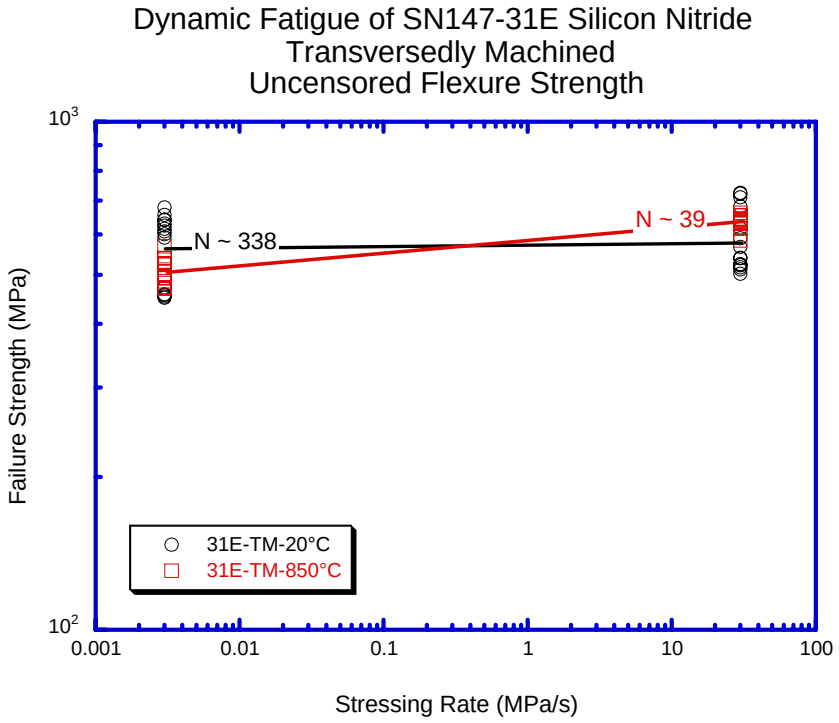

Figure 6. Failure strength versus stressing rate curve of SN147-31E longitudinally machined and tested at 20° and 850C in air.

Figure 7. Photo of NT551 silicon nitride valves after 500 h bench rig test. The arrows indicate the valve seat markings after the bench rig4 test.

Low-Cost Manufacturing of Precision Diesel Engine Components

P. J. Blau, Jun Qu, and Tyler Jenkins
Oak Ridge National Laboratory

Objective/Scope

The objectives of this effort are (1) to identify and investigate cost-effective processes to machine precision components of advanced materials for diesel engines and (2) to develop and use methods to characterize the effects of machining on the surface quality and performance of advanced engine materials.

Technical Highlights

Machining of Advanced Cermets. Composite materials that contain a high percentage of ceramic phases in a metallic binder are called cermets. Cermets offer promise as highly-durable engine component materials, but fabrication and finishing costs must be reduced to enable them to be more widely utilized. This quarter, we began a literature review and investigation of current machining practices for composite materials containing metals and ceramics. In parallel, test coupons of a cermet based on nickel aluminide (Ni_3Al) and titanium carbide are being prepared for this machining study by T. N. Tiegs and F. C. Montgomery, of the ORNL Metals and Ceramics Division. Two levels or hard particles are being included: 25 and 50% by volume. Based on the results of the findings of the preliminary technology review, a test matrix of machining conditions will be established and a series of instrumented grinding tests will be initiated. The surface quality for different material removal rates and the mechanisms by which the grinding media interact with the hard and softer constituents in the cermet microstructures are of interest in this investigation.

Future Plans

(1) Conduct instrumented grinding tests on cermet materials to investigate the effects of hard particle content on grindability and surface quality.

(2) Continue to help in the development and validation of high-speed machining models for titanium and other materials within the Third Wave Machining Consortium.

Travel

None.

FY 2005 Milestone

1) Complete an investigation on the effects of grinding and related abrasive removal processes on surface quality in advanced cermets. **(06/05)**

Presentations and Publications

None.

Cost-Effective Machining of Titanium Alloys

Albert Shih
University of Michigan

Objective/Scope

The objective of this research is to investigate new technologies for cost-effective machining of Ti alloys. Experiments and modeling of the turning and drilling of titanium alloys and new tool materials are investigated.

Technical Highlights

The simulation and experiment of drilling Ti-6Al-4V were conducted. The TiC (95%)-Ni_3Al (5%) metal matrix ceramic (MMC), prepared by Oak Ridge National Laboratory, was tested as new tool material for turning CP Ti.

1. Ti Drilling Test

1.1. Experiment design

The drilling experiments of Ti-6Al-4V plate were conducted on a Mori-Seiki vertical machining center. To investigate the thrust force, toque, drill wear, chip morphology, and burr formation, two types of drill, a HSS twist drill with 3 mm diameter and a Kennametal K285A01563 WC-Co dynapoint drill with 3.97 mm diameter, were used. The workpiece is Ti-6Al-4V plate with 3.5 and 6.9 mm thickness, respectively.

A baseline test was conducted using the HSS drill at three peripheral cutting speeds (6.1, 12.2, 18.3 m/min) and 0.051 mm/rev feed. Another set of tests were conducted using WC-Co drill with peripheral cutting speeds at 18.3, 27.4, 36.6, 45.7, 54.9, 64.0, 73.2, and 82.3 m/min under 0.051 mm/rev feed. The thrust force and torque were measured. The effect of spindle speed on the drill life was studied. And, the chip morphology and burr formation were compared.

1.2. HSS drill

Results of the effect of cutting speed on drill life for HSS drilling of 3.5 mm thick Ti-6Al-4V plate are listed in Table 1. The tool life decreased significantly with the increase of peripheral cutting speed. The drill broke at the peripheral cutting speeds of 12.2 and 18.3 m/min. Besides the short tool life, another disadvantage of using HSS drill is the formation of large size exit burr, as shown in Fig. 1.

Table 1. Tool life of HSS drilling Ti-6Al-4V.

Peripheral cutting speed (m/min)	6.1	12.2	18.3
Tool life (s)	>319.5	31.9	4.3

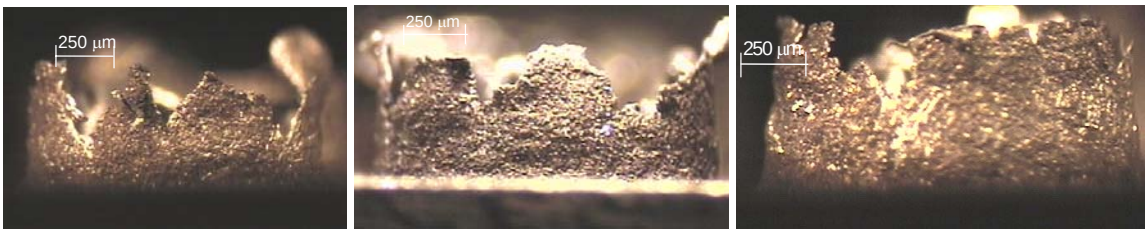

(a) (b) (c)

Fig. 1. Exit burr of HSS drilling of Ti-6Al-4V at (a) 6.1, (b) 12.2, and (c) 18.3 m/min peripheral cutting speed.

1.3. WC-Co drill

Under the same feed (0.051 mm/rev), the spindle speed or drill peripheral cutting speed determines the material removal rate and effectiveness in machining of Ti alloys. At high cutting speed, the tool temperature is high, which shortens the tool life. Experiment results showed the WC-Co drill provided by Kennametal is able to drill Ti-6Al-4V at high cutting speeds, up to 82.3 m/min or 6602 rpm. A 4 mm diameter hole can be penetrated in 1.2 s. It shows that new drills are much better in performance and tool life on drilling Ti alloys. At the high material removal rate drilling, change in color of the chip and workpiece were visible.

Fig. 2 shows the thrust forces and torques as a function of peripheral cutting speed for WC-Co drilling of Ti. The thrust force increases sharply at 82.3 m/min peripheral cutting speed although the torque remains constant for all the speeds.

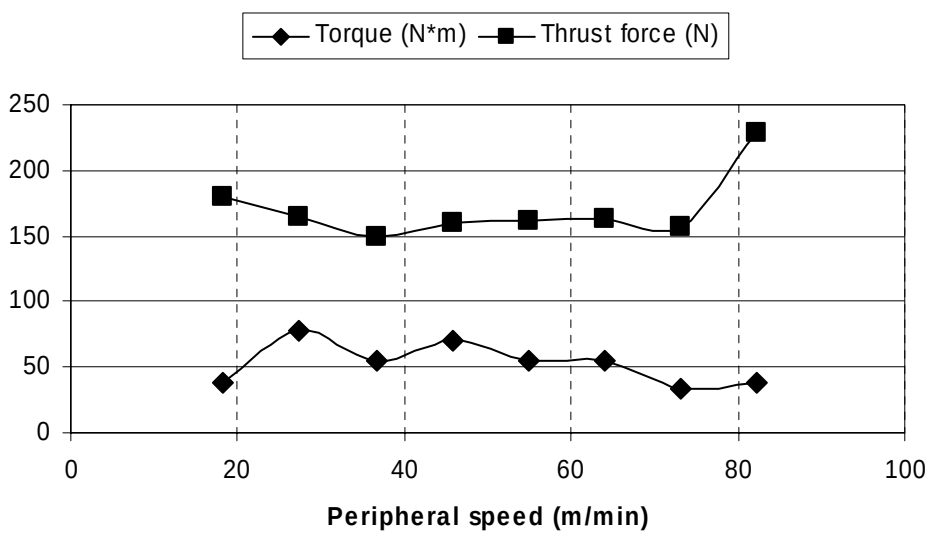

Fig. 2. Thrust forces and torques as a function of peripheral cutting speed.

The chip morphology is affected by peripheral cutting speed, as shown in Fig. 3. The spiral (small pitch) followed by ribbon (folded) chip at low peripheral cutting speed is a common chip

morphology for ductile materials in drilling. The long ribbon (folded) followed by long ribbon (long pitch) chip at high peripheral cutting speed likely results from the change of material properties, due to the high temperature at high speed.

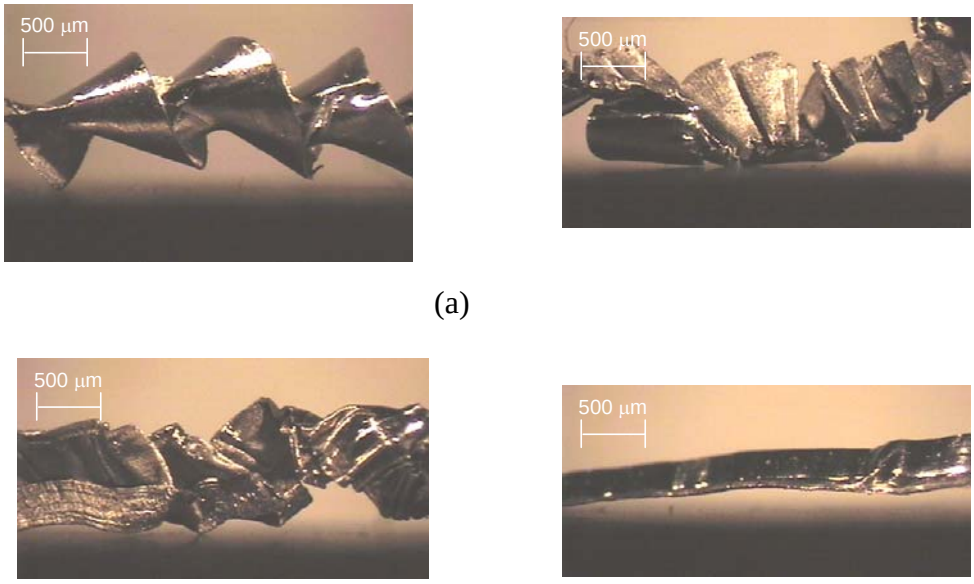

(a)

(b)

Fig. 3. Chip morphology of drilling Ti-6Al-4V: (a) spiral (small pitch) followed by ribbon (folded) chip at low peripheral cutting speed (18.3 m/min) and (b) long ribbon (folded) followed by long ribbon (long pitch) chip at high peripheral cutting speed (82.3 m/min).

Fig. 4. Ti-6Al-4V burr formation with WC-Co drill: (a) very small burr at low peripheral cutting speed (18.3-54.9 m/min) and (b) uniform burr with cap formed at high peripheral cutting speed (64.0 to 82.3 m/min).

Burr size is very small for the hole drilled by WC-Co drill. As shown in Fig. 4(a), almost no visible burr can be seen at low peripheral cutting speed from 18.3 to 54.9 m/min. At high peripheral cutting speed from 64.0 to 82.3 m/min, small uniform burrs with cap were formed, as shown in Fig. 4(b).

Drill wear is a technical barrier which needs to be overcome in Ti drilling process. Fig. 5 shows the damage on the tool tip, buildup edge at tool chisel edge, margin and cutting edge wear of the WC-Co drill after drilling for 87 s at peripheral cutting speeds from 18.3 to 82.3 m/min (0.051 mm/rev feed). Results of this preliminary Ti drilling experiment demonstrate that the existing WC-Co drill, with suitable process parameters, can have reasonably good performance in Ti drilling. This research will work with Kennametal to search for process parameters, tool geometry, and coatings to enable cost-effective drilling of Ti.

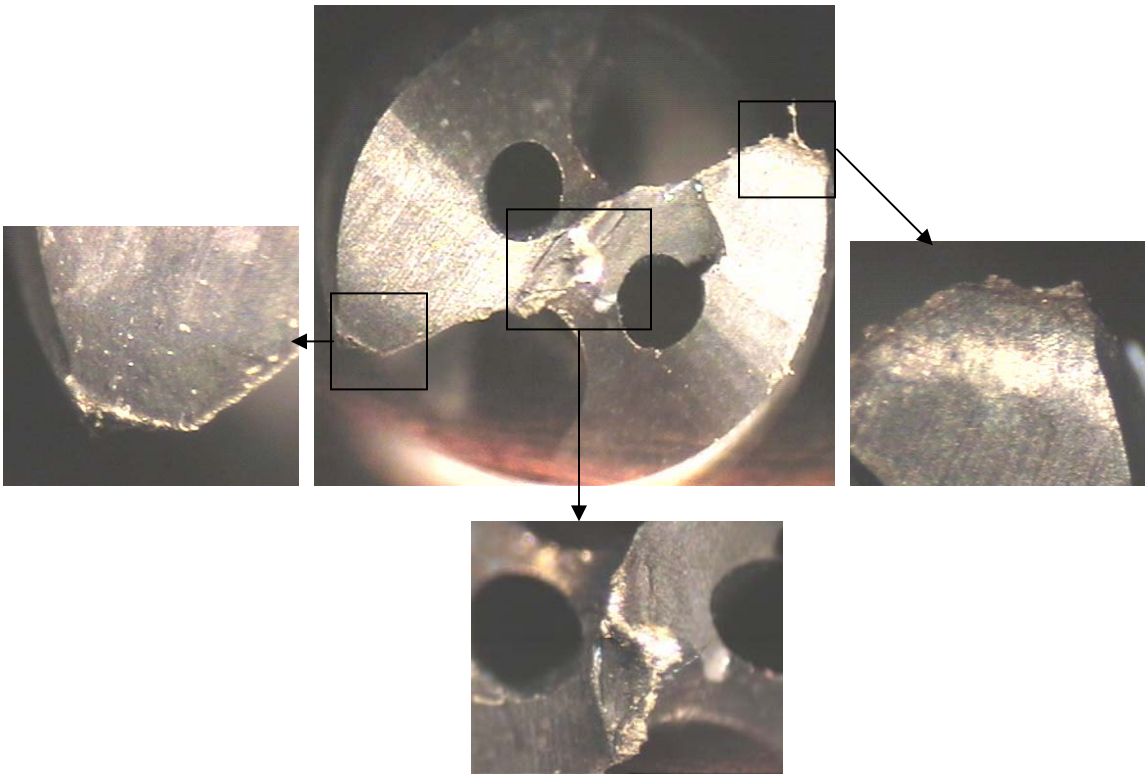

Fig. 5. WC-Co drill wear after drilling 87 s at peripheral cutting speeds from 18.3 to 82.3 m/min and 0.051 mm/rev feed.

2. Turning test with TiC-Ni_3Al material

The diffusion wear is a key factor that limiting the tool life in Ti machining using WC-Co tool. An idea to use the TiC-Ni_3Al tool for machining of Ti is explored. The TiC(95%)-Ni_3Al(5%) material was prepared by Dr. Terry Tiegs and machined (WEDMed and polished) by Dr. Jun Qu at ORNL. A series of lathe turning tests were conducted using this new tool material at Univ. of Michigan.

Figure 6 shows the optical microscopic image of the material. The porosity of the material is obvious. The edge preparation of the tool insert may also be critical. We do not have complicated tool grinding machine for edge and nose radius preparation. This, compounded with the porosity of the material, can significantly shorten the tool life. The tool geometry, as shown in Fig. 7(a), was the same as the Kennametal TPG160308 tool insert used in previous Ti

lathe turning tests for mutual comparison. An optical picture of the TiC-Ni_3Al tool insert is shown in Fig. 7(b).

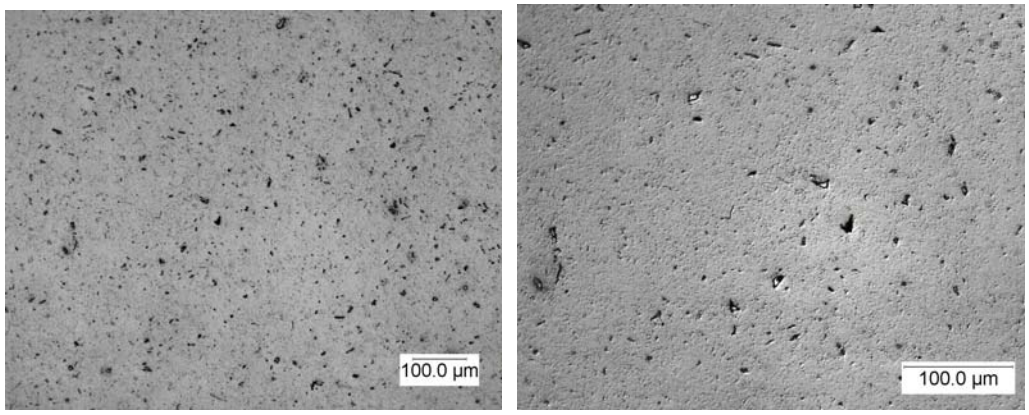

Fig. 6. Optical microscopic image of the TiC-Ni_3Al tool material.

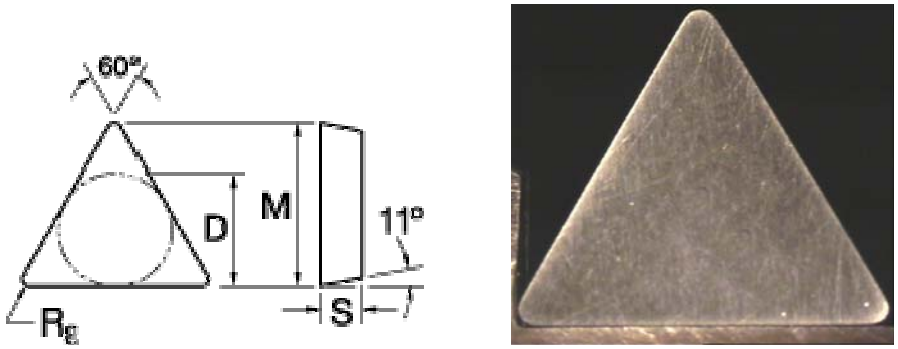

(a) (b)

Fig. 7. Tool geometry: (a) schematic of Kennametal TPG160308 tool insert (courtesy of Kennametal) and (b) optical image of TiC-Ni_3Al tool insert.

The first set of turning tests using the TiC-Ni_3Al tool was conducted at three feeds (0.051, 0.127, and 0.254 mm/rev), 24.4 m/min cutting speed, and 1 mm depth of cut. As a comparison, a set of tests was conducted using uncoated WC-Co tool at the same cutting conditions. Fig. 8 shows the comparison of cutting forces. For both tools, the cutting forces increased as feed increased. The TiC-Ni3Al tool generated higher cutting forces than WC-Co tool. The low axial force in WC-Co may be due to better edge preparation, i.e., sharper cutting edge.

In order to test the effect of cutting speed on TiC-Ni_3Al tool, another set of tests was conducted at five higher cutting speeds (24.4, 48.8, 97.5, 195, and 243.8 m/min), 0.254 mm/rev feed, and 1 mm depth of cut, using both TiC-Ni_3Al and WC-Co tools. Fig. 9 shows the comparison of cutting forces. This test shows that the tool can work at high cutting speed up to 243.8 m/min. But the cutting time was short.

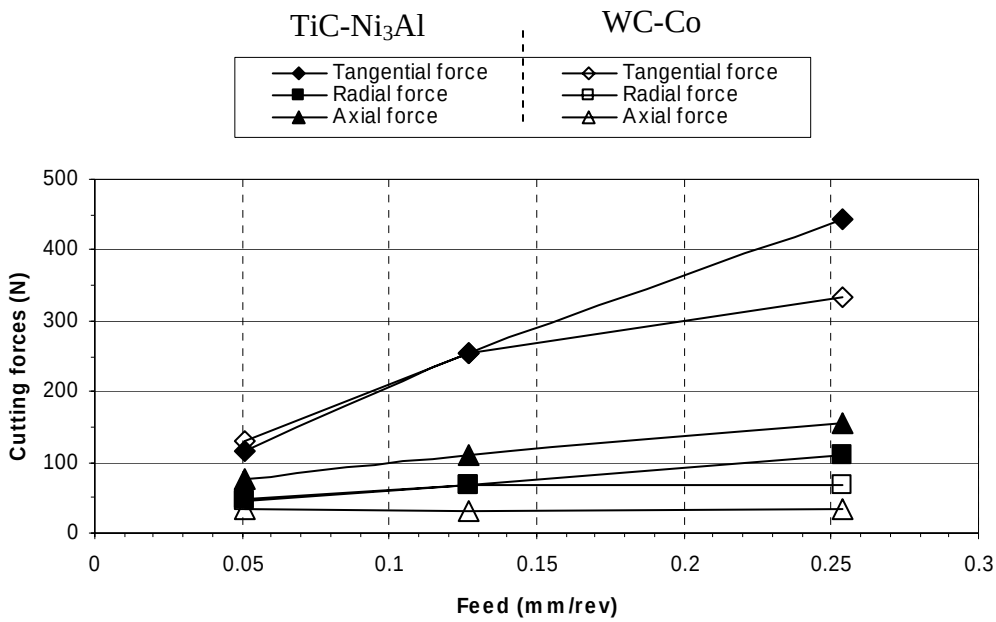

Fig. 8. Cutting forces as a function of feed.

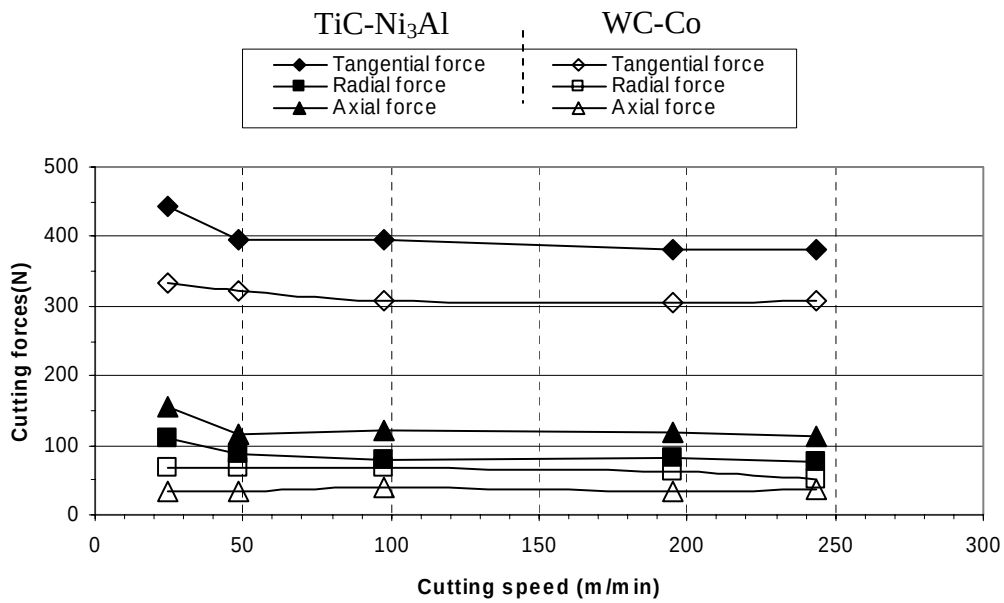

Fig. 9. Cutting forces as a function of cutting speed.

The third set of test is to investigate the tool life of TiC-Ni_3Al tool at different cutting speeds. The test was conducted at three different cutting speeds (24.4, 48.8, and 195 m/min), 0.254 mm/rev feed, and 1 mm depth of cut. Table 2 lists the tool life at different cutting speeds. The tool life for TiC-Ni_3Al tool is relatively short, especially at the high cutting speed. As a comparison, the WC-Co tool life is 69 s when cutting at 195 m/min, 0.254 mm/rev feed, and 1.02

mm depth of cut. At all cutting speeds, the tool failed by breakage, as shown in Fig. 10. This is different from the traditional diffusion wear that is commonly seen in turning of Ti. This indicates that the brittleness of the material subject to impact loading during machining of Ti with cyclic cutting force with adiabatic shear band formation is the likely cause of tool failure.

Table. 2. Tool life at three cutting speeds for TiC-Ni_3Al tool turning of CP Ti.

Cutting speed (m/min)	24.4	48.8	195
Tool life (s)	245.3	18.4	15.3

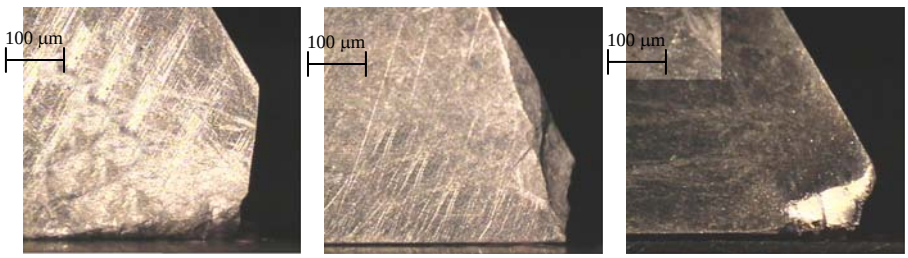

(a) (b) (c)

Fig. 10. Broken TiC-Ni_3Al tools at different cutting speed (m/min): (a) 24.4, (b) 48.8, and (c) 195.

Future Work

The test will continue on improving the TiC-Ni_3Al tool material for the next round of Ti machining tests. An experimental setup to measure the tool tip temperature has also been setup. On the finite element modeling, Third Wave Systems is working on improving the drilling simulation efficiency and accuracy. High speed drilling of Ti will continued by collaborating with Kennametal on coated and uncoated WC-Co drill.

Status of Milestones

Milestone 1: 2D finite element modeling of titanium machining process.
Status: Completed. Effects of cutting speed, feed, and coating effects have been investigated using the Third Wave AdvantEdge software for machining of Ti-6Al-4V.

Milestone 2: 3D finite element modeling of titanium machining process.
Status: Extensive study of 3D turning of CP Ti and parametric study work of different cutting parameters, tool geometries, and tool coatings have been conducted. The work is continuing in 3D drilling.

Milestone 3: Investigation of TiC-based cutting tool material.
Status: Exploratory tests have been conducted. Cutting forces have been measured and compared with the results when using WC-Co tool at different cutting speeds and feeds. Tool life has been evaluated at different cutting speeds.

Milestone 4: Titanium turning tests.
Status: Experiments have been set up for lathe turning of Ti alloys. Tool wear tests using tools with different coatings and corner radius have been conducted. Extensive tests have been conducted to verify the finite element modeling.

Milestone 5: Titanium drilling tests.
Status: Drilling tests of Ti-6Al-4V have been conducted using both HSS twist drill and WC-Co dynapoint drill.

Communications/Visit/Travel

Ray Johnson and Paul Becker visited Univ. of Michigan on Dec. 2nd and reviewed the progress of this project.

Publications

R. Li, A. J. Shih, "Finite Element Modeling of 3D Titanium Turning**,**" *2004 ASME IMECE* at Anaheim, CA in Nov. 2004.
R. Li and A. J. Shih, "Finite Element Modeling of 3D Turning of Titanium," *International Journal of Advanced Manufacturing Technology* (accepted).

Advanced Cast Austenitic Stainless Steels for High Temperature Components

P.J. Maziasz, John P. Shingledecker, and N.D. Evans
Oak Ridge National Laboratory
and M.J Pollard
Caterpillar, Inc.

Objective/Scope

This is the 2nd CRADA project with Caterpillar, and focused on commercialization of the new CF8C-Plus cast austenitic stainless steel developed on the first ORNL/CAT CRADA. CF8C-Plus steel is a cost-effective performance upgrade relative to current heavy-duty diesel engine exhaust component materials, including SiMo ductile cast iron. In FY2005, this project will complete the initial properties data base needed for component design or redesign, particularly fatigue, thermal fatigue, and creep, and studies of aged materials, including impact properties. This CRADA (Cooperative Research and Development Agreement) project (ORNL02-0658) began on July 21, 2002, and has been extended for 2 more years beyond the 3 year expiration date of July 21, 2005. More detailed information on this project must be requested directly from Caterpillar, Inc.

Technical Highlights, 4th Quarter, FY2005

Background

Evidence is increasing that shows that current cast iron heavy diesel engine exhaust manifolds and turbocharger housings are being pushed beyond their temperature capabilities as normal duty cycles go to 750°C or higher, and included rapid and severe thermal cycling. New materials with upgraded temperature capability and reliability must also be commercially available at a reasonable cost. The new cast CF8C-Plus austenitic stainless steel shows the promise of being such a material. Current efforts by Caterpillar, Inc. and ORNL include completing the systematic and thorough properties data base required by designers to optimize component design, and characterizing the properties of trial or prototype commercial components.

Approach

Multiple commercial heats of CF8C-Plus have been made by several commercial foundries, including static sand and centrifugal casting methods. In FY 2004, new heats of standard CF8C-Plus (Mn+N) and a new modified CF8C-Plus steel (Mn+N+Cu+W) have been produced by MetalTek and are being tested and characterized at ORNL. The next step is to make and characterize prototype or trial components for various applications of CF8C-Plus steel.

Technical Progress

Figure 1 shows a compilation of all the ultimate tensile strength (UTS) as a function of temperature for specimens made from various kinds of commercial heats (typically 500 lb or more, air melted), or smaller ORNL lab-scale heats (15 lb, air melted). There is a clear strength advantage of 100 MPa or more of the new CF8C-Plus steel relative to the standard CF8C steel, particularly at 600°C and above. There also may be a subtle effect of processing, with static cast CF8C-Plus steel heats appearing to be a little stronger than centrifugally-cast heats.

Creep rupture testing further amplifies the differences between CF8C-Plus steel and the standard steel, and both SiMo ductile and Ni-resist austenitic cast irons.

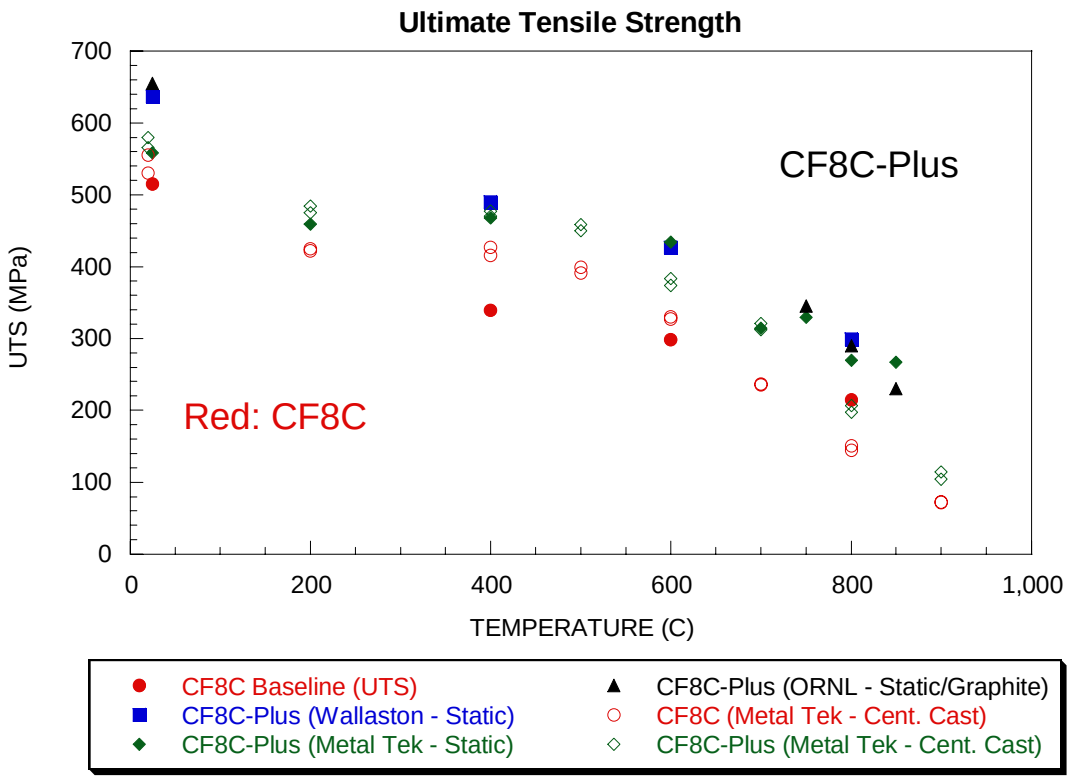

Figure 1 – A plot of ultimate tensile strength (UTS) as a function of test temperature for various commercial heats of standard CF8C and new CF8C-Plus cast stainless steels, including static sand casting or centrifugal casting methods in commercial foundries, and ORNL static casting of small lab-scale heats in graphite molds. There is a clear strength advantage of the CF8C-Plus, particularly at 600°C and above.

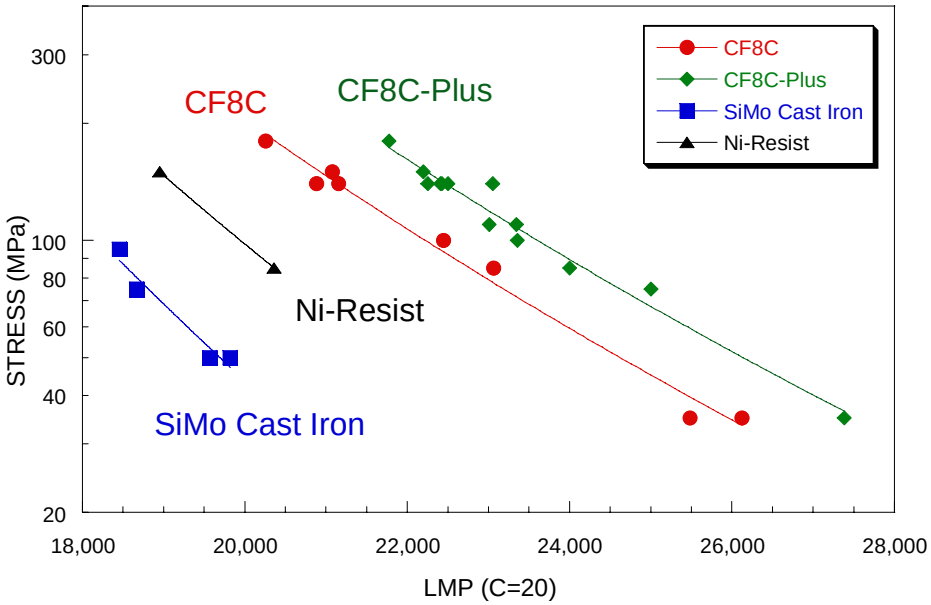

Figure 2 – Creep-rupture stress plotted versus Larson-Miller Parameter (LMP) for various creep-rupture tests run at 500-850°C at ORNL in air of various commercial heats of SiMo ductile and Ni-resist austenitic cast irons, and standard CF8C and new CF8C-Plus austenitic stainless steels. CF8C-Plus shows a significant creep-strength advantage over the standard steel or the cast irons.

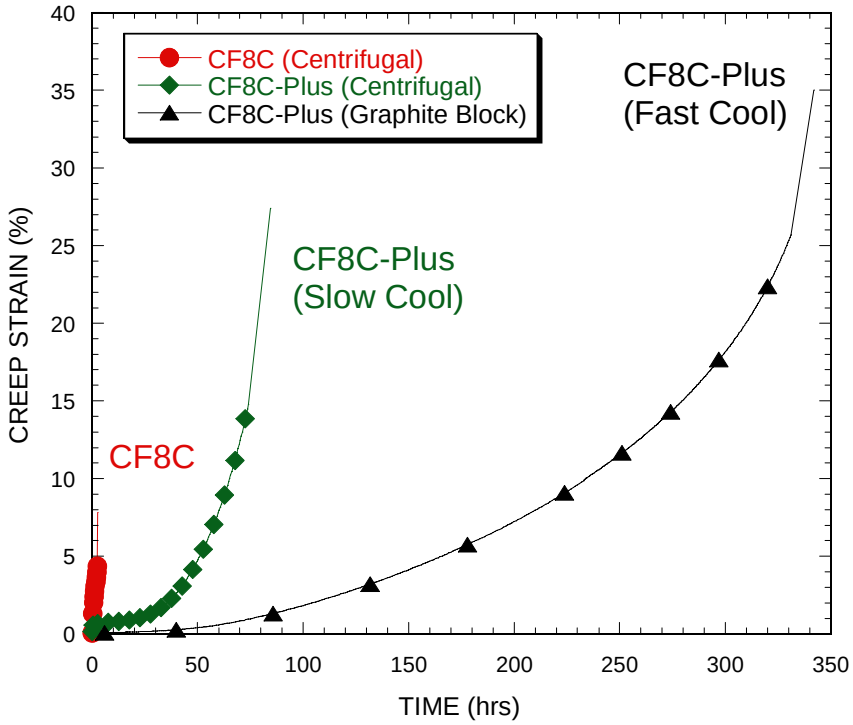

Figure 3 – Comparison of several different steels and cooling rates (CF8C-Plus) for creep-rupture testing at 750°C and 140 MPa in air.

Clearly, the CF8C-Plus steel has 1.5-2 times more creep-rupture strength than the standard CF8C steel, and far greater strength advantages relative to either SiMo ductile or Ni-resist austenitic cast irons. Finally comparison of several creep tests of CF8C-Plus steel made with different casting methods that have different cooling rates indicates that faster cooling rates have a beneficial effect on improving the creep-resistance that are not seen in CF8C steel. This particular property is encouraging for the thinner-walled exhaust components that CF8C-Plus steel is being considered for.

Last quarter, new centrifugally-cast commercial heats of CF8C, CF8C-Plus and the new CF8C-Plus Cu/W modified steels were made by MetalTek. This quarter, specimens were made and tensile and fatigue testing began at MarTest. Results will reported next quarter.

Communications/Visits/Travel

Detailed team communications between ORNL and Caterpillar occur regularly, at least once or twice a week. The new 3 year CRADA began on July 21, 2002, when the previous CRADA ended and is scheduled to end on July 21, 2005. This quarter a two-year CRADA extension was requested at ORNL and Caterpillar.

Status of Milestones

FY 2005 Milestones for Subtask 4.10 – 1) Complete properties measurements of new CF8C-Plus heats, including static and centrifugally cast, at 700-850°C (2/05); **on track**, 2) Commercially scale up new CF8C-Plus heats with Cu/W alloying additions for more high-temperature strength, and complete testing (6/05); **on track**, and 3) Extend the current CRADA for another year or more to complete testing and evaluation of prototype components cast from CF8C-Plus (7/05); **on track**.

Publications/Presentations/Awards

Last quarter CF8C-Plus steel was awarded ORNL Technology Transfer and Economic Development (TTED) Royalty Funds to enable and accelerate commercial scale-up of the new heats with Cu and W added, which continued this quarter and will continue next quarter.

P. J. Maziasz, I. G. Wright, J. P. Shingledecker, T. B. Gibbons, F. V. Ellis, D. A. Woodford, and R. R. Romanosky, "Defining the Materials Issues and Research for Ultra-Supercritical Steam Turbines," invited talk given at 4th International Conference on Advances in Materials Technology for Fossil Power Plants, 25-29, October, 2004, Hilton Head, SC, sponsored by EPRI.

P. J. Maziasz, "Improved Cast Austenitic Stainless Steel – CF8C-Plus," talk given during visit by Shell Exploration and Production and Shell Global Solutions business units to ORNL, 8-9 November, 2004, Oak Ridge, TN.

TEM Study of Microstructures in a Creep-Deformed Tial/Ti_3al Nanocomposite

Luke L. Hsiung
Lawrence Livermore National Laboratory

Objective/Scope

The objective of this effort is to exploit advanced thermomechanical-processing techniques to fabricate in-situ TiAl/Ti_3Al laminate composites containing ultrafine lamellar microstructure with the width of constituent lamellae down to submicron or nanometer length-scales. The LLNL portion of this joint effort is to experimentally verify microstructural stability and mechanical properties (room-temperature ductility and strength, and elevated-temperature creep resistance) of the composites, and to investigate the fundamental interrelationships among processing, microstructures, alloying additions, and mechanical properties of the composites so as to achieve the desired properties and performance of the composites for high-temperature structural applications.

Technical Highlights

We have investigated during the first quarter report-period the microstructures and creep properties of a TiAl(γ)/Ti_3Al(α_2) nanolaminate composite fabricated by the hot extrusion of cast Ti-46.5Al-3Nb-1W-0.1B (1W hereafter) alloys at 1350°C with the extrusion ratio of 1:5. The steady-state creep rate of the nearly fully-lamellar 1 W composite tested at 760°C under stresses ranging between 75 MPa and 500 MPa is shown in Fig. 1. Similar to previously reported creep data of fully-lamellar Ti-47Al-2Cr-2Nb hot-extruded at 1400°C, there exists two creep regimes, i.e. low-stress (*LS*) and high-stress (*HS*) regimes, in which a nearly linear or nearly quadratic creep behavior [i.e. steady-state creep rate = $k\sigma^n$, where σ is applied creep stress and $2 > n > 1$] was observed in low-stress (*LS*) regime (i.e. $\sigma < 200$ MPa), and power-law break down ($n > 6$) was observed in high-stress (*HS*) regime (i.e. $\sigma > 200$ MPa). This again suggests that the creep mechanism in *LS* regime is controlled by the movement of interfacial dislocation (i.e. sliding of lamellar interfaces). Figure 2 (a) and (b) show the lamellar microstructure and the dislocation structures, respectively, within as-fabricated and annealed 1W composite. Here, as shown in Fig. 3, we found that deformation mode in *HS* regime is mainly predominated by interface sliding coupled with deformation twinning within γ lamellae [Fig. 3(a)]. In addition, fine needle-like precipitates, presumably B2 phase resulting from the segregation of W, are observed within α_2 lamellae [Fig. 3(b)]. More analytical works need to be done in order to verify the structure and chemical composition of the fine precipitates within α_2 lamellae.

Future Plans

1. Continue collaborating with ORNL to fabricate and characterize the oxidation-resistant class of TiAl/Ti_3Al nanolaminate composites with high Nb content (>10 at. %).
2. Continue creep testing to investigate the creep resistance, microstructural stability, and deformation twinning phenomenon within the laminate composites at elevated temperatures.
3. Conduct a new gas-gun experiment in order to investigate the impact strength and impact damage mechanisms of the nanolaminate composites.

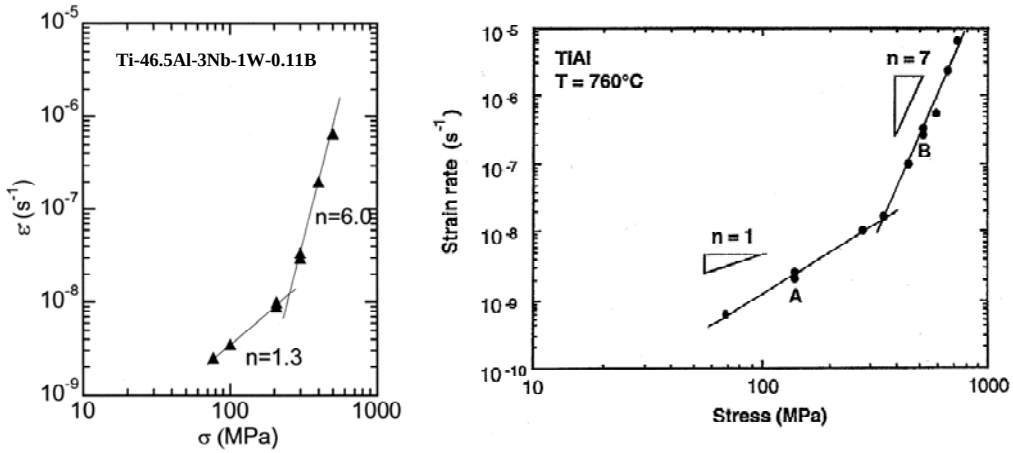

(a) (b)

Fig. 1. Steady-state creep rate plotted as a function of applied stress at 760° for (a) the currently investigated Ti-46.5Al-3Nb-1W-0.1B, (b) previously investigated Ti-47Al-2Cr-2Nb.

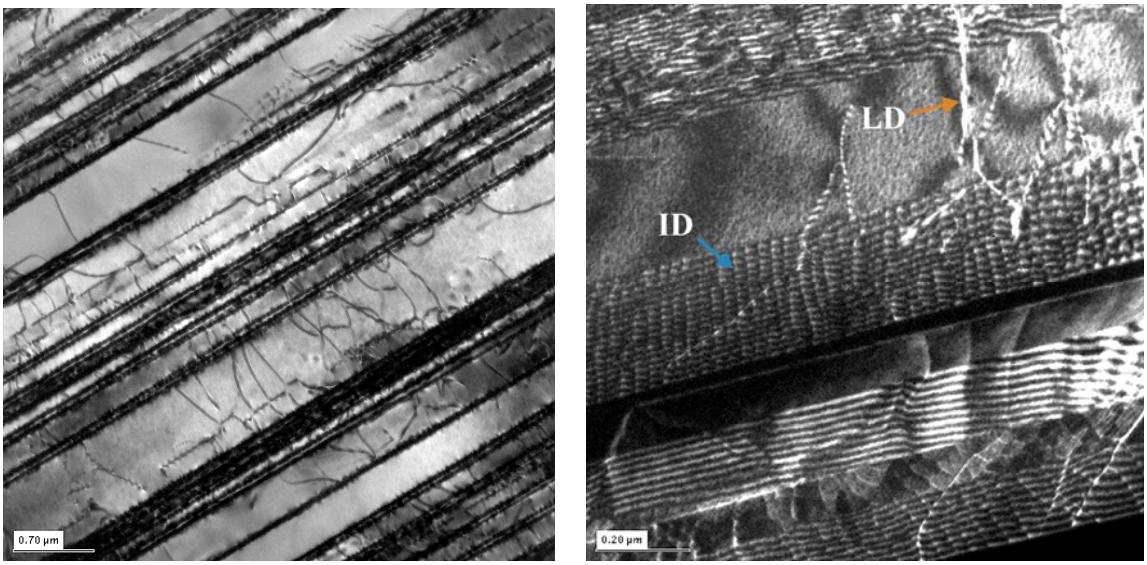

(a) (b)

Fig. 2 (a) A bright-field TEM image shows a typical lamellar microstructure of 1W composite; (b) A dark-field TEM image shows microstructures of interfacial dislocations (ID) and lattice dislocations (LD).

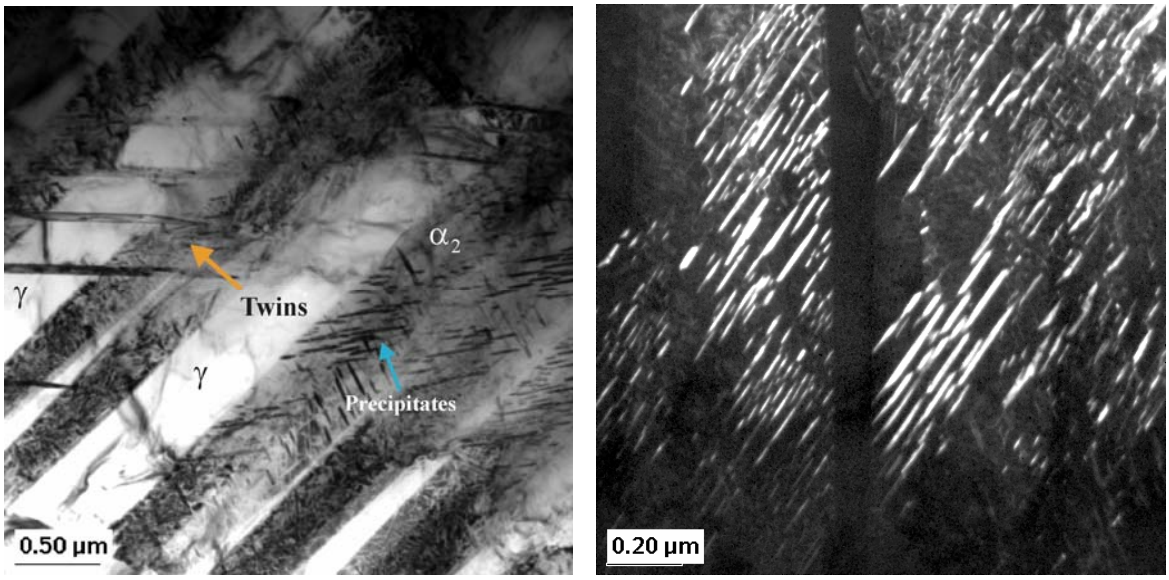

(a) (b)

Fig. 3 (a) A bright-field TEM image shows the formation of deformation twins in γ lamellae and fine B2 precipitates in α_2 lamellae within a 1W sample creep-deformed at 760°C, 500 MPa. (b) a dark-field TEM image shows the morphology and a high density of B2 precipitates (appeared as a bright contrast) within α_2 lamellae.

High Density Infrared Surface Treatment of Materials for Heavy-Duty Vehicles

T. N. Tiegs, D. C. Harper, F. C. Montgomery, and C. A. Blue
Oak Ridge National Laboratory

Objective/Scope

High Density Infrared (HDI) technology is relatively new to the materials processing area and is gradually being exploited in materials processing. For many applications in heavy-duty vehicles, superior properties, such as corrosion and wear resistance, are only required at the material surface. The project using HDI technology will be exploratory and will examine (1) application of wear-resistant coatings, and (2) modification of plasma-sprayed coatings.

Technical Highlights

Earlier work had shown that adherent coatings of hardmetal compositions could be applied to a variety of metal substrates (D-2 tool steel, 4140 alloy steel, and cast iron). However, a problem with the earlier coatings was that a preheat step was required to minimize sintering of the slurry coating prior to bonding with the substrate. When the slurry coating was heated too fast, it tended to peel off from the substrate and crack. The preheating step allowed the substrate to get hot enough so bonding occurred.

Samples are in the process of being fabricated that will use WC and TiC particles only for the coating. The sintering temperature for these plain carbides is significantly higher than the melting point of the substrates. Consequently, because no binder additions (i.e. Ni or Ni_3Al) will be present, sintering and cracking will be inhibited. This will allow the coating to heat up to a sufficiently high temperature so that the underlying substrate will melt and be wicked into the coating by capillary action. Previous work has shown that WC-cast iron composites have excellent wear behavior, so these will be the initial compositions.

Status of Milestones

On schedule.

Communications/Visits/Travel

None.

Problems Encountered

None.

Publications

None.

High Temperature Aluminum Alloys

Yong-Ching Chen
Cummins Inc.

Objective/Scope

Work at Cummins has identified three potential paths to improve the high temperature strength and fatigue resistance of aluminum casting alloys. These paths have been partially investigated under cooperative agreement DE-FC05-97OR22582. Each path showed some promise and further work is needed to determine the useful applications.

Task 1, Ternary Phase Diagrams

This task involves a ternary phase aluminum alloy utilizing rare earth metals to provide precipitate size control and stability. Limited information on these alloys indicates high temperature strength and stability, however, the predicted cost of the alloy is high. Additional work shall be performed to determine if additional rare earth (or other metal) elements which produce beneficial properties at a reasonable cost. Cummins shall develop ternary phase compositions by means of modeling of the equilibrium phase diagram, castings and evaluating the properties of alloys identified.

Task 2, NASA-Developed Process

This task involves a conventional aluminum alloy, which has been chemically modified by a process developed at NASA-Huntsville. The elevated temperature properties reported by NASA are attractive, but it is preferred for Cummins to use alloy with lower silicon content. Eck Industries purchased the license for the NASA-developed technology on high silicon casting alloy and has expanded the range to include conventional low silicon casting alloys. Limited testing of these modified conventional low silicon alloys at Cummins has not shown the property improvement anticipated. Physical and mechanical property measurements shall be performed on specimens provided by NASA and by Eck to characterize the material and determine the optimal properties possible by this method.

Task 3, Particulate-Reinforced Alloy

This task involves a particulate loaded aluminum alloy patented by Chesapeake Composites Inc. The nano-phase particulate at 50 volume percent provides adequate high-temperature strength in early experiments, however, the particulate loaded alloy could only be forged or squeeze cast so complex shape capability is limited. Cummins shall fully characterize the specimens previously made to determine the mechanical behavior of the alloy. Casting modifications shall also be investigated to determine shape capability for the alloy.

Task 4, Reporting Requirements

Quarterly report and final reports

Task 5, Quality Assurance Requirements

Technical Highlights

Task 1. Ternary Phase Diagram:

Task Summary

In previous quarters, the ternary phase diagram of the Al-Fe-Mn was developed by using ThermoCalc software. The versatility of the ThermoCalc had been demonstrated. A binary Al-Y phase diagram was then generated by using the ThermoCalc and it was validated against literature data. In the past quarter, the work on thermodynamic assessment of Al-Yb binary by using ThermoCalc was carried out. Figure 1-(a) shows the Al-Yb binary phase diagram obtained from using ThermoCalc with the limited assessment information obtained from the literature. In general, it is in good agreement with the standard phase diagram published in the literature, Figure 1-(b).

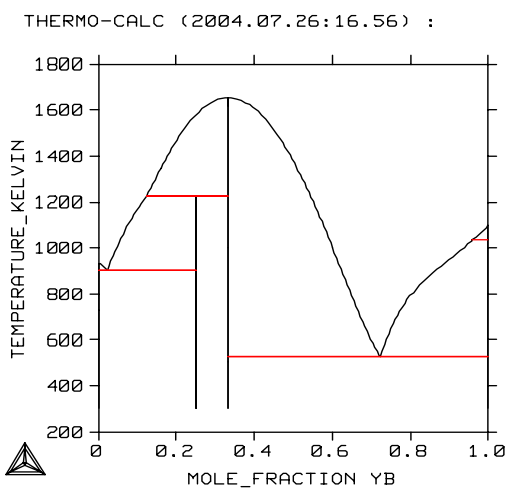

Figure 1-(a). The preliminary Al-Yb phase diagram generated using ThermoCalc.

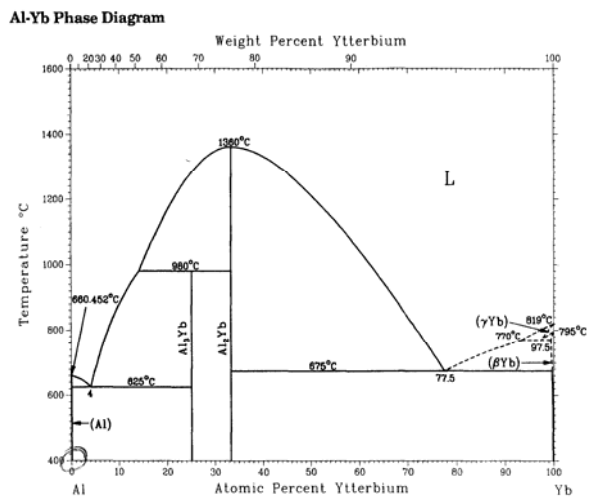

Figure 1-(b). The standard Al-Y phase diagram (in atomic percent).

However, it is important to note that unlike most elements, the rare-earth elements Y and Yb are not widely used. In order for the ternary Al-Y-Yb system to be predicted, the minimum information needed is the assessment of Y-Yb system. Without any experimental data, it is not possible to know if such ternary predictions are accurate or not. So the minimum step we need is to get Y-Yb system otherwise one axis of our ternary diagram may not be correct. We need data in terms of the actual thermodynamics of the system, e.g. heat of mixing, activity data, etc .We have to estimate the actual Gibbs energy for the compounds and then make the fit to the polynomial terms. Much effort in next quarter will be focus on experimentally generating Y-Yb binary phase diagram. This will allow us to predict Al-Y-Yb ternary system.

Task 2. NASA-Developed Process

Task Summary

Extensive mechanical tests were conducted on the NASA 388-T5 and T6 alloys. Tests included elevated temperature tensile tests and rotating beam fatigue tests of samples with or without long-term thermal soaking. Test results were compared to those of the current production materials. Slight improvement in the tensile strength was only realized at test temperatures above 300°C for the NASA 388-T5 alloy as compared to the current materials. The degree of improvement was deemed to be insignificant as compared to the further development needed for the new casting process and prototype trials. The decision was made to discontinue the evaluation work for the NASA 388-T5 alloy for intended application.

The NASA 388-T5 alloy was originally developed for automotive engine components such as pistons to utilize less material, which can lead to reducing part weights, material cost, as well as improving gas mileage and engine durability. The potential application of the NASA 388-T5 alloy in diesel engine pistons was communicated to the piston suppliers. One of the piston suppliers conducted fatigue tests of the NASA 388-T5 alloy and their production aluminum alloy at 350°C. The NASA 388-T5 alloy exhibited slightly better fatigue strength at 350°C than the production aluminum alloy. However, the NASA 388-T5 alloy was found to be difficult to cast in diesel piston size without defects. The piston supplier also decided not to pursue the development of NASA 388-T5 alloy in the piston application.

Task 3. Particulate-Reinforced Alloy

Task Summary

This task involves a nano-phase particulate loaded aluminum alloy patented by Chesapeake Composites Inc. A patented, low cost, liquid metal infiltration process is utilized to produce a billet form ready for secondary operations. This composite material combines the enhanced elevated temperature strength, toughness, and ductility of dispersion strengthened (DS) alloys with the stiffness and low CTE of metal matrix composites (MMC's). It was claimed that this composite can be readily turned using WC tooling and drilled and tapped using high-speed steel tools. Potential applications include pistons, compressor wheel, and engine components.

Initial tensile and fatigue tests of 1090 Al and 2024 Al alloy reinforced with nanoscale Al_2O_3 particles (DSC) at elevated temperatures showed impressive results. Almost 100% improvement in tensile strength and yield strength was obtained on the DSC material as compared to those of the current production materials. No degradation in the tensile strength and fatigue strength was observed in the DSC material after 500 hours of thermal soaking at 400°C.

Extensive microstructural characterization of 2024Al-DSC material has been carried out by Jixong Han and Professor Vijay K. Vasusevan at University of Cincinnati. The attached is the quarterly progress report submitted.

Characterization of New, Cast Aluminum Alloys for High-Temperature Applications

Jixiong Han and Vijay K. Vasudevan
Professor, Department of Chemical and Materials Engineering, University of Cincinnati, Cincinnati, OH 45221-0012
Tel: (513) 556-3103; Fax: (513) 556-3773; Email: vijay.vasudevan@uc.edu

Quarterly Progress Report Submitted to

Dr. Yong-Ching Chen
Technical Advisor, Metallurgical Engineering Division, Cummins Inc.,
1900 McKinley Avenue, Mail Code 50183, Columbus, IN 47201

January 12, 2005

DESCRIPTION OF ACCOMPLISHMENTS

Objectives of Project

The goal of this project was to characterize the microstructure of new, cast aluminum alloys that are being considered for high-temperature diesel engine applications. These include NASA-modified cast Al 388 alloy and an Al-matrix composite dispersion strengthened (DSC) with nanoscale Al_2O_3 particles. In this report, results of the microstructure of a 2024Al-Al_2O_3 DSC material are reported.

Experimental Details

The 2024Al-Al_2O_3 nanoscale particle dispersion strengthened composite (DSC) was prepared by Chesapeake Composites Co. (New Castle, DE) by a casting route. Cut specimens were solution treated at 540°C for 3 h, quenched in cold water and then subjected to artificial aging at 130 and 190 °C for times varying from 1 to 100 h. All the heat-treated samples were encapsulated in evacuated and Argon back-filled Pyrex capsules to prevent oxidation. Tensile properties of the DSC material were determined by Cummins Inc. at a range of temperatures from ambient to ~700 °F. Samples in the as-cast condition, as well as those thermally soaked for times of 500 hours at each temperature were tested. The Vickers microhardness was measured on a LECO M400-H1 hardness-testing machine using a load of 300 g for an indentation period of 20 s. At least seven hardness values from different locations well distributed on the sample surface were measured for each sample in order to eliminate possible segregation effects, and the average value of the measurements was considered to be the microhardness of the sample. The volume fraction of Al_2O_3 was measured by systematic point counting method as well as computer image analysis.

The materials in various conditions and accompanying microstructural changes were characterized by a variety of methods, including X-ray diffraction, optical microscopy (OM), secondary and back-scattered electron (BSE) imaging in a scanning electron microscope (SEM) and transmission electron microscopy (TEM). XRD observations were performed using a Philips X′Pert X-ray powder diffractometer operated at 40 KV and 50 mA. Metallographic samples were mounted and wet ground on silicon carbide grinding paper using water as lubricant. Polishing was carried out using 6 μm and 1 μm diamond paste. Finally polishing was being

done on a polishing cloth using colloidal silica, which was a suspension of 0.05 μm SiO_2 particles. Thin foil samples for TEM examinations were prepared as following. Small discs with 3 mm diameter were first punched out from the polished slice which cut from as-cast or annealed samples; after that they were mechanically grinding to 100 μm, followed by dimpling (Fischione Instruments Model 150 Dimpling Grinder) to 20 μm, and finally Ar+ ion milling (Fischione Instruments Model 1010 Low Angle Ion Milling and Polishing System). Observations of the thin foils were conducted in a Philips CM20 TEM operated at 200 kV and photographs under bright field (BF), dark field (DF), weak-beam dark field (WBDF), selected area diffraction (SAD) and convergent beam electron diffraction (CBED) modes were recorded. The fracture morphologies and failure mechanisms in the tested samples of the DSC material were studied by SEM (Philips XL-30 ESEM and Hitachi S-4000) to characterize the predominant fracture mode and the fine-scale features on the tensile fracture surface. Samples for TEM observation were obtained from the deformed tensile specimens by sectioning parallel to the fracture surface.

Results and Discussion

As-received 2024 Al-Al_2O_3 Material

Microstructural characterization studies carried out on the as-received materials (Fig. 1) revealed the presence of Al_2O_3 particulates as the most predominant phase distributed in the metallic matrix, which was confirmed by EDS analysis. The SEM results indicated good interfacial bonding between the Al_2O_3 particulates and the matrix. The Al_2O_3 particles are more or less spherical and a few of them had sharp corners. The agglomerations of Al_2O_3 particles were non-uniform in size and irregularly shaped, and particulate-rich and particulate-free regions, together with some porosity, were present. Figure 2(a) is a typical bright-field TEM image of the as-received material. The Al_2O_3 particles are basically spherical with particles size varying from 100 nm to 500 nm. Figure 2(b) is the EDS profile of the Al matrix. Figure 2(c) is the EDS profile of the Al_2O_3 particle, which confirms that it is Al oxide. Again, the Al_2O_3 particle size distribution for this composite was not uniform, i.e. was essentially bimodal.

Solutionized + Water Quenched and Aged 2024Al-Al_2O_3 Material

Samples cut from the composite material were solution treated isothermally at 540°C for 3 h to dissolve any precipitates prior to cold-water quenching. Generally speaking, the solubility of the alloying elements in α phase increases with increasing solution treatment temperature. At approximately 500 ^{o}C, the solubility of the alloying elements in the α-Al phases reaches a maximum [1]; and water quenching will retain the solubility of the alloying elements; hence prohibit the formation of the precipitates. However, in the present case, many precipitates were present in the Al matrix (Fig. 3) of the solutionized and quenched sample, which is indicative of an ineffective solutionizing treatment. Further work, including repetition/optimization of the solutionizing treatment, is underway to ascertain whether the precipitation is due to faulty heat treatment or a real effect. Both θ' and S' precipitates were present.

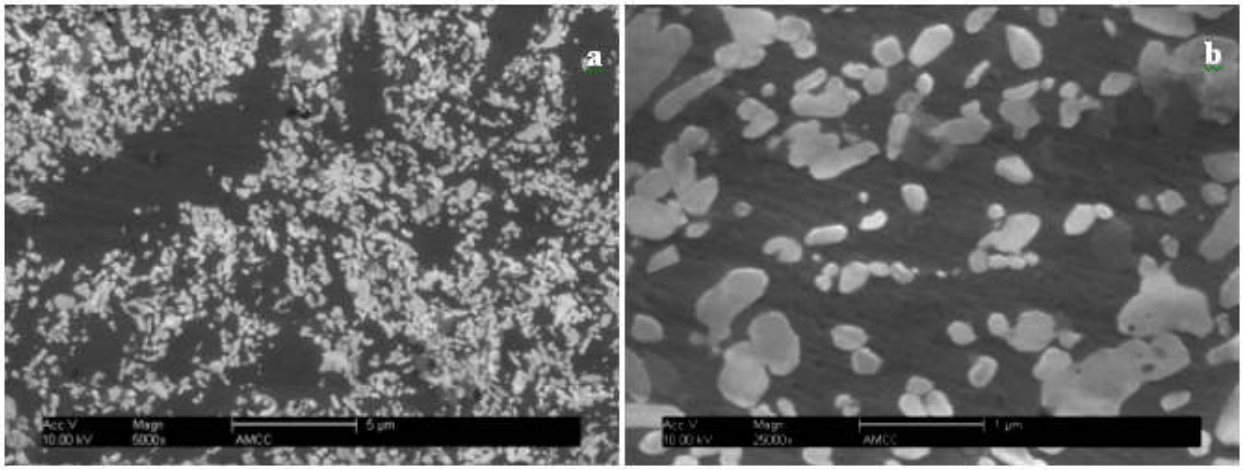

Figure 1. SEM micrographs showing the microstructure of the 2024Al-Al_2O_3 DSC material as infiltrated: (a) low magnification; (b) high magnification.

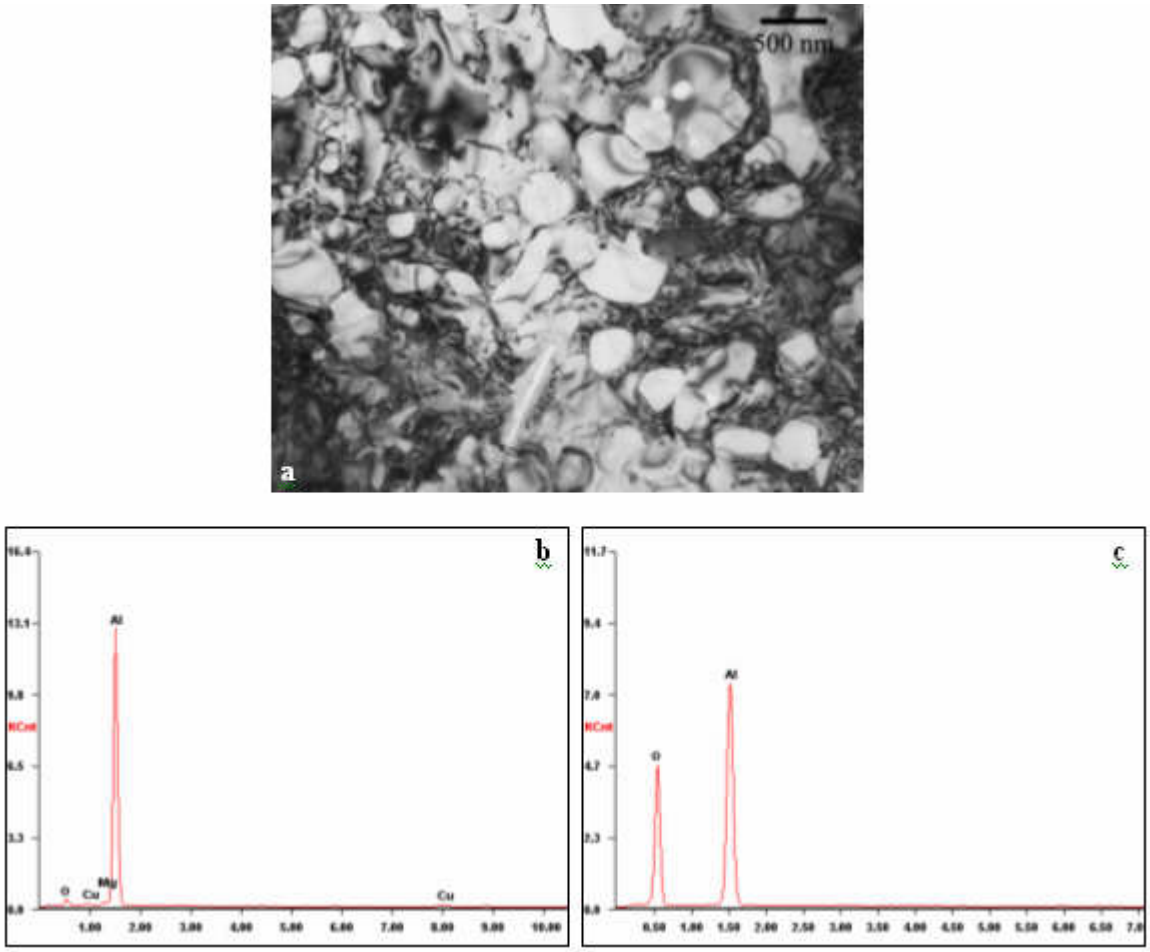

Figure 2. (a) BF-TEM micrograph showing typical microstructure of the as-received 2024Al-Al_2O_3 DSC material; (b) EDS spectrum from the Al matrix; (c) EDS spectrum from the Al_2O_3 particles.

The solutionized and water quenched samples were then aged at 130°C and 190°C for times from 1 to 100 h. It is well known that the aging of the 2024 aluminum alloy leads to a precipitation sequence as follows [2]:

$$\text{Supersaturated } \alpha\text{-phase} \rightarrow \text{GPI} \rightarrow \text{GPII or S}'' \rightarrow \text{S}' \rightarrow \text{S } (CuMgAl_2)$$

Solution treatment of the alloy introduces vacancy sites, which are retained after quenching. These vacancy sites are preferential nucleation areas of GPI zones, which are disc-shaped clusters of constituent atoms. Upon aging for a longer time, formation of ordered zones takes place (known as GPII zones) in the form of cylinders coherent with the surrounding matrix (α-phase). Subsequently, the volume fraction of GPII zones or S″ phase is maximized and at the same time S′ phase appears when the peak aged condition (maximum hardness and mechanical strength of the alloy) is reached. Upon subsequent aging, S′ phase loses its coherency with the matrix and is replaced by the S phase in the overaged condition.

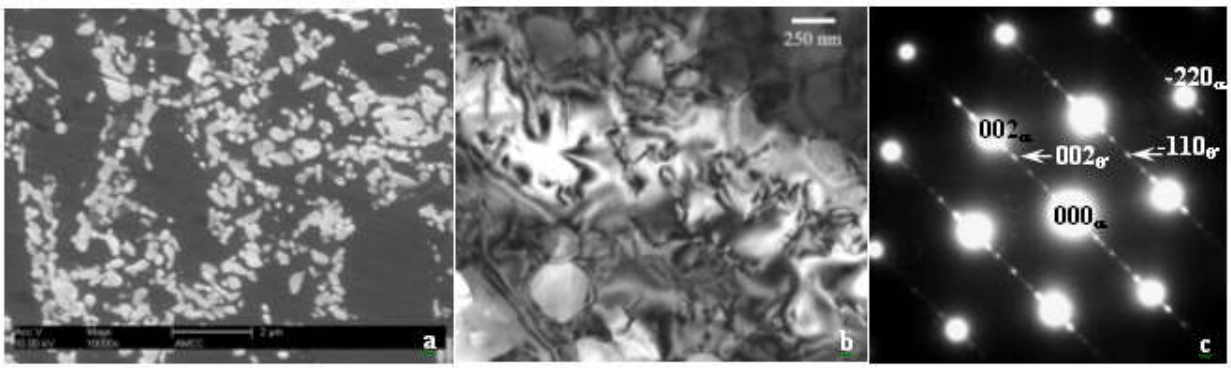

Figure 3. Electron micrographs showing the microstructure of the 2024Al-Al_2O_3 as solutionized and water quenched: (a) SEM micrograph; (b) DF-TEM image; (c) [110]Al // [110] θ' SAD pattern of (b).

The microstructure development of 2024Al-Al_2O_3 composite in response to aging treatment at 130 ^{o}C for various times is shown in the series of TEM micrographs provided in Figure 4~6. A number of needle-shaped of S′ (Al_2CuMg) phase, which is the main precipitate in the 2024 alloy for the 1 h of aging time, precipitated from the solid solution, as shown in Fig.4. The S′ is uniformly distributed in Al matrix.

Figure 5 shows the microstructure of 2024Al-Al_2O_3 aged at 130 ^{o}C for 10 h. Both BF and DF image demonstrate that the precipitates are uniformly distributed in the matrix material. There does not appear to be any precipitate-free zone or preferential (excess) precipitation at or near the particle-matrix interface. The micrographs of Fig. 6 show the microstructure of the composite aged to 100 h. A uniform, high density of S′ precipitates in the matrix can be seen in Fig. 6(a).

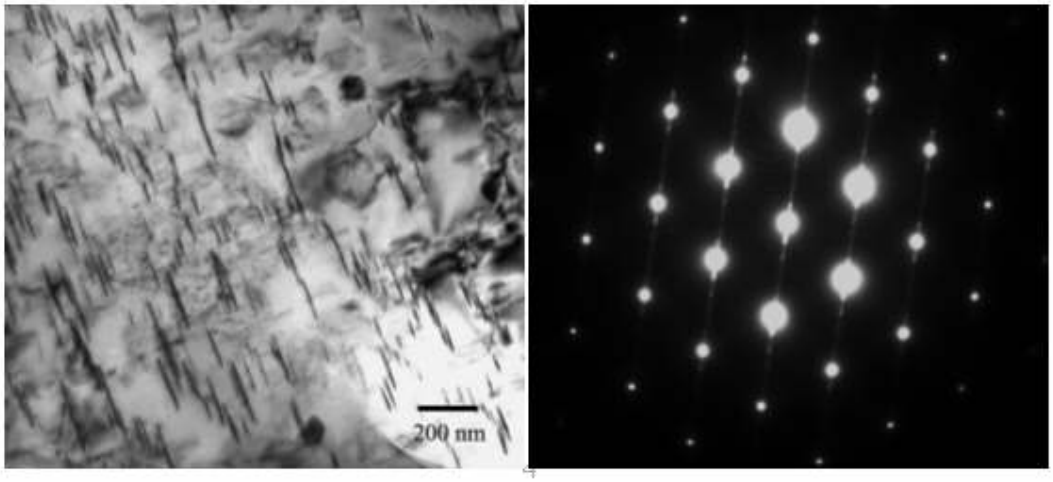

Figure 4. TEM micrographs showing the microstructure of the 2024Al-Al_2O_3 aged at 130°C, 1 h: (a) BF-TEM image; (b) [110] Al SAD pattern of (a).

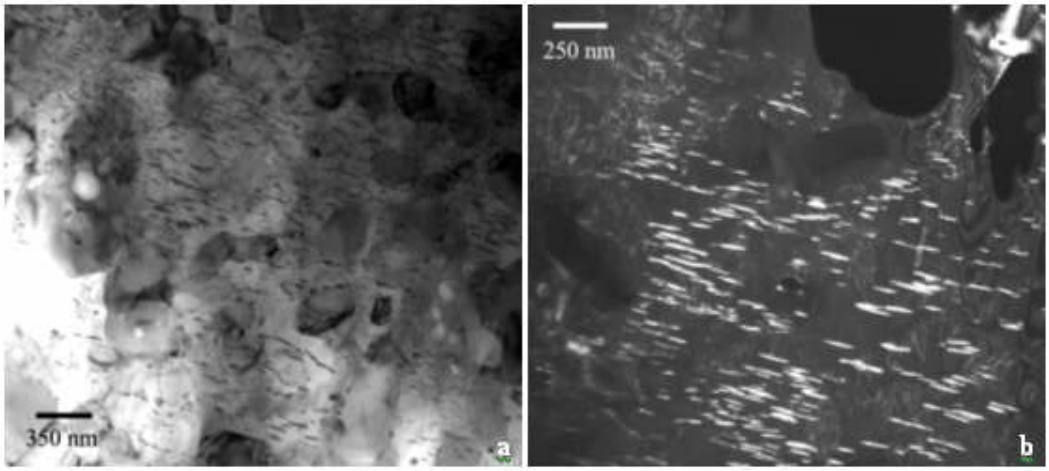

Figure 5. TEM micrographs showing the microstructure of the 2024Al-Al_2O_3 aged at 130 ^oC, 10h: (a) BF-TEM image; (B) DF-TEM image from an S' precipitate reflection.

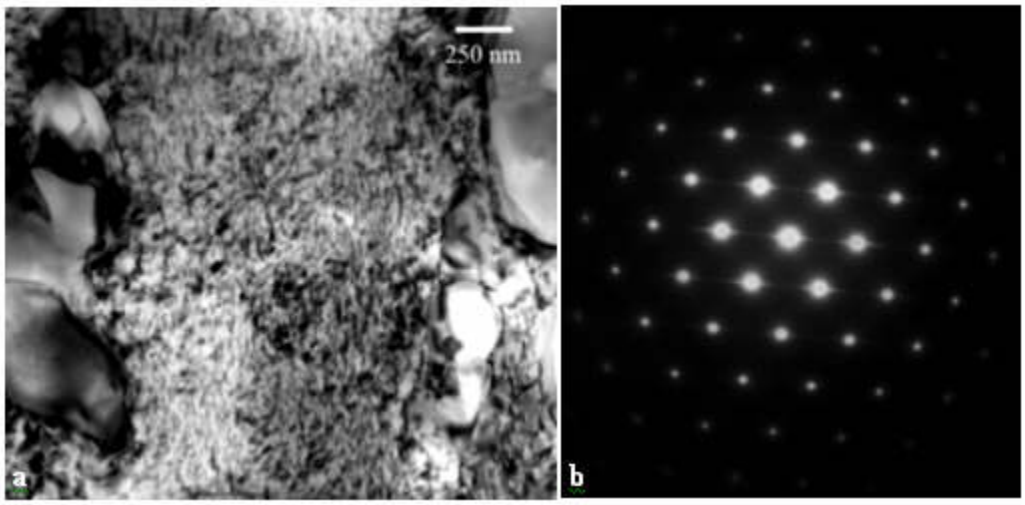

Figure 6. TEM micrographs showing the microstructure of the 2024Al-Al_2O_3 aged 130°C, 100 h: (a) BF-TEM image; (b) [110] Al SAD pattern of (a).

Microstructural development in the 2024Al-Al_2O_3 composite in response to aging treatment at 190°C for various times is shown in Figures 7~9. A common characteristic in the microstructures of the composites with different aging conditions is that coarse S′ precipitates are densely distributed in the regions where quite a few Al_2O_3 particles exist, as shown in Figs. 4a, 7a, and 8a. The tiny S′ precipitates are sparsely distributed in the regions where particles are dense, as shown in Fig. 5a, 9a. This is probably because a greater areal fraction interfaces are present in the sub-micron particle reinforced composite, and those interfaces could act as an aggregation site for the alloying elements and cause reduced solute atom concentration in the matrix away [3]. Therefore, it can be assumed that the solute atom concentration is lower in the dense particle regions. Also, the interspace between particles is very small; hence, it is difficult for the solute atom to migrate. For this reason, the nucleation and growth of the precipitates were suppressed to some extent in the regions where the particles are dense.

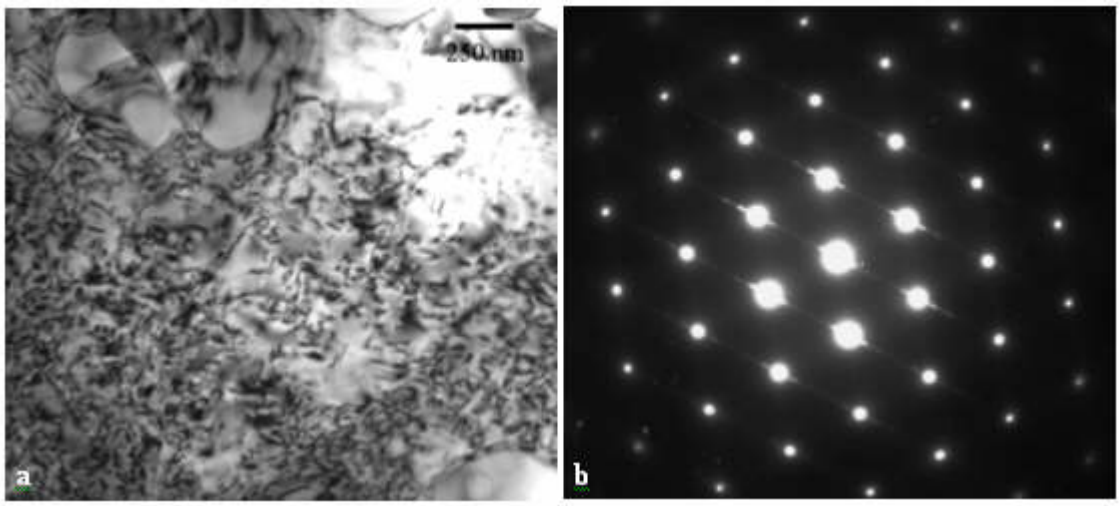

Figure 7. TEM micrographs showing the microstructure of the 2024Al-Al_2O_3 Aging 190°C, 1h: (a) BF-TEM image; (b) [110] Al SAD pattern of (a).

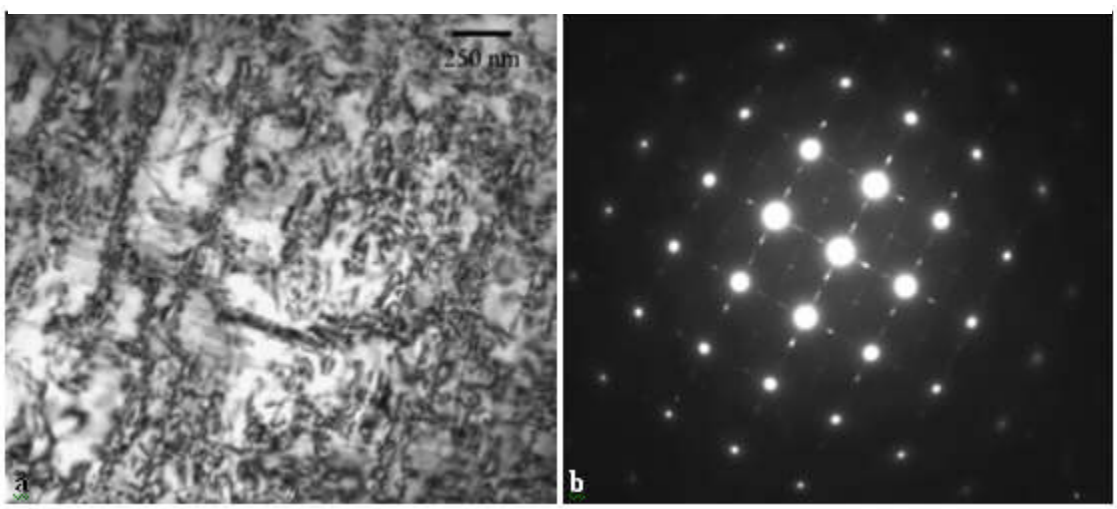

Figure 8. TEM micrographs showing the microstructure of the 2024Al-Al_2O_3 Aging 190°C, 10h: (a) BF-TEM image; (b) [001] Al SAD pattern of (a) showing reflections from S' and θ'.

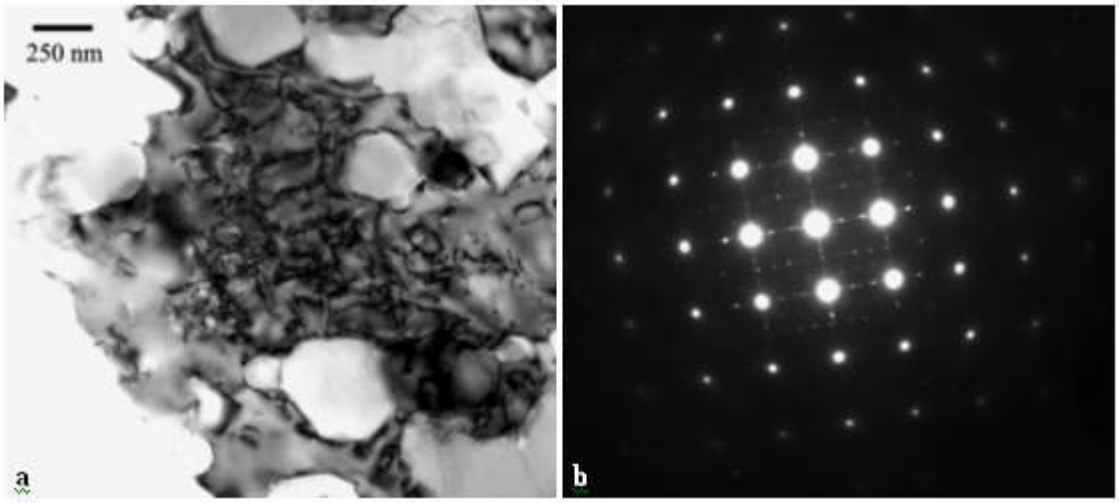

Figure 9. TEM micrographs showing the microstructure of the 2024Al-Al_2O_3 Aging 190°C, 100h: (a) BF-TEM image; (b) [001] Al SAD pattern of (a) showing S' and θ' reflections.

The TEM observations gave evidence for an accelerated aging phenomenon in this 2024Al-Al_2O_3 composite, which was also confirmed in the microhardness data shown in Fig. 13. The accelerated aging phenomenon was hypothesized to be a consequence of the short-circuit path for pipe diffusion of solutes, which is induced by the high dislocation densities and interfacial stresses resulting from the reinforcement [4]. A previous study conducted by Christman and Suresh on 2124Al-SiC composite reported similarly accelerated aging. They found the increased dislocation density facilitates the nucleation of precipitates whereby the incubation time for precipitates nucleation and the aging time to achieve peak hardness in the matrix are significantly reduced for the composite as compared to the unreinforced matrix material [5].

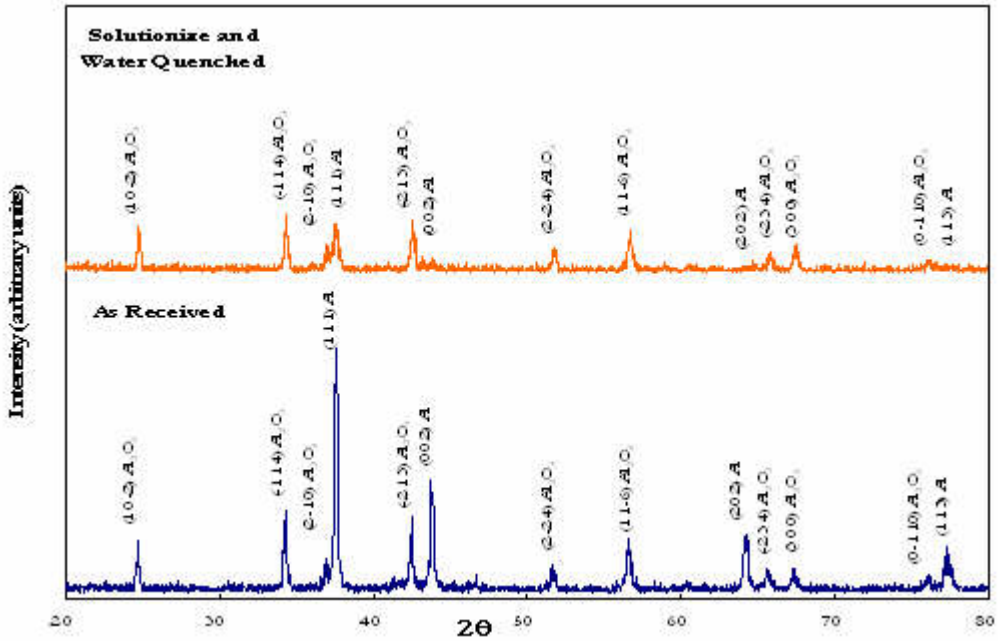

Figure 10. XRD pattern of the 2024Al-Al_2O_3 composite as received, solution treated and water quenched.

Figure 10~12 are the X-ray diffraction patterns of the as received, solutionized+WQ, and the aged specimens. For both of ageing conditions (130°C and 190°C), the X-ray diffraction patterns indicate the presence of Al_2CuMg (S′) in addition to Al and Al_2O_3 phases.

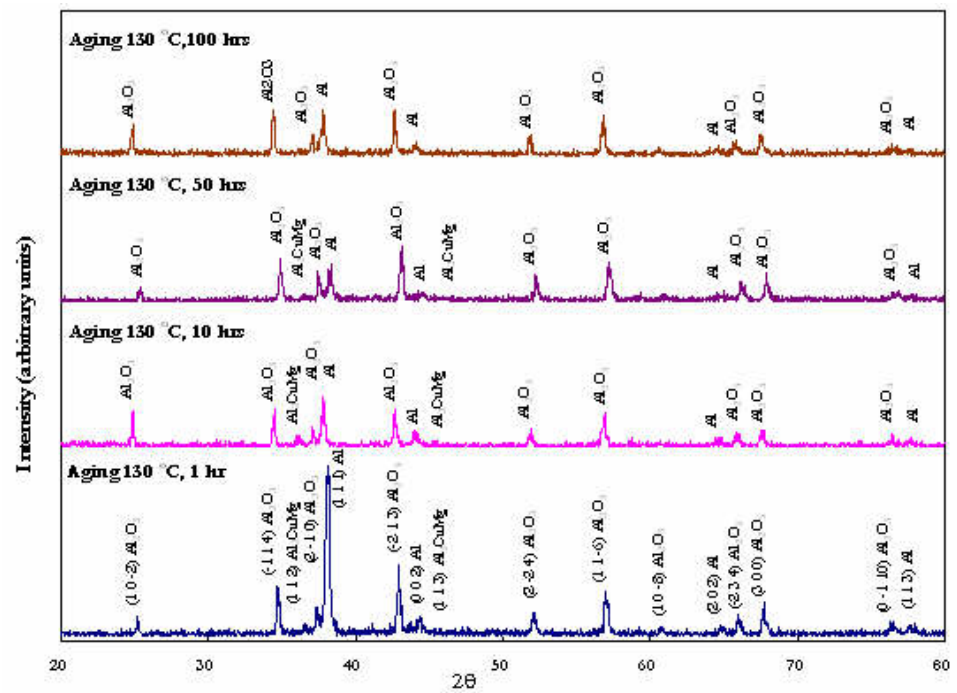

Figure 10. XRD pattern of the 2024Al-Al_2O_3 composite as received, solution treated and water quenched.

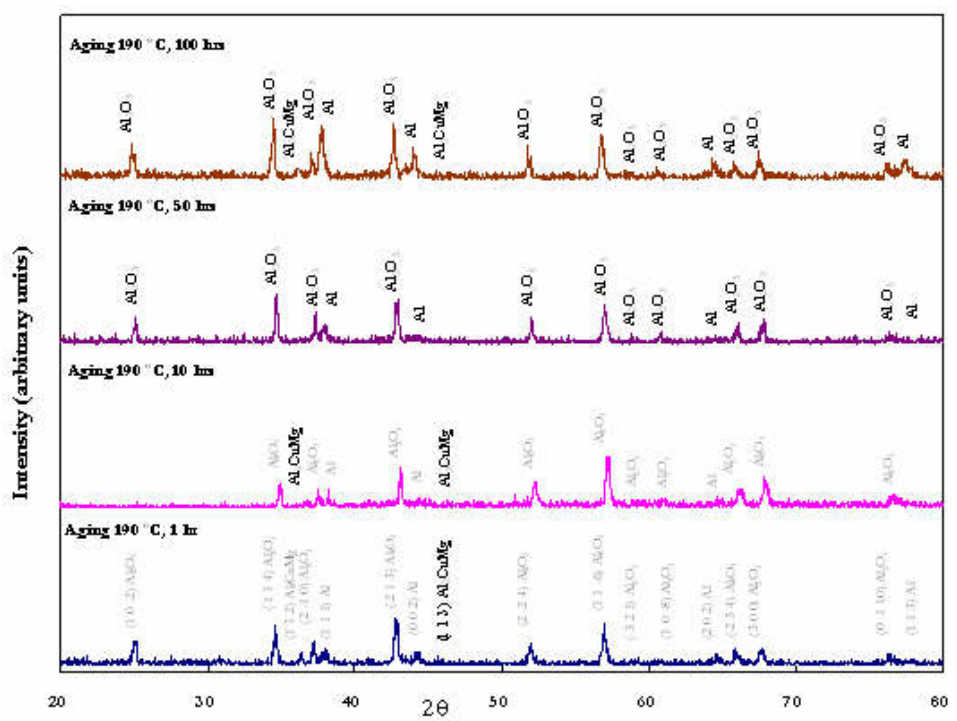

(*Figure 12. XRD pattern of the 2024Al-Al_2O_3 composite after aging at 190°C for various times.*

Figure 13 shows the variation of microhardness as a function of aging time for 2024Al-Al_2O_3 composite aged at 130°C and 190°C. Generally speaking, the aging time at peak hardness for the unreinforced all 2024 alloys is about 10 h [6]. However, the composite material reaches peak hardness after only 1 h of aging, which confirms the accelerated aging phenomenon we have discussed previously. Overaging and drop in hardness was observable at 190°C. Solution treatment and water quench greatly improve the microhardness of the composite. This is particularly because the dislocation generation due to thermal expansion mismatch between Al matrix and Al_2O_3 reinforcement.

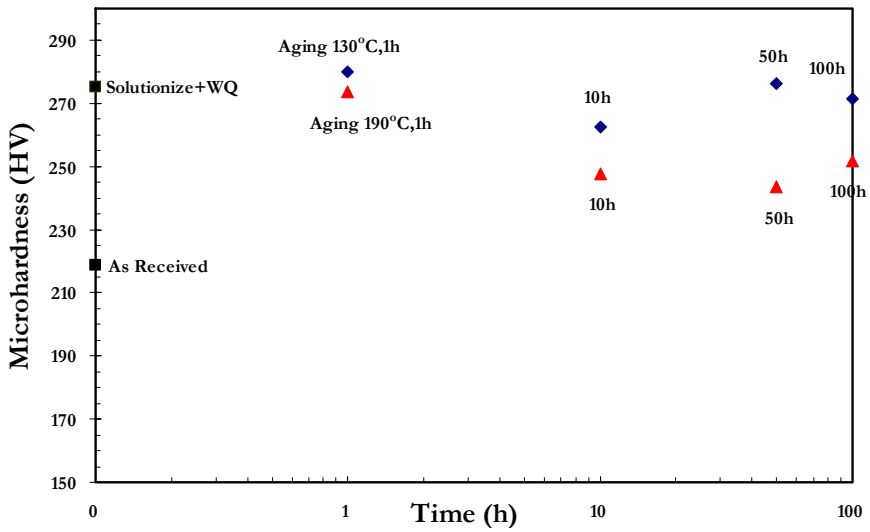

Figure 13. Variation of microhardness as a function of aging time for the 2024Al-Al_2O_3 composite.

Dislocation Structures in Tensile-Deformed Materials

Fig. 14 shows the dislocation structures in the as-infiltrated 2024Al-Al_2O_3 composite material. The dislocation density in the matrix of the as-infiltrated composite is quite high. Dislocations were generated during the casting process due to the thermal misfit stress developed as a result of the difference in the coefficient of thermal expansion of the matrix and the reinforcement phase, which will be discussed in detail later.

Fig. 15 shows the dislocation structures in the solutionized + water quenched 2024Al-Al_2O_3 composite material. The dislocation density is very low, which is an exception to the generally observed high dislocation density in solution treated and water quenched particle reinforced Al matrix composites. As mentioned previously, many precipitates were present in the Al matrix, which is unexpected for solutionized and quenched condition. The reason for this is not clear yet, and is being investigated. However, the fine precipitates were well dispersed and the fraction of interfaces increased enormously. Thus, the thermal misfit stress could bring about plastic strain gradient near the interfaces, and hence the stress around the dispersoids became relatively uniform. This appears to be the reason for the low dislocation density in the solution treated and water quenched composite material.

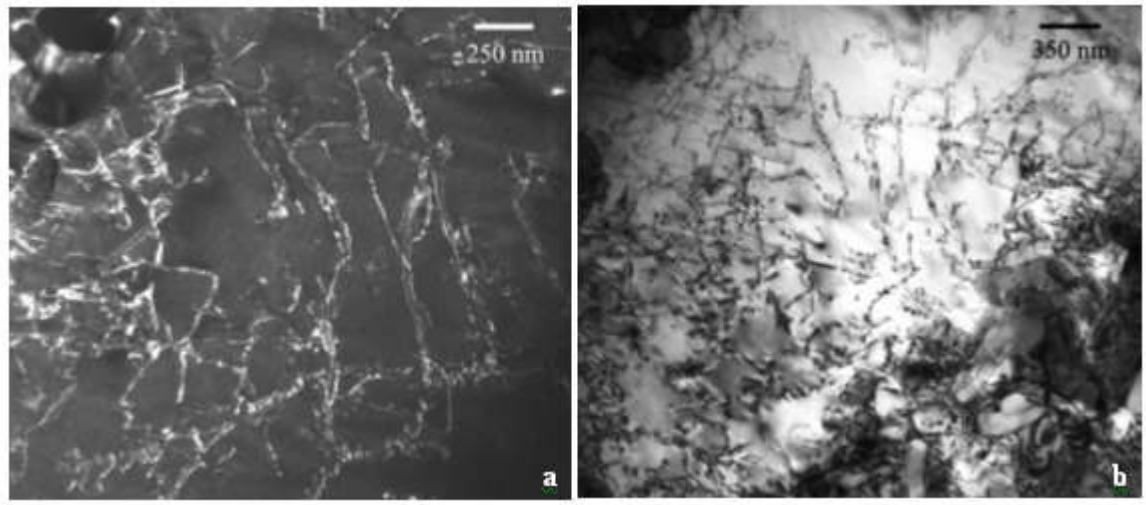

Figure 14. TEM micrographs showing the dislocation structures in the as-received 2024Al-Al_2O_3 material: (a) WBDF-TEM image; (B) BF-TEM image.

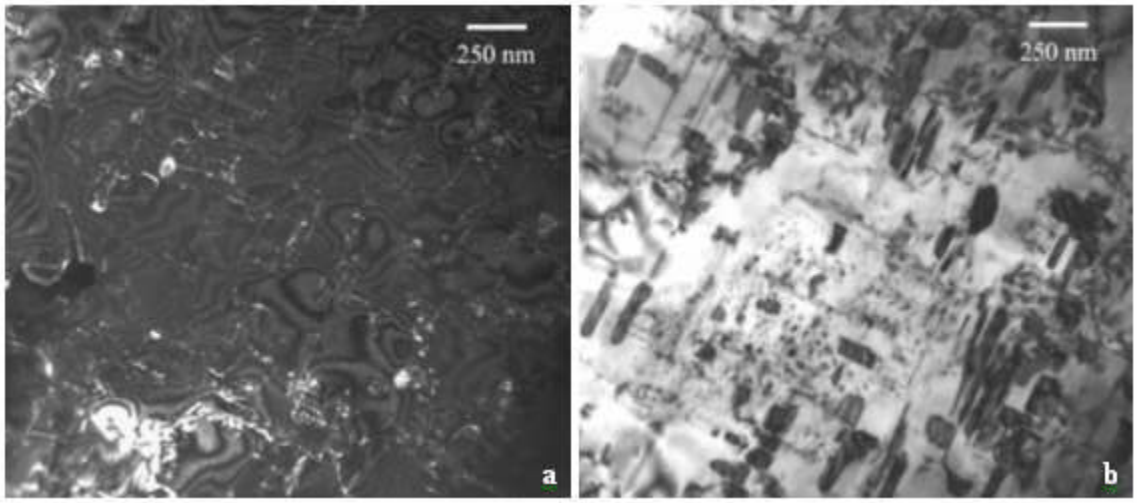

Figure 15. TEM micrographs showing the dislocation states of the 2024Al-Al_2O_3 as solutionized + water quenched material: (a) TEM DF (dark field) image; (B) TEM BF (bright field) image (precipitates).

The dislocation structures in the tensile test samples of the 2024Al-Al_2O_3 composite are shown in Figure 16. The dislocation density in the matrix of the room temperature tensile tested specimens was very low, and only a few dislocations can be seen in the matrix (see Fig. 16a), which is consistent with the low ductility observed for this sample. There was a small increase in the dislocation density in the non-thermally soaked 500°F- (Fig. 16b) and 700°F-tested (Fig. 16c) samples. However, the dislocation density in the matrix of the 500 h-thermally-soaked 500°F and 700°F-samples (Figs. 16d and 16e) was quite high, and dislocation tangles can be seen. The high density of dislocations in the matrix suggests that heavier plastic deformation had been induced in the matrix during the tensile test at higher temperatures, which is consistent with the small increase in ductility observed for these test conditions. The dislocation generation mechanism proposed by Arsenault and Fisher [7] to account for this high dislocation density is based on the large difference in coefficients of thermal expansion (CTE) of Al matrix materials and particles reinforcement phases. In the present case, the CTE of Al and Al_2O_3 have been

reported to be 25×10^{-6} $^{o}C^{-1}$ and $6.5\text{-}8.8\times10^{-6}$ $^{o}C^{-1}$, respectively [8], i.e. a factor of ~ three difference. When the composite is cooled from elevated temperatures of annealing or processing, misfit strains occur due to differential thermal contraction at the Al/Al_2O_3 interface, which is sufficient to generate dislocations. In addition, dislocations could also be introduced into this composite during plastic deformation at high temperatures, which may not be annihilated and could be trapped by the Al_2O_3, resulting in a high dislocation density in the high temperature tested samples.

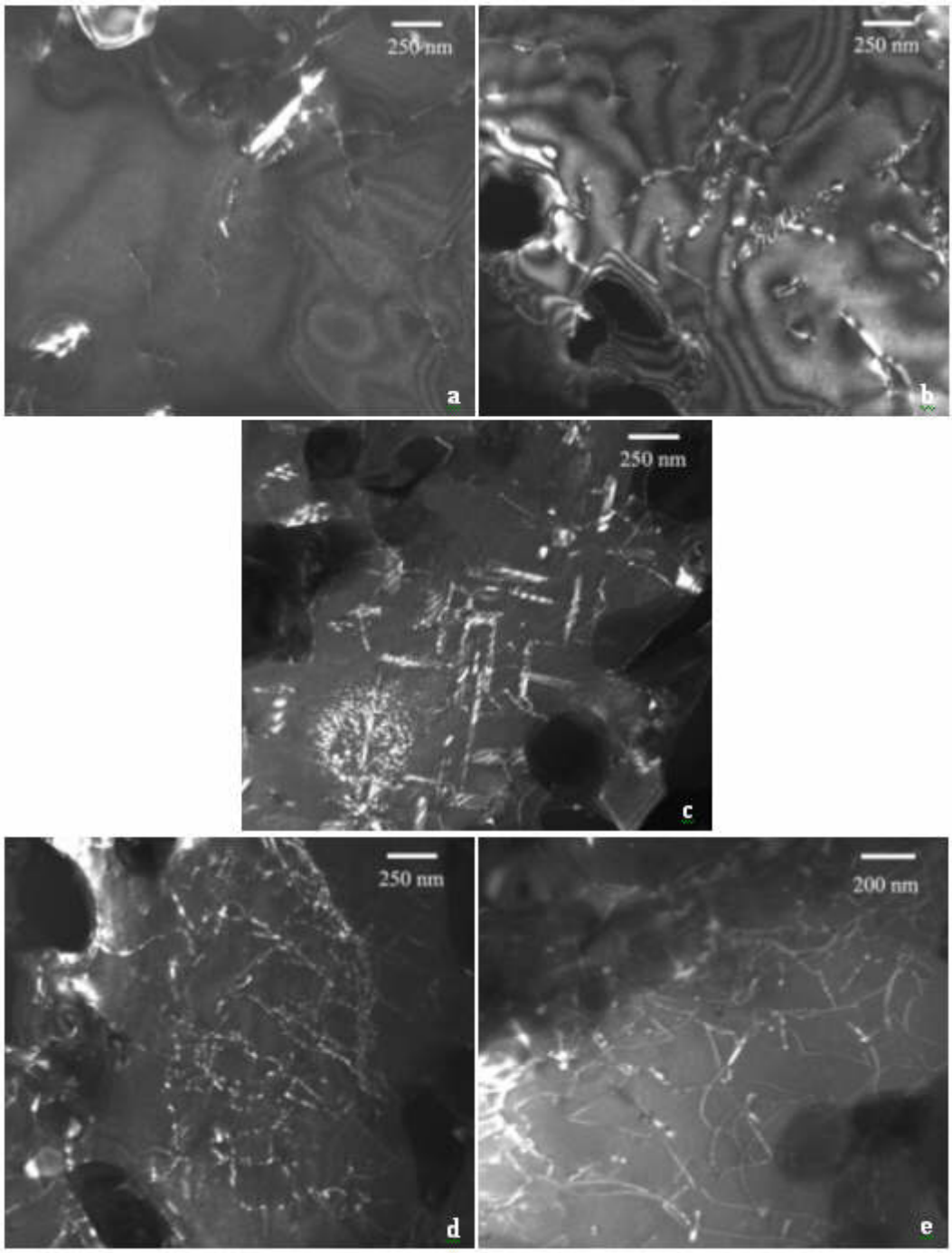

Figure 16. WBDF-TEM micrographs of the tensile test specimens of the 2024Al-Al_2O_3 composite, (g=[111]): (a) 25°C/no thermal soaking; (b) 500°F/no thermal soaking; (c) 700°F/no thermal soaking; (d) 500°F/thermal soaking for 500 h; (e) 700°F/thermal soaking for 500 h.

In this investigation, particular attention was focused on developing an understanding of microstructural development in a 2024Al-Al_2O_3 composite during heat treatment. An accelerated aging phenomenon has been reported, which is attributed to the increase in dislocation density due to Al_2O_3 reinforcement. TEM analysis of the aged samples revealed the presence of θ' and S' precipitates, which were generally quite stable at 130°C, but underwent some coarsening with a concomitant drop in hardness following aging at 190°C. The dislocation density in room-temperature tensile-tested samples was quite low, which was consistent with the low ductility at this temperature. On the other hand, the dislocation density in samples thermally-soaked and tested at higher temperatures (500 and 700°F) was high. This is thought to be associated with the combined effect of ease of plastic deformation at high temperatures, coupled with differential thermal contraction of Al and Al_2O_3 on cooling from the elevated temperatures of testing.

Future Work

Detailed TEM, SAD and EDS analysis of the microstructural changes, particularly focused on precipitation and dislocation structures of the 2024Al-Al_2O_3 composite is on going to fully establish and better understand the transformation sequence, microstructure evolution and deformation mechanisms.

Reference

1. D.R. Sun, X.C. Sun, D.O. Northwood, and J.H. Sokolowski, Mater. Charact., 36, 83-92 (1996).

2. G.E. Kiourtsidis, S.M. Skolianos, G.A. Litsardakis, Mater. Sci. and Eng., A382, (2004) 351-361.

3. X.F. Wang, G.H. Wu, D.L. Sun, C.J. Qin, Y.L. Tian, Mater. Lett., 58, (2004) 333-336.

4. T.G. Nieh and R.F. Karlak, Scripta Metall., 18, 25 (1984).

5. T. Christman, and S. Suresh, Acta Metall., 36, 1691-1704 (1988).

6. C. Badini, F. Marino, E. Verne, Mater. Sci. and Eng., A191, 185-191 (1995).

7. R.J. Arsenault and R.M. Fisher, Scripta Metall., 17, 67 (1983).

8. J.P. Schaffer, A. Saxena, S.D. Antolovich, T.H. Sanders and S.B. Warner, in: The Science and Design of Engineering Materials, Richard D. Irwin, Inc. (1995), p. 572

Applications of Titanium Alloys for Heavy-Duty Vehicles

Paul C. Becker
Oak Ridge National Laboratory

In this quarter, the following tasks will be reported on:

1) Ti-6-4 alloy as a replacement for cast iron in diesel engine heads and blocks.
2) Mg alloy to replace cast iron in diesel engine heads and blocks.
3) Slurry cast process (SLP) for Al alloys for improved fatigue resistance.

Task 1: Explore the use of Ti-6-4 alloy as a replacement for cast iron in diesel engine heads and blocks.

1. The modeling showed that by using Ti-6Al-4V for the head and block in conjunction with using a Be-Cu insert in the valve bridges, the engine could be run at 3200 psi peak cylinder pressure (450 hp) instead of 2400 psi (305 hp). There were some high stresses at the insert/head interface due to differences in thermal expansion coefficients. These could be lowered with some minor design changes.

Task 2: Exploration of the use of a Mg alloy to replace cast iron in diesel engine heads and blocks.

The table below shows the advantage of weight saving if Ti, Al, or Mg is used to replace cast iron in a 1000 lb diesel engine.

Material	Wt. Saving, lb
Ti-6-4 head and block	147
Al head on a Ti block	175
Al head and block	233
Mg head and block	362

It can be seen that a weight saving of about 35%, 23% or 15% could be achieved by a simple substitution of either Mg or Al or Ti, respectively, for the cast iron in the head and the block.

1. Ricardo was contracted to provide by FEA the temperatures and stresses in the head and block of a Cummins ISB engine running at 305 hp. Previously it was shown that using the Mg alloy, WE 43 that the engine could be used successfully as a replacement for grey cast iron.
    a) The analyses shows that by using the aluminum casting alloy A354-T6 as a replacement for grey cast iron for the head and block, the engine could be run successfully.

<u>Task 3</u>: Determine if there are fatigue benefits by casting Al parts using the Sub-Liquidus Casting (SLC) process instead the permanent mold process.

1. The cast bars have been made by THT Presses and delivered to Metcut Technology for machining and testing. Some of the data has been determined at room temperature and at 150°C and at 250°C. There appears to be some improvement in fatigue life at very high cycles compared to permanent mold cast material. However, metallography has shown that the SLC castings are not as porosity-free as expected. Even so, there is some benefit to using this process.

Mechanical Behavior of Ceramic Materials for Heavy Duty Diesel Engines (Q1-FY05)

A. A. Wereszczak, H. Wang, and M. K. Ferber
Ceramic Science and Technology (CerSaT)
Oak Ridge National Laboratory

Objective/Scope

The application of more ceramic components in engines and transportation systems would be enabled if they could be confidently manufactured and machined faster (i.e., more cost-effectively) and if mechanisms that limit their mechanical performance were understood, predictable, and controlled. This project quantifies "quasi-plasticity/fracture thresholds" in ceramics (e.g., cubic oxides and non-oxides, nanoceramics and nanocermets, piezoelectric ceramics, micaceous ceramics, and traditional structural ceramics) and examines the competing mechanisms that dictate when and how quasi-plasticity or fracture dominates the other during controlled and instrumented static and dynamic indentation and scratch testings. The thorough understanding of the competition of fracture and quasi-plasticity in ceramics will enable improved and faster means of ceramic component manufacturing and surface engineering (e.g., ductile regime machining) and maximize mechanical performance when surface condition (e.g., bending) or when surface-located events (e.g., wear, impact) are service-life-limiters in engine and transportation system components.

Technical Highlights

A substantial amount of static and dynamic Vickers indentation was completed on SN101C, NBD200, TSN 03-NH, NC132, and Ceralloy 147-31N silicon nitrides. The radial cracks about the Vickers indents were used to determine fracture toughness (K_{Ic}). A great deal of uncertainty can be associated with the determination K_{Ic} using indentation, so the testing of NC132 (a NIST Standard Reference Material, SRM, for K_{Ic}) was initially conducted and the results were interpreted using over 10 different indentation fracture toughness models (see [1-2] for their survey). Among them, the Evans and Charles model [3] produced K_{Ic} values most closely matched to the SRM K_{Ic} value, so that model was used for indentation K_{Ic} determinations on all the silicon nitrides tested. K_{Ic}'s from indents whose radial crack to indent diagonal (c/a) ratio was greater than 2.5 were deemed as acceptable values.

Examples of comparisons of quasi-static and dynamic properties are shown for Ceradyne's Ceralloy 147-31N. Results for all the investigated silicon nitrides will be discussed in a journal manuscript. Vickers Hardness as a function of load for quasi-static and dynamic loadings is shown in Figs. 1-2, respectively. For this material, there was a suggestion that dynamic loading resulted in a slightly larger hardness; however, this was not the case for all the silicon nitrides evaluated. Indentation K_{Ic} as a function of load for quasi-static and dynamic loadings are shown in Figs. 3-4, respectively. There is a subtle suggestion that fracture toughness decreased slightly for dynamic loading. The competition of damage (quasi-yielding and fracture processes) is being interpreted several ways - one is through the use of the established model of Bradt, et al., [4]. The data is remarkably linear when the ratio of the indentation load to indent diagonal length (P/d) is plotted as a function of diagonal length, see Figs. 5-6. Discussions with Bradt's group will be initiated to examine the significance of this further.

To examine the effect of grain size on damage due to cracking and quasi-plastic yielding generated with instrumented indentation and scratch testing, three different mean-grain-sized (2-3, 15, and 25 μm) aluminas are undergoing investigation. The microstructures of each are shown in Fig. 7, and their Knoop hardnesses as a function of indentation load are shown in Fig. 8. The alumina has 99.9% purity, Mg as a sintering aid, and each average grain size has a relatively tight distribution about it. A primary reason why alumina was chosen as the model material to examine grain size effects was because of the ease associated with measuring residual stresses with it using optical fluorescence and the immediate availability of such an analytical tool within CerSaT. Residual stresses will be measured in, around, and under generated indents and scratches, and will likely prove to be valuable results when interpreting grain size effects on cracking and quasi-plasticity. Damage evolution is likely to be a function of grain size - quantification of their effects will enable engineering control of ceramic machining or allowable wear conditions to inhibit or avoid deleterious effects that may be more strongly linked to fracture or quasi-plastic processes or both.

The Hertzian indentation model is continuing to undergo refinements. It presently predicts the stress state in a material subjected to Hertzian (spherical) indentation, and independent parameters that may be considered in the model are: elastic properties and hardness (i.e., yielding) of the target or indenter material, indenter diameter, coefficient of friction, confinement pressure, and of course applied indenter load. The modified model will allow the study of how quasi-plastic response is affected by microcracking and vice versa, see Fig. 9.

Examinations of some of the diamond spherical indenters revealed that their surface roughness was perhaps too large. Consequently, indenters were sent back to their manufacturer (Gilmore Diamond Tool) for refinishing.

Status of FY 2005 Milestones

Establish dynamic indentation and instrumented scratch testing facilities. Satisfied during present reporting period.

Communications/Visits/Travel

A presentation entitled "Mechanical Characterization of Ceramic Deformation Processes," was given at the *Ductilization of Ceramics Workshop*, Santa Fe, NM, 16 November 2004.

Discussions about the laser-assisted machining of Si_3N_4 occurred and are ongoing with Prof. S. Lei of Kansas State University.

Discussions were initiated with ORNL's P. Blau regarding a collaboration involving the use of their group's Grindability Tester.

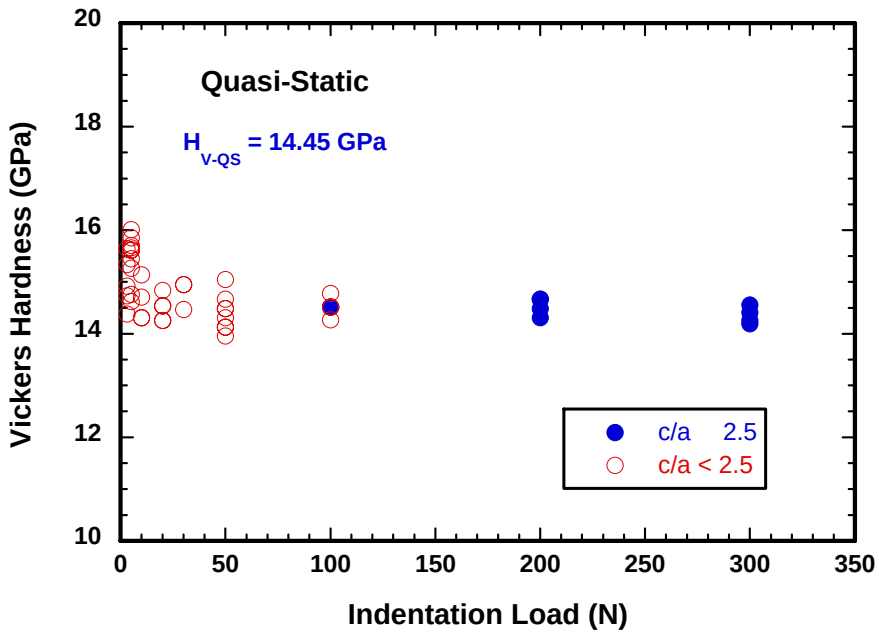

Figure 1. Vickers Hardness for Ceralloy 147-31N Si_3N_4 as a function of load for quasi-static loading. The H = 14.45 GPa is for indentation loads that generated a radial crack to indent diagonal (c/a) ratio ≥ than 2.5.

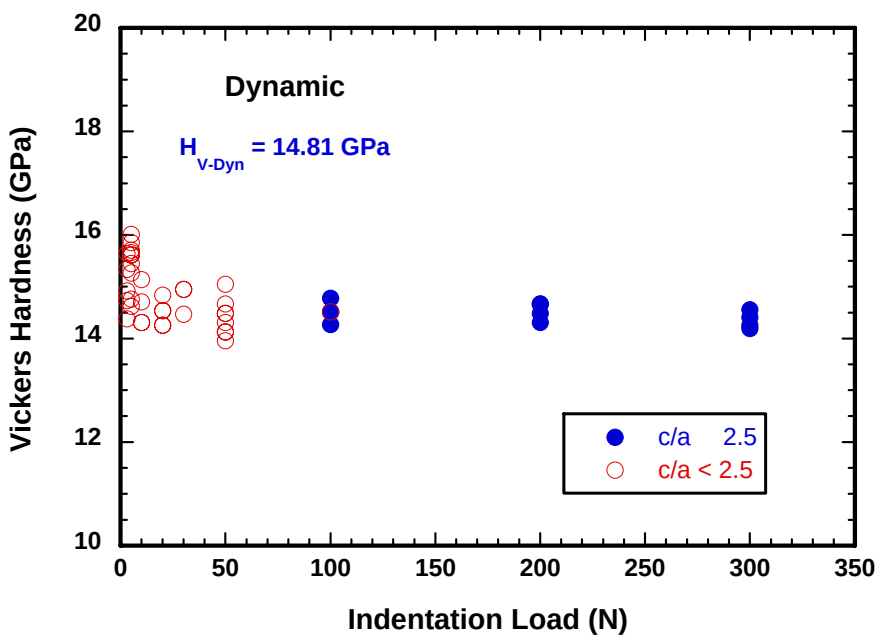

Figure 2. Vickers Hardness for Ceralloy 147-31N Si_3N_4 as a function of load for dynamic loading. The H = 14.81 GPa is for indentation loads that generated a radial crack to indent diagonal ratio ≥ than 2.5.

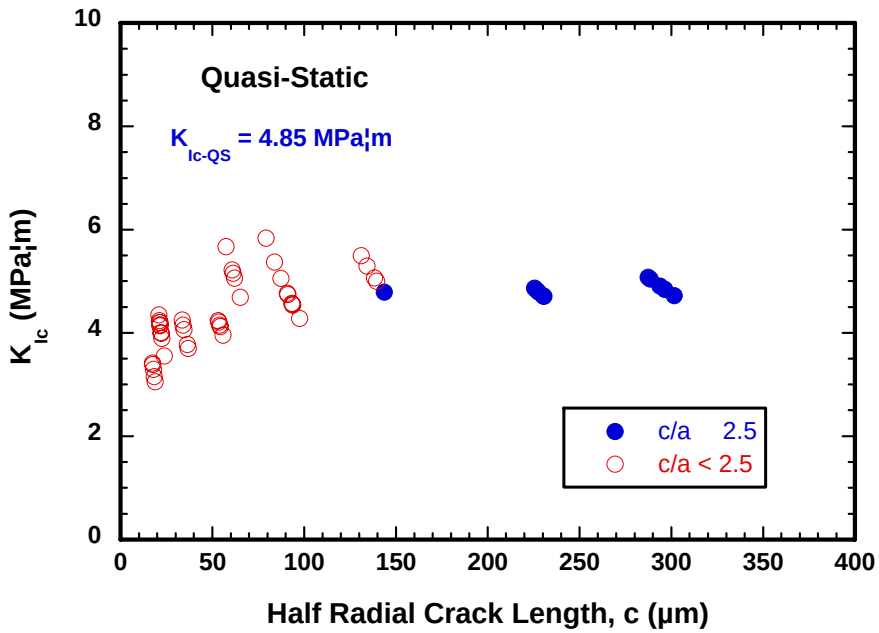

Figure 3. Indentation fracture toughness for Ceralloy 147-31N Si_3N_4 as a function of radial crack size for quasi-static loading. The $K_{Ic} = 4.85$ MPa√m is for indentation loads that generated a radial crack to indent diagonal ratio ≥ than 2.5.

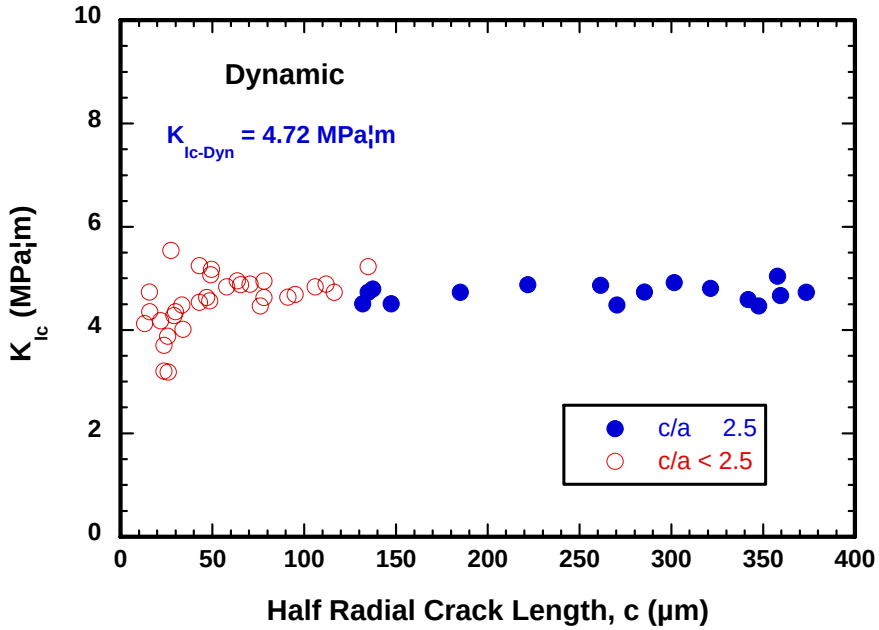

Figure 4. Indentation fracture toughness for Ceralloy 147-31N Si_3N_4 as a function of radial crack size for dynamic loading. The $K_{Ic} = 4.72$ MPa√m is for indentation loads that generated a radial crack to indent diagonal ratio ≥ than 2.5.

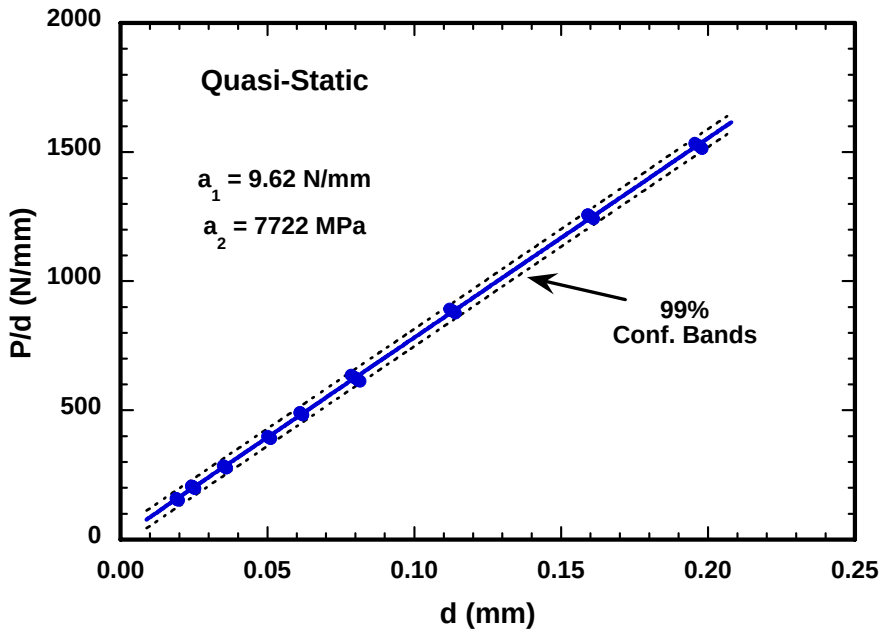

Figure 5. The ratio of indentation load to Vickers indent diagonal for Ceralloy 147-31N Si_3N_4 as a function of diagonal size for quasi-static loading.

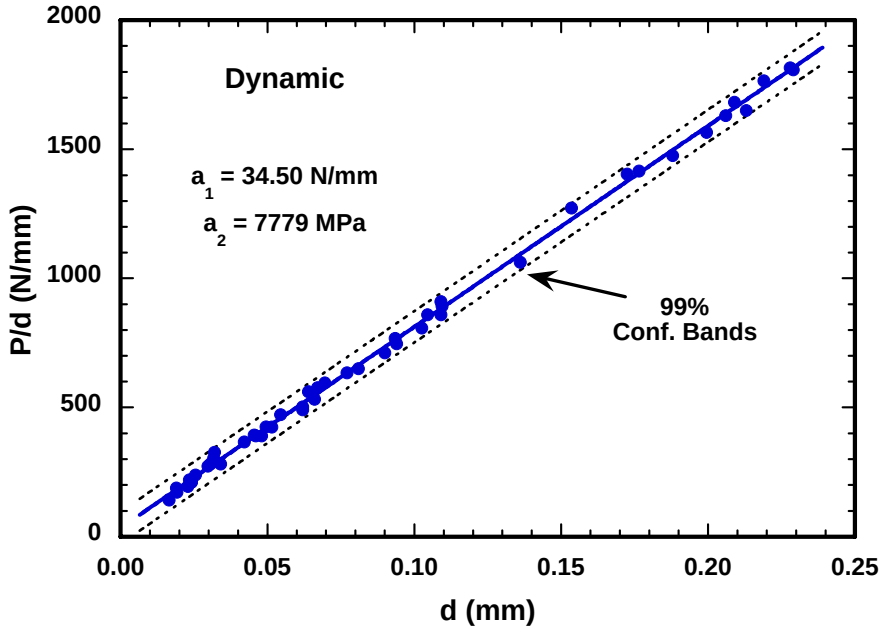

Figure 6. The ratio of indentation load to Vickers indent diagonal for Ceralloy 147-31N Si_3N_4 as a function of diagonal size for dynamic loading.

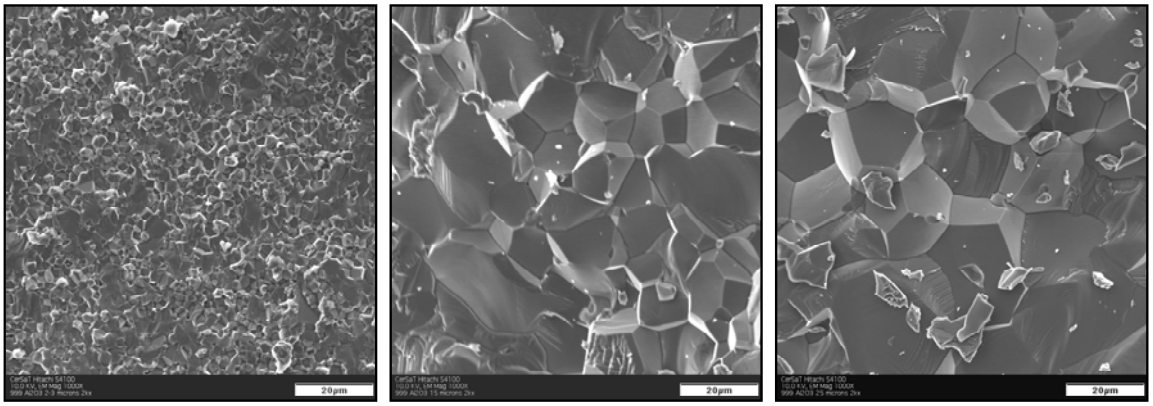

Figure 7. Microstructure on fracture surfaces of three different 99.9% aluminas. The means sizes are 2-3 (left), 15 (center), and 25 µm (right). The indentation and study its damage in these materials will enable the study of their dependencies on grain size.

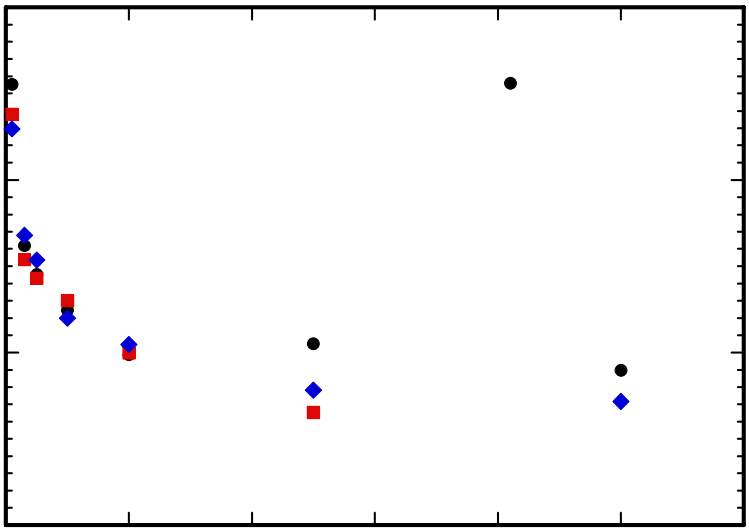

Figure 8. Knoop hardness as a function of indentation load and average grain size for the 99.9% alumina.

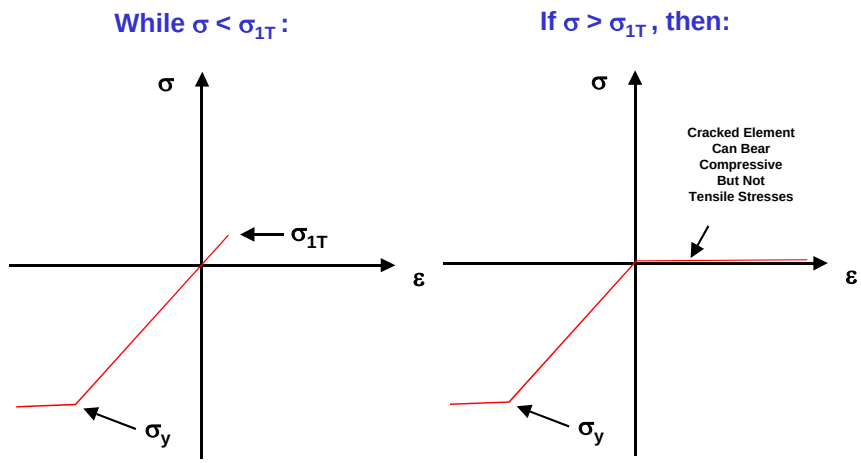

Figure 9. The Hertzian indentation model is being altered to allow for the study of the effect of cumulative damage on indentation response. It will depict the fact that monolithic ceramics are much stronger in compression than in tension (left) and that they can yield if compressive stresses are high enough. If tensile strength is exceeded (right), it will permit subsequent compressive but not tensile loadings.

Publications

H. Wang and A. A. Wereszczak, "Mechanical Responses of Silicon Nitride Under Dynamic Indentation, to be published in *Ceramic Science and Engineering Science Proceedings*, 2005.

G. Subhash, M. A. Marszalek, A. A. Wereszczak, M. J. Lance, "Scratch Resistance and Residual Stresses in Longitudinally and Transversely Ground Silicon Nitride," to be published in *Ceramic Science and Engineering Science Proceedings*, 2005.

A. A. Wereszczak and T. P. Kirkland, "Exclusivity of Strength-Limiting Intrinsic and Hybrid Flaws," to be published in *Ceramic Science and Engineering Science Proceedings*, 2005.

References

[1] C. B. Ponton and R. D. Rawlings, "Vickers Indentation Fracture Toughness Test, Part 1, Review of Literature and Formulation of Standardised Indentation Toughness Equations," *Materials Science and Technology*, **5** 865-72 (1989).

[2] C. B. Ponton and R. D. Rawlings, "Vickers Indentation Fracture Toughness Test, Part 2, Application and Critical Evaluation of Standardised Indentation Toughness Equations," *Materials Science and Technology*, **5** 961-76 (1989).

[3] A. G. Evans and E. A. Charles, "Fracture Toughness Determinations by Indentation", Journal of the American Ceramic Society, **59** 371-72 (1976).

[4] M. E. Stevenson, M. Kaji, and R. C. Bradt, "Microhardness Anisotropy and the Indentation Size Effect on the Basal Plane of Single Crystal Hematite," *Journal of the European Ceramic Society*, **22** 1137-48 (2002).

Powder Processing of Nanostructured Alloys Produced by Machining

S. Chandrasekar, K. P. Trumble, and W. D. Compton
Purdue University

Objective/Scope

This project builds on the recent discovery of a low-cost means of producing nanostructured materials in essentially any alloy via normal machining. Comminution of the nanostructured chips will enable large scale production of nanocrystalline particulate, which can be converted into nanostructured bulk forms using powder processing methods. Alternatively, the chips and particulates may be used as continuous or discontinuous reinforcements in metal or polymer matrices to create advanced composite bulk forms. Three routes for consolidation and densification of the nanostructured particulate to produce monolithic and composite materials are being pursued:

(1) Shear-based deformation processing, including powder extrusion and powder rolling
(2) Rapid infiltration processing using low-melting metal alloys
(3) Polymer die-press bonding

These routes are all geared toward densification and bonding of the particulate while minimizing thermal coarsening. For the powder extrusion, nanostructured Al-6061-T6 chips were converted into particulate using attrition milling. The resulting particulate was mixed with varying weight percentages of commercially available, gas-atomized Al powder; this mixture was powder extruded through steel dies at extrusion ratios of 10-60. The extruded samples were prepared in the form of cylinders up to 10 mm in diameter and 5-25 mm in length.

Infiltration processing has focused on pressure infiltration of M2 tool steel chips with hypoeutectic Al-Si casting alloy Al-356. The liquidus temperature of this alloy is in the range of secondary hardening temperatures of the high-speed tool steel. A preliminary study is in progress to compare these results with Al-356 infiltrated AISI 1018 plain-carbon steel chips, in which there is a larger relative increase in hardness upon machining compared to the M2 steel. Complimentary studies of the kinetics of the diffusion reaction between the liquid Al alloy matrix and iron and steel of different degrees of cold-work have also been completed.

The polymer bonding is a new approach in which a thermosetting polymer resin is used, together with high-pressure compression molding in a steel die to yield a structure consisting of low volume fractions of polymer bonding the nanostructured metal particles. The focus so far has been on Al-6061-T6 chip powders bonded with different epoxies. This approach is based on the observation that the cure conditions of the resin are well below the know time-temperature conditions for coarsening (and loss of hardness) of the nanostructures in the chip particles. Application for light weight, wear-resistant components is envisioned.

Technical Highlights

Nanostructured Pure Titanium imaged by TEM

Figure 1 shows a TEM micrograph and selected area diffraction pattern of nanostructured Ti formed in machining chips. The starting grain size of the commercially pure Ti was ~ 50 μm and TEM revealed a grain size range of 50 to 200 nm in the chip specimens. Correspondingly, Vickers hardness increased from 144 ± 5 to 230 ± 9 kg/mm^2, consistent with the machining response of a wide range of other pure metals and alloys.

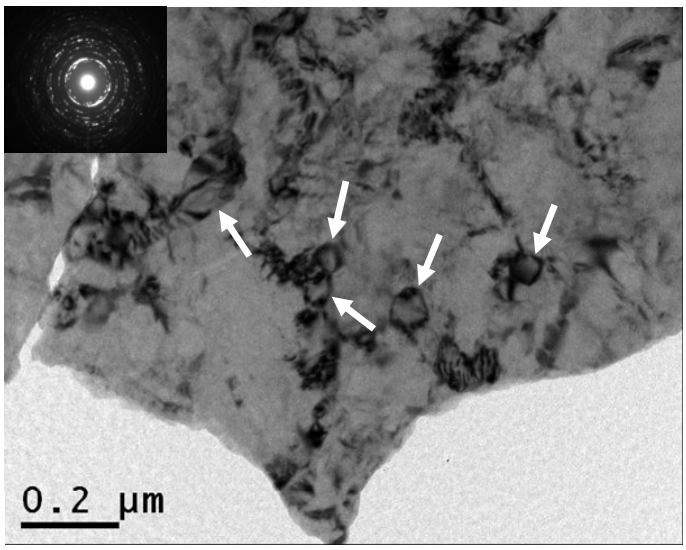

Figure 1. Bright-field TEM and selected area diffraction pattern of pure Ti chip produced at shear strain of 2.04. Arrows indicate individual grains smaller than 100 nm.

Densification of Al-6061-T6 chip particulate achieved by extrusion at room temperature

Extrusion of nanostructured Al6061-T6 chip particulate results in poor densification and bonding. However, by blending the chip particulate with pure Al powder, near complete densification is possible. The effect of chip powder particle size relative to the pure aluminum (Ampal, 99.9%, gas-atomized, ~60 μm) and extrusion ratio are under investigation. Figure 2 show the extrudate and corresponding microstructure for a ~180 μm nanochip particulate blended 50-50 with pure aluminum and extruded at room temperature with an extrusion ratio of 42. Immersion density measurements indicated a relative density of 98.7%, consistent with the small amount of porosity observed in optical microscopy. The chip particles are clearly distinguished in the micrographs and appear well-bonding with the continuous pure Al matrix. Tensile testing in progress should provide a clear indication of the degree of particle bonding. Scaling up to billets large enough to take advantage of the ORNL extrusion facilities should begin in the next quarter, as larger supplies of particulate become available.

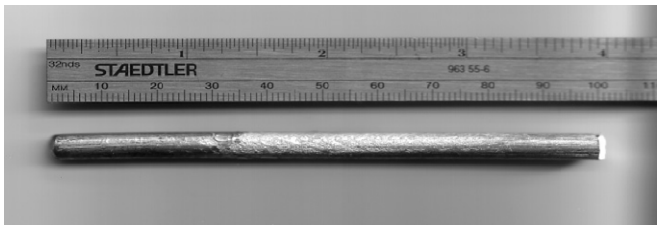

(a)

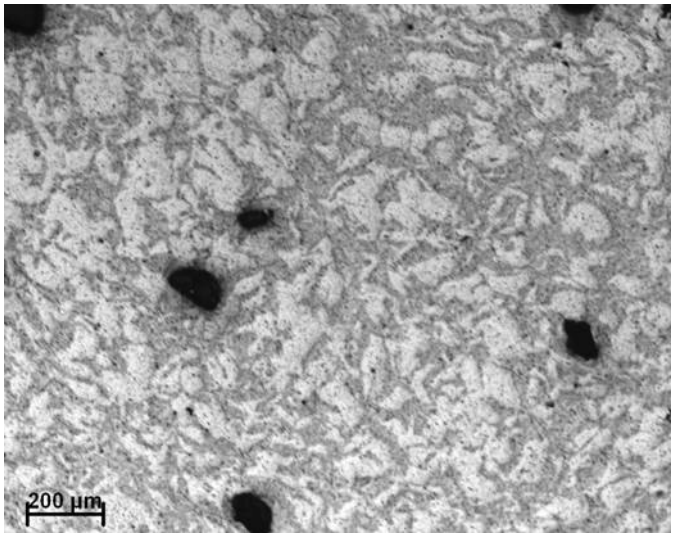

(b)

Figure 2. (a) Macrograph showing Al-6061-T6 nanochip/pure aluminum (1:1 by volume) extrudate; extrusion ratio = 42. (b) Optical micrograph of corresponding microstructure in cross-section showing small amount of residual porosity on the order of the nanochip particle size but otherwise well-bonded structure.

Al alloy-infiltrated steels produced without significant interphase reaction

Figure 3 shows the microstructure of an Al-356/M2 steel nanochip composite produced by melt infiltration. Loose-packed chips were infiltrated in simple graphite dies, which allowed for only about 1 atm applied pressure. A small amount of porosity is apparent, which should be easily reduced by using higher pressure infiltration as, for example, in die casting. Preliminary hardness measurements indicate a small but statistically significant hardness decrease, but no significant amounts of interphase reaction between the aluminum alloy and steel have been resolved. Similar results have been obtained recently using nanostructured AISI 1018 steel chips. Sliding wear tests on both of these composites are in progress.

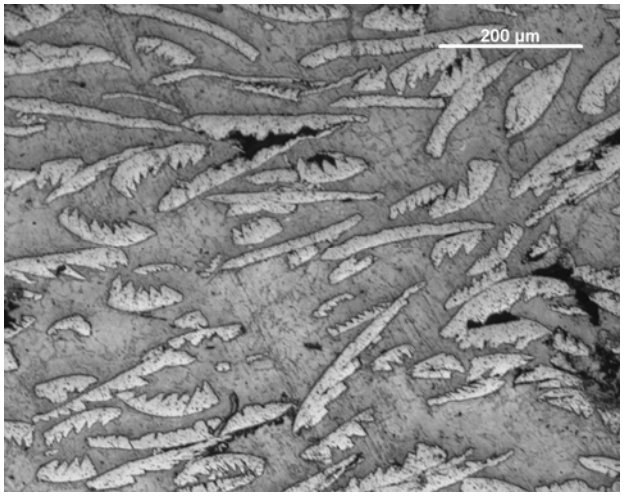

Figure 3. Al-Si alloy 356/M2 high speed steel chip composite. Some porosity is visible between chip clusters, indicative of wetting failure. Otherwise the interfaces appear well formed, with little or no interphase (intermetallic) reaction products.

Polymer-bonded chip particulate composite demonstrated

We have also been successful, recently, at producing bulk Al-6061-T6 samples from nanostructured chip particulate via an infiltration/pressing approach using a small amount (<10%) of epoxy as binder. Figure 4 shows a typical example. Small amounts of porosity persist, especially where larger particles were not packed uniformly, but most particle boundaries show a thin bond layer of epoxy. Epoxy and porosity volumes as low as 6% have been achieved so far and preliminary nanohardness measurements show little or no loss of hardening imparted in producing the chips, consistent with separate measurements of coarsening-softening kinetics in this alloy.

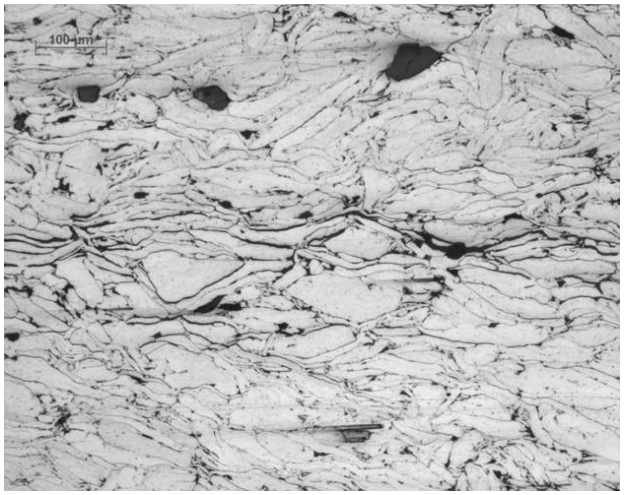

Figure 4. Optical micrograph showing epoxy-bonded Al-6061-T6 chip particulate (15-100 µm) pressed at 1000 MPa and cured at 100°C.

Problems Encountered
None

Status of Milestones
"Evaluate a range of consolidation and densification routes that enable bulk monolithic and composite materials to be produced from nanostructured machining chip particulate without significant coarsening." On schedule.

Publications
1. S. Swaminathan, M. Ravi Shankar, S. Lee, J. Hwang, B. Rao, S. Chandrasekar, W. D. Compton, K. P. Trumble and A. H. King, “Large Strain Deformation and Ultra-fine Grained Materials by Machining." submitted for Proceedings TMS symposium in honor of T. Langdon.

Deformation Processes for the Next Generation Ceramics

Paul F. Becher
Oak Ridge National Laboratory

Objective/Scope

This project seeks to determine how to exploit the deformation response of ceramics to enhance mechanical properties and develop novel shape forming with particular emphasis on the impact of nano-scale microstructures. This project involves two major thrusts. The first is a collaborative effort with researchers in the Synthesis of Nanocrystalline Ceramics task at Pennsylvania State University in the processing and sintering of nanocrystalline ceramics. The goal being to develop the technology to form "green" (unfired) bodies of nanocrystalline particles with densities well in excess of 50% of the theoretical density to allow one to devise pressureless sintering profiles to produce dense monolithic bodies with grain sizes < 100 nm [1]. This is aimed at finding approaches to produce sizeable monolithic bodies for subsequent evaluation. The second thrust focuses on the mechanical and wear behavior of nanocrystalline ceramics and the influence of external parameters (e.g., stressing rate, temperature, environment (e.g., air, vacuum), and electric fields (in collaboration with researchers at North Carolina State University) on the plastic deformation behavior.

Technical Highlight

Synthesis, Evolution and Stability of Nanostructures in Bulk Materials

The challenges in particle processing to form bulk, dense nanometer grain sized materials include the dispersion of the nanosize particles and control of gas evolution from the very high surface area compacts during sintering. Typically, nanometer size particulates suffer from a high degree of agglomeration, which results in poor particle packing (green densities < 40% of theoretical), which inhibits sintering and promotes undesirable grain growth. Two routes to obtaining well-dispersed powders include comminution and colloidal processing [2,3]. By optimizing colloidal processing approaches, one should be able to produce "green bodies with densities in excess of 60% of theoretical by control of interparticle forces through appropriate chemical additives to suspensions of nanoparticulates combined with filter pressing or pressure casting of the high solids content slurries. By controlling the packing of nanoparticulates one should be able to control the porosity to achieve the narrow size distribution necessary, which then will enhance densification.

Densification of nanocrystalline ceramics has typically involved the use of applied pressure to achieve dense sub-100 nm grain sized samples [4]. In those few cases where pressureless sintering has been employed successfully, long hold times at the sintering temperatures were required to achieve densities ≥ 95% of theoretical, which allows undesired grain growth to proceed [5]. Heating to a temperature sufficient to achieve densities of ≥ 75% of theoretical followed by rapidly lowering the temperature to a level to obtain sufficient boundary diffusion to remove pores trapped on boundaries while minimizing grain growth have been only partially successful as long hold times at the lower temperature were still required [5]. Here we seek to optimize the processing of the "green" bodies and utilize modified sintering cycles to achieve dense sub-100 nm grain size oxides.

Advanced colloidal processing in the Synthesis of Nanocrystalline Ceramics task have provided monolithic "green" bodies of both yttria-doped and undoped zirconias with densities from 55 to 68% of theoretical and an average particulate size of ~15 nm. Novel sintering cycles now allow one to produce dense monolithic zirconias with grain sizes well below 100 nm. As noted, sintering in vacuum promotes densification at lower temperatures as compare to sintering in air. At this point, one presumes this is due to lower of the capillary pressure within pores and faster removal of any residual organics or moisture used in the colloidal processing.

At the same time, it is obvious that the addition of yttria inhibits the densification of nanocrystalline zirconia. Recent studies indicate that space charge effects due to yttrium segregation may inhibit Zr^{+4} lattice diffusion [6]. While grain boundary diffusion is a critical factor in the removal of pores during the densification of nano-particulate bodies, lattice diffusion might impose some limitation on limit be a rapid limiting parameter in sintering. In addition, deformation rates by diffusional processes may exhibit less than the $(\text{grain size})^{-2}$ predicted from Nabarro-Herring creep due to space charge effects [6,7]. However, space charge effects can be modified by solute and environmental parameters, which have important implications for enhancing the mechanical behavior in nanocrystalline oxides.

References

1. M. J. Mayo, "Processing of Nanocrystalline Ceramics from Ultrafine Powders," Int'l Mater. Rev. 41(3) 85-115 (1996).
2. J. H. Adair et al., "Dynamic Control and Enhanced Chemical Milling of Ceramics to Submicron Particle Sizes," U.S. Patent 6,415,966 B1, July 9, 2002.
3. T. Tsukada, S. Venigalla, A. A. Morrone, and J. H. Adair, "Low-Temperature Hydrothermal Synthesis of Yttrium-Doped Zirconia Powders," J. Am. Ceram. Soc. 82(5) 1169-74 (1999). J. H. Adair et al., *Material Science and Engineering Reports*, *R23*(4-5) 139 (1998). R. A. Kimmel and J. H. Adair, "Aqueous Degradation and Chemical Passivation of Yttria-Tetragonally-Stabilized Zirconia at 25°C," J. Am. Ceram. Soc. 85(6) 1403-08 (2002).
4. R. Chaim and M. Hefetz, "Fabrication of Dense Nanocrystalline ZrO_2-3 wt. % Y_2O_3 by Hot-Isostatic Pressing," J. Mater. Res., 13(7) 1875-80 (1998).
5. I.-W. Chen and X. –H. Wang, "Sintering Dense Nanocrystalline Ceramics Without Final-Stage Grain Growth," Nature 404: 168-71 (2000).
6. D. Gomez-Garcia, C. Lorenzo-Martin, A. Munoz-Bernabe, and A. Dominguez-Rodriguez, "Model of High-Temperature Plastic Deformation of Nanocrystalline Materials: Application to Yttria Tetragonal Zirconia," Phys. Rev. B67 (14): Art. No. 144101-1 to –8 (2003).
7. C. H. Hsueh and P. F. Becher, "Effects of Dopant Segregation on Lattice-Diffusional Creep of Nanocrystalline Ceramics," *Phys. Rev. B*, accepted for publication.

Status of Milestones

New project

Communications/Visits/Travel

None

Publications

C. H. Hsueh and P. F. Becher, "Effects of Dopant Segregation on Lattice-Diffusional Creep of Nanocrystalline Ceramics," *Phys. Rev. B*, accepted for publication.*

---

*Study was jointly sponsored with U. S. Department of Energy, Office of Basic Energy Sciences, Division of Materials Science and Engineering.

Synthesis of Nanocrystalline Ceramics

James H. Adair
Pennsylvania State University

Objective

Advanced particle processing will be used to produce dense, bulk nanocrystalline oxide ceramics. Two routes to obtaining well-dispersed powders (i.e., comminution and colloidal processing) will be emphasized. The large surface areas of such powders lead to large quantities of adsorbates, which must be removed both to enhance particle packing and subsequent sintering. Both reactive atmosphere and microwave thermolysis have merit and will be evaluated to eliminate adsorbates at low temperatures. This project will scale-up the processes to be able to produce dense YSZ ceramics with grain sizes less than 100 nm having sample dimensions ≥ 25mm in diameter by ≥3 mm in thickness to be delivered to ORNL for further testing. Additional effort will focus on fabrication of said samples with grain sizes < 50 nm for testing by ORNL staff.

Background

Particle processing has the potential to produce dense, bulk nanocrystalline materials with a variety of chemical compositions and architectures including composite materials. Outstanding challenges in particle processing to form bulk, dense nanograin sized materials include the dispersion of the nanosize particles and control of gas evolution from the very high surface area compacts during sintering. Typically, nanometer size particulates suffer from a high degree of agglomeration, which results in poor particle packing (green densities < 40% of theoretical) and inhibits sintering and promotes undesirable grain growth. Two routes to obtaining well-dispersed powders include comminution and colloidal processing. Recent advances in colloidal processing have obtained high green densities (>50% of theoretical) with 8 nm YSZ particulates, which preliminary sintering efforts resulted in a translucent, fully dense 45 nm grain sized ceramic. Finally, gas evolution during sintering can occur due to the very high surface areas of nanoparticulate green bodies and disrupt sintering processes. While the thermodynamics and kinetics in the gas phase evolution reactions are reasonably well established, the fundamental science and engineering aspects must be addressed for each nanoparticulate system. Recent considerations indicate that innovative gas phase treatments (e.g., injection of reactive gases during the sintering cycle) can be used to overcome the undesirable effects of evolution gases from the nanoparticulate bodies during sintering.

Status

The focus of research during the past quarter has been the preparation and drying of filter-pressed zirconia pellets. It has been proposed that water removal may be accomplished by pushing a non-aqueous solvent through the filter-pressed body immediately after pressing. Several solvents have been suggested: ethanol, methylethyl ketone (MEK), isopropanol, and acetone. Experiments in which any of these solvents were forced through the filter-pressed body have all resulted in crack formation within the body. It has also been suggested that a solvent exchange may be achieved by a gradual change in environment, i.e. submersing the wet green body in aqueous filtrate and slowly adding increasing amounts of solvent. However, as soon as the green body was submersed, it dispersed back into suspension. It was concluded that the best method for removing water from these green bodies was by controlled humidity drying.

Using a humidity-control oven, filter-pressed pellets were dried from a relative humidity of 100% to 30% in about 4 hours. However, due to differential shrinkage caused by adhesion to filter membranes or physical handling damage, cracking has taken place in all samples dried so far. The pieces of dried pellets were cold-isostatically pressed (CIP) to further compact the bodies and increase green strength.

After filter-pressing, wet pellets usually have a theoretical density of about 45-50% (by dimensional measurements). After humidity-controlled drying, theoretical density increases to about 55-60% (as measured by the Archimedes method). Green density is increased again after CIPing to as high as 68% of theoretical (as measured by the Archimedes method)

Currently, efforts are focusing on the production of dried, whole samples of pure and yttria-doped zirconia as well as their densification behavior under transient sintering conditions. A comparison will also be made between the sintering of filter-pressed green bodies versus that of dry-pressed bodies.

Plans for Next Quarter

The emphasis over the next quarter will be to prepare pellets for sintering trials and delivery to ORNL personnel to continue evaluations of microstructural and mechanical properties. These activities involve organic removal and pellet drying in addition to sintering trials.

Patents

None to report.

Publications/Presentations

None to report.

Milestone Status Table

ID Number	Task / Milestone Description	Planned Completion	Actual Completion	Comments
1	Particle Process for Nanoscale Zirconia	1/31/05	6/30/04	
1.1.1	Particle Preparation	3/30/04	3/30/04	
1.1.2	Particle Preparation Scale-up	3/30/04	6/30/04	
1.1.3	Pressure Casting	4/30/04	9/30/04	
1.1.4	Organic Removal	5/30/04	9/30/04	
1.2.1	Drying	8/15/04	9/30/04	
1.2.2	Sintering	10/15/05	In progress	
1.2.3	Characterization	12/15/05	In progress	
1.2.4	Shipment of Parts to ORNL for Evaluation	10/15/05	In progress	
1.3.5	Analyze Data	12/31/05	In progress	
1.4	Final Report	1/31/06	In progress	

Development of Titanium Alloys for Heavy-Duty Diesel Engines

Nan Yang, Jeremy Trethewey, Jesus Chapa-Cabrera, John A. Grassi
Caterpillar Inc.

Introduction

The present cost of producing titanium has significantly decreased, and the future forecast is for the decreasing trend to continue, making titanium alloys an attractive alternative to other strong, lightweight materials. Turbochargers on diesel engines play an integral role in meeting emission regulations and controlling fuel economy. Caterpillar Inc. has introduced the use of two turbocharger systems on some on-highway diesel engines in order to meet current and future emission regulations. The presence of two turbocharger systems challenges the already limited under the hood space for on-highway truck applications and so the development of an alternative turbocharger system that is smaller and lightweight is of great interest.

Project Objectives

The purpose of this program is to develop one or more heavy-duty diesel engine components using titanium alloys. The chosen engine components must demonstrate an improvement in fuel efficiency while reducing emissions. Caterpillar has selected the turbocharger wheel as an engine component to be fabricated from titanium aluminide (TiAl). In addition, Caterpillar has patented a new compact design for the turbocharger known as the HEAT™ (High Efficiency Advanced Turbocharger) that will utilize the TiAl turbo wheel. The HEAT™ consists of two compressor wheels and one turbine wheel attached to the same driveshaft. One compressor wheel is made from an aluminum alloy while the second compressor wheel is made of Ti-6V-4Al.

In order for the HEAT™ to meet the performance specifications of two turbocharger systems, a high strength, lightweight turbo wheel must be developed, which is the primary objective of this project. Thus, lightweight titanium materials (e.g. TiAl) are among the critical technologies for the successful development of this new turbocharger design that will meet transient emission regulations while improving the engine's fuel efficiency and responsiveness in various applications.

Approach

An interdisciplinary team has been organized at Caterpillar to develop the TiAl turbowheel. Staff members from the Advanced Materials Technology (AMT) division will lead and manage the project development efforts. Experts from the Large Engine Center (LEC) Air Systems division will work with Engine Research to design and bench test the turbo wheel. Manufacturing and Process engineers from the Mossville Engine Center (MEC) will work with machining experts at the Advanced Production Technologies (APT) division to develop a cost competitive manufacturing implementation plan.

Quarter Summary

Supplier Readiness

The Advanced Materials Technology (AMT) team meets frequently with suppliers to ensure the manufacturing readiness for providing the TiAl turbine wheels with required quality. Large size TiAl turbine wheels have been procured from Supplier A. A second order has been placed with Supplier A to include full size wheels and two different sizes specimen bars. These samples will be cut into specimens for tensile, creep, Thermo-mechanical Fatigue (TMF), Foreign Object Damage (FOD), and friction welding tests, as well as physical properties measurements. A batch of small sized TiAl turbine wheels and test bars from Supplier B has been received and larger size turbine wheels have been requested.

Materials Characterization

Testing houses for mechanical testing and FOD tests have been identified along with corresponding testing matrices. Two batches of the samples from Supplier B have already been provided to a subcontractor for mechanical testing, and the results are expected in the next quarter. Upon receiving wheel samples from the suppliers, FOD test will begin in the next quarter.

Friction Welding

As previously reported, the cracking that occurred during the later stage of the friction welding process is one of the main technical challenges in the project. This problem will be resolved before a parametric study can be conducted to maximize the welding strength through optimized friction welding parameters and part geometry. Previous finite element analysis of the friction welding process as well as non-destructive evaluation and fractographic examination have shown that the cracking was caused by high thermal stresses. Therefore, a design for minimizing thermal stress must be adopted in the friction welding process. Process control is being incorporated in the friction welding experiment to minimize the thermal stress.

The correlation between temperature gradient and thermal stress in the friction welding process is being studied using simulation in order to select the proper temperature gradient limits. Once the proper temperature gradient limits corresponding to tolerable thermal stresses are selected, further parametric study will be performed during the next quarter.

Mechanical Joining

A temporary mechanical joining technique has been developed to attach the turbine wheel to a shaft. This temporary joining must be deployed for the gas stand test in the next quarter.

Future Plans

Upon selecting the temperature gradient limit, a parametric finite element analysis will be conducted. The results of this analysis will be used for designing the friction welding experiment. The experiment will then be conducted with the objective of completing the development of a robust joint. The FOD test will start in the next quarter. Mechanical testing and physical measurements are expected to be completed in the next reporting period.

Rolling Contact Fatigue

A. A. Wereszczak and T. P. Kirkland
Ceramic Science and Technology (CerSAT)
Oak Ridge National Laboratory

Objective/Scope

The understanding and control of contact damage behavior of ceramics under rolling and sliding conditions are enablers to more widespread utilization of ceramics as cam followers, valves, valve seats, and other important transportation-related components. International interest exists to understand the fundamentals of rolling contact fatigue (RCF) of ceramics because greater control (or minimization) of RCF will result in longer life of such components. Rolling contact fatigue is internationally studied through a variety of test methods and analytical approaches; interest exists in the present project to link their measured performances. Toward that, RCF studies (primarily of Si_3N_4) involving both international and domestic interactions are being pursued as Annex III of the International Energy Agency (IEA) agreement.

Technical Highlights

Hardware modifications to the RCF tester were performed to enable greater versatility in the testing. A single lubricant reservoir was native to the tester and only permitted the use of a sole lubricant for all four test stations. Four one-quart reservoirs were purchased and mounted on top of the RCF tester and the plumbing lines rerouted to connect the reservoirs to each station. This modification will now enable the concurrent testing with different lubricants.

In preparation for collaborative and comparative RCF testing of Si_3N_4, a machining request to machine balls with different grinding conditions was submitted to PremaTech Chand. Spheres will be machined from cylindrical bar stock. The grinding conditions are the same as those used to machine RCF test rods, and RBS, half-RBS, and ASTM C1161B test coupons, and are summarized in Table I. Four sets are listed in Table I; three have a 12.7 mm diameter and the fourth has a 13.2 mm diameter. The larger diameter will be used by Bournemouth University to reduced to a 12.7 mm diameter using an internally developed lapping procedure that will essentially yield a fourth finish condition. These spheres will be used in both three-ball-on-ball and three-ball-on-rod RCF tests.

Fractography of the Ceralloy 147-31N Si_3N_4 RCF, rotary bend strength (RBS), half-RBS, and ASTM C1161B test specimens commenced during the present reporting. Perhaps more important than the identification of the strength-limiting flaws in these specimens will be the determination of the depth of the subsurface damage resulting from their machining in like fashion to Quinn, *et al.* [1]. That quantified subsurface damage will be linked to RCF performance.

Elastic property measurements were made on spheres using a developed method [2] that combines resonant ultrasound spectroscopy (RUS) and finite element (FEA) modal analysis. The methods generated values to four significant digits and are listed in Table II for three commercially available bearing grade Si_3N_4 spheres, and will be performed on Ceralloy 147-

31N. The elastic properties are needed to accurately determine Hertzian stresses in the RCF testing.

W. Wang started their graduate studies at Bournemouth University during the present reporting period and formal plans have been made for his first research visit to begin at ORNL in early May and go through November 2005. W. Wang will perform RCF research at Bournemouth using three-ball-on-ball testing and assist this project's PI on three-ball-on-rod testing at ORNL. The evaluation of the role of subsurface damage on RCF performance is a key element to the study and the linkage of results generated from the two techniques will be an outcome as well.

A report entitled “Rolling Contact Fatigue of Ceramics” by Y. Wang, M. Hadfield, W. Wang, and A. A. Wereszczak was completed and is currently in ORNL internal review. The report will be published as a DOE/ORNL Technical Memorandum.

Table I. Grinding Conditions for Silicon Nitride Spheres.

Diameter & Finish	Step	Wheel	Removal	Removal per pass
12.7 mm / 0.500"	1 (roughing)	accepted practice		0.001”
	2 (induce damage)	100 grit	0.004”	0.001”
Coarse	3 (finishing)	600 grit	0.0005”	0.0001”
13.2 mm / 0.520"	1 (roughing)	accepted practice		0.001”
	2 (induce damage)	100 grit	0.004”	0.001”
Coarse	3 (finishing)	600 grit	0.0005”	0.0001”
12.7 mm / 0.500"	1 (roughing)	accepted practice		0.001”
	2 (induce damage)	180 grit	0.004”	0.001”
Fine	3 (finishing)	600 grit	0.0005”	0.0001”
12.7 mm / 0.500" RCF-Conventional	“Accepted” practice for RCF test bar finishing			

Table II. Measured Properties of Bearing Grade Si_3N_4 Spheres.

Grade	Density (g/cc)	Elastic Modulus (GPa)	Poisson's Ratio
NBD 200	3.211	321.5	0.2710
SN 101C	3.161	306.9	0.2705
TSN 03-NH	3.249	308.7	0.2782

Status of FY 2005 Milestones

Characterize the effect of sub-surface machining damage on Si_3N_4 rolling contact fatigue performance and submit paper to the open literature on the results and interpretations. [09/05] *On schedule.*

Communications/Visits/Travel

- Hitesh Trivedi of UES/USAFRL (Dayton, OH) was visited on 20 October to discuss RCF issues and potential interactions.
- Discussions with Vimal Pujari (Saint-Gobain Advanced Ceramics, Northboro, MA) occurred regarding the RCF testing and characterization of their bearing grade Si_3N_4's.
- Several communications occurred with W. Mandler of Enceratec regarding the testing of Toshiba TSN 03-NH Si_3N_4 spheres.

Publications

Y. Wang, M. Hadfield, W. Wang, and A. A. Wereszczak, "Rolling Contact Fatigue of Ceramics," in internal review, to be published as a DOE/ORNL Technical Memorandum.

References

[1] G. D. Quinn, L. K. Ives, and S. Jahanmar, "On the Fractographic Analysis of Machining Cracks in Ground Ceramics: A Case Study on Silicon Nitride," NIST Special Publication 996, National Institute of Standards and Technology, US Department of Commerce, May 2003.

[2] A. A. Wereszczak, "Elastic Property Determination of WC Spheres and Estimation of Compressive Loads and Impact Velocities That Initiate Their Yielding and Cracking," in press, *Ceramic Engineering and Science Proceedings* (2005).

Implementing Agreement For A Programme Of Research And Development On Advanced Materials For Transportation Applications

M. K. Ferber
Oak Ridge National Laboratory

Objective/Scope

The current mission of the IA-AMT is to investigate promising new technologies for evaluating and ultimately improving the performance of materials for transportation systems. The primary motivation for this activity is the fact that new material technologies are required to increase efficiency and reduce harmful emissions in these systems. Examples of these technologies include (1) light weighting to improve fuel efficiency, (2) surface engineering to improve the resistance to wear and contact damage, (3) development of durable coating systems for thermal, wear, and environmental management, and (4) development of revolutionary materials (structural ceramics and ceramic matrix composites) for operation at much higher temperatures and pressures. As discussed below, the research activities within the IA-AMT focus specifically on (1) the identification of promising new technologies for improving materials performance and (2) the development of specialized characterization techniques for validating the applicability of this technology to improve material properties while maintaining acceptable life-cycle costs.

Technical Highlights

This reporting period the laser spallation test for the measurement of coating adherence [1, 2] was evaluated. In this test, the tensile forces required for coating debonding are generated by a pulsed laser focused on the back of the substrate. This initial impingement generates a compressive wave which on reflection becomes tensile. Specific tests utilized commercial hardware for Laser Shock Peening (LSP), which is a relatively new surface treatment for generating compressive stress fields in the near surface regions of metallic materials. When applied to selected regions of engineering component such as gas turbine airfoils, these stress fields can greatly improve resistance to fatigue and increase tolerance to foreign object damage. The depth of the compressive residual stresses are typically much greater than those induced by conventional shot peening. As illustrated in Figure 1, the technique involves the production of mechanical shock waves by using a laser to generate a plasma over a small spot on the surface. This plasma is formed by the vaporization and subsequent ionization of a sacrificial material such as black tape or paint, which is first applied to the region to be treated. An over-layer of water, which is transparent to laser radiation, is used to confine the expansion plasma such that a shock wave is driven into the component. The surface and near surface regions are subject to plastic deformation if the pressure of the shock wave is greater than the yield strength of the material under shock conditions. In plane compressive stresses arise as the undeformed material attempts to restore the original shape of the surface.

The compressive pulse that is generated on the front face will be reflected as tensile pulse from the rear surface. If the tensile stresses are of sufficient magnitude they can lead spallation of material located at the rear surface [3]. If a thin coating is present along the rear surface, these same tensile stresses can cause coating spallation [4].

The present study evaluated the adherence of a thermal barrier coating (TBC) system consisting of (a) bond coats of either vacuum plasma-sprayed (VPS) Ni-22Cr-10Al-1Y or VPS Ni-23Co-

18Cr-12Al-0.3Y, (b) air plasma sprayed (APS) yttria stabilized zirconia (YSZ), and (c) substrates of either single-crystal (SX) Rene N5 or Mar M. In all cases the substrates were in form of 25 mm diameter disks approximately 6 mm in thickness. Typical bond coat and top coat thicknesses were 100 and 250 µm, respectively.

Figure 2 illustrates a plot of incident power density versus specimen number. Conventional and infrared photographs are included for selected samples. The infrared images were generated by placing each specimen on a hot plate maintained at 100°C (see Figure 3 for reference). For this arrangement, any cracking arising from the laser pulse was expected to disrupt the heat flow thereby lowering the measure surface temperature. Although the spallation of the coating was inhibited for power densities < 1 GW/cm^2, debond cracks were still able to form as indicated by the dark spot in the corresponding infrared image. These results that even lower power densities would be required to identify the onset of this debonding process. A final interesting observation was that the laser pulse generated at the highest power density was able to cause spallation of the bond.

Status of Milestones

(1) Develop draft plan (Annex IV proposal) for implementation of lightweight materials activity. **(Completed: 09/04)**.

(2) Complete Annex II-Subtask 13 effort and issue report. **(Draft prepared-12/04).**

Communications/Visits/Travel

None.

Publications

[1] "Implementing Agreement For A Programme Of Research And Development On Advanced Materials For Transportation Applications (IA-AMT), Strategic Plan," March 2004, available on web site IA-AMT.ornl.gov.

References

[1] P. A. Steinmann and H. E. Hintermann, "A review of the mechanical tests for thin-film adhesion." Journal of Vacuum Science Technology A, Vol. 7, No. 3, 1989, pp. 2267-2272.

[2] J. Valli, U. Makela, and A. Matthews, "Assessment of Coating Adhesion." Surface Engineering, Vol 2,.No. 1, 1986, pp. 49-53.

[3] M. Boustie, F. Cottet, Y. Chauveau, and S. A. Marta, "Spalling of Aluminum and Copper Targets by Laser Shocks," pp. 741-50 in Shock-Wave and High-Strain-Rate Phenomena in Materials, edited by M. A. Meyers, L. E. Murr, and K. P. Stadhammer, Marcel Dekker, Inc., New York, 1992.

[4] M. Boustie, E. Auroux, and J. P. Romain, "Application of the Laser Spallation Technique to the Measurement of the Adhesion Strength of Tungsten Carbide Coatings on Superalloy Substrates," Eur. Phys. J. AP, 12, 47-53 (2000).

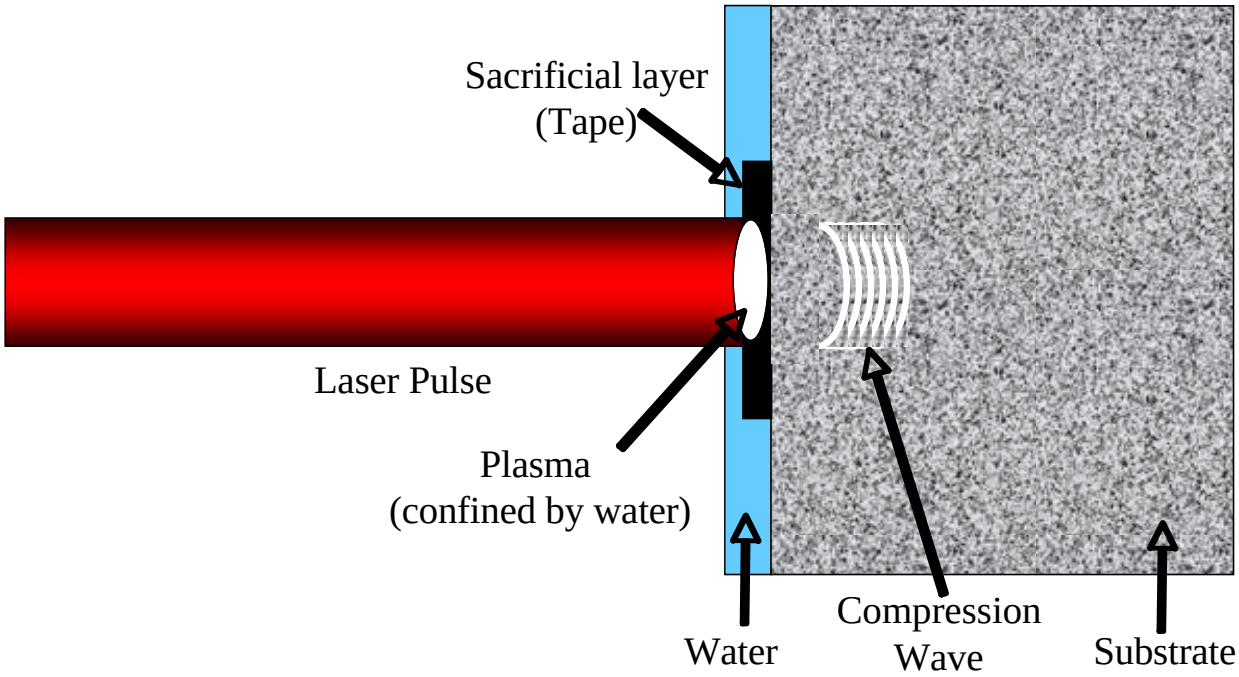

Figure 1: Schematic representation of the LSP process.

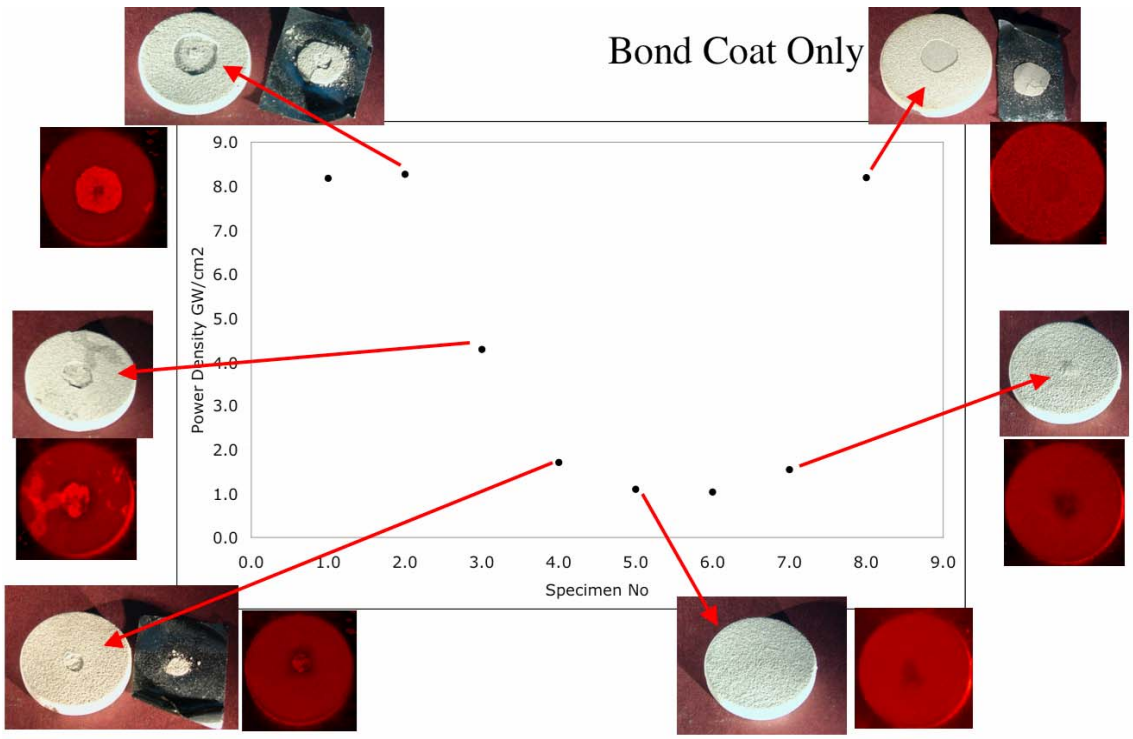

Figure 2: Graph of incident power density versus specimen number.

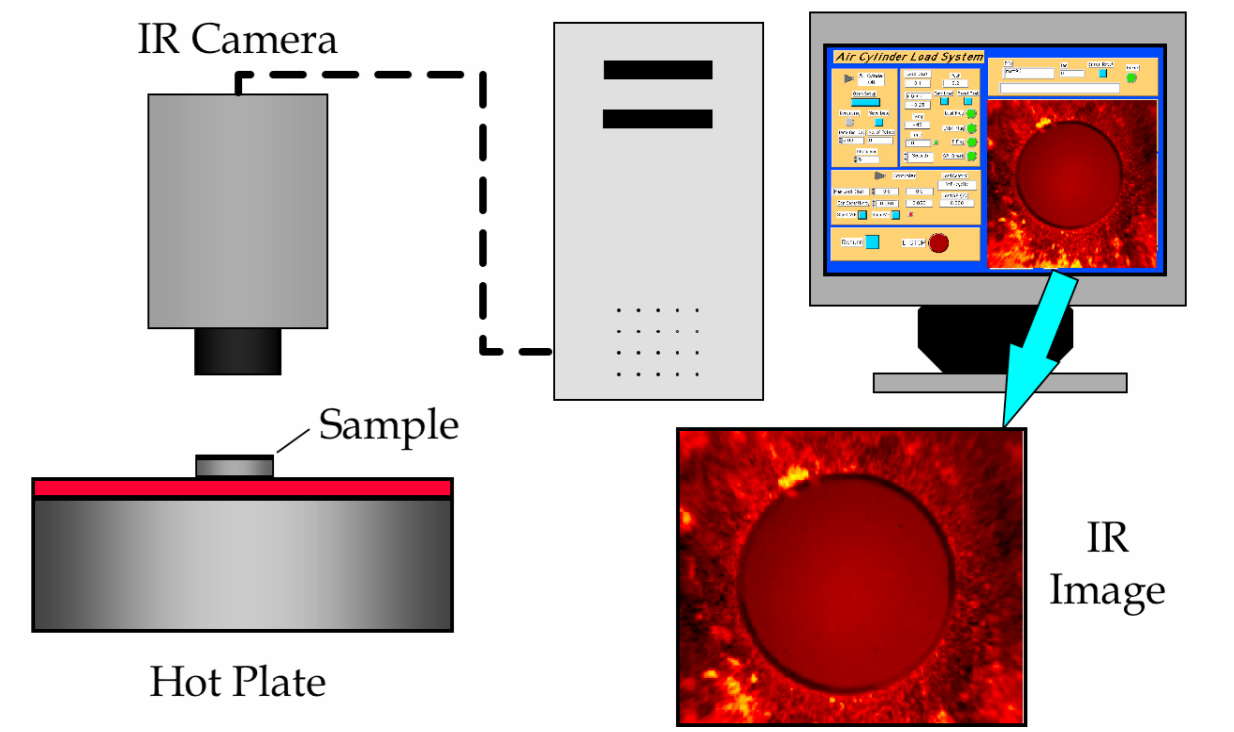

Figure 3: Schematic representation of setup used for the infrared imaging. The sample was placed on the hot plate such that the coated surface was facing the camera lens. Note that infrared image basically represents surface temperature map of the top coat.

Mechanical Property Test Development

George Quinn
National Institute of Standards and Technology

Objective/Scope

This task is to develop mechanical test method standards in support of the Propulsion Systems Materials Program. Test method development should meet the needs of the DOE engine community but should also consider the general USA structural ceramics community as well as foreign laboratories and companies. Draft recommendations for practices or procedures shall be developed based upon the needs identified above and circulated within the DOE engine community for review and modification. Round robins will be conducted as necessary. Procedures will be standardized by ASTM and/or ISO.

Technical Highlights.

1. General

Work continues on a Guide to Practice for Fractography. Some work was done to remedy a problem in the ASTM standard F 2094 for silicon nitride ball bearings. Several ASTM Committee C-28 draft standards were reviewed. A paper on fractography of machining damage in ground silicon nitride ceramics was presented in October at a fractography conference in Slovakia. A major review paper: "Design and Reliability of Ceramics, Do Modelers, Designers, and Fractographers See the Same World?" was prepared for the American Ceramic Society conference in January.

2. Fracture Toughness

No new work was done this quarter. Three inquiries were received from people in industry and academia who wanted to try to use the ASTM fracture toughness standard, C 1421, but found it difficult to understand. It is clear that that standard needs to be rewritten to make it more user-friendly.

3. Flexural Strength of Advanced Ceramics – Rectangular Specimens

No new activity this quarter. Work on this is pretty much done with the sole exception that we reviewed a preliminary final report of the results of a major Versailles Advanced Materials and Standards (VAMAS) round robin led by Dr. S. J. Cho of KRISS, Korea. This project is focusing on the effects of humidity on flexural strength.

4. Fractography

Work continued on a NIST user-friendly "Guide to Best Practice" for fractographic analysis. Several case studies were written up and illustrations prepared as examples of applied fractographic analysis. One of the case studies is the excellent work done by the Ford Motor Company in the early 1980's on a model silicon nitride gas turbine rotor that was spun to failure in a hot test rig. This work was done to intentionally check the veracity of their design codes and databases. Mr. Quinn followed up the Ford work by reconstructing two of their burst rotors and finding the exact initiation sites. This is an excellent case of how fractographic analysis can aid design code development and can help close the loop of design, testing, interpretation and redesign.

5. Flexural Strength Testing of Cylindrical Ceramic Specimens
No activity this quarter. We are getting inquiries about this and spent some time preparing a summary brief report on the status of this work with some suggestions. This brief package will be sent to future inquirers upon request. A good summary of the status of the project with some preliminary data was prepared for distribution

6. Split Cylinder Flexural Strength Testing
We will resume flexural strength testing of split cylinder or segmented cylinder rods in the Spring and Summer of 2005 when a student comes to assist.

7. Hardness
A paper on Standard Reference Material 2831, Vickers Hardness of Ceramics and Hardmetals was prepared and given at the international HardMeko conference in November 2004.

8. Diametral Compression
No progress this quarter.

9. Other
Revisions to ASTM Standard F 2094, Specification for Silicon Nitride Ball Bearings
Following up work started last quarter, we continued to work on the revision to this standard. It was adopted in 2001 by ASTM Committee F-34. Over the years we have contributed a lot to the development of this standard, which has aided the commercialization of silicon nitride ball bearings. There were a few loose ends in the document that needed polishing. One of the lose ends was a questionable table on required flexural strengths for the three grades (materials class) of silicon nitride specified in the standard. The standard specifies average flexural strengths, which could be measured by either 3-point or 4-point flexure, and either by the USA-ASTM-European methods or by the Japanese Industrial Standard method. Unfortunately, these methods all have different effective volumes and effective surfaces so the numbers should vary with the test procedure. The table of strength numbers was listed in the last quarterly report. Bill Mandler of Enceratec submitted a new table to the ASTM F-34 membership for ballot in November, but it used all old 3-point strength values as the baseline for table conversion. Ceradyne and NIST voted negative on the draft with the suggestion that the table would be better if the anchor values were the 4-point values and the 3-point values adjusted accordingly. The whole affair was discussed at the F-34 meeting in Washington, DC in November where an agreement could not be reached. No attempt was made to find the negative ballots nonpersuasive. In subsequent weeks there was a considerable exchange of messages and proposals between the interested parties. We also researched back 20 years to the origins of some of the numbers and they were traced to SKF in the Netherlands. A compromise solution was reached that will now be submitted for ballot. It will use some 3-point values for the baseline and some 4-point values in other instances. The timing is important since we have subsequently learned that the Japanese delegation will formally submit a New Work Item proposal to ISO Technical Committee TC 206 very soon on this matter. This level of activity is a sign that commercialization of silicon nitride bearings is progressing very well.

<u>Status of Milestones</u>

412149	Prepare ballot-ready first ASTM draft of cylindrical rod flexure strength test	Overdue
412151	Prepare review paper on flexural testing of cylindrical rods.	Overdue, Ongoing work on error analysis

Communications/Visits/Travel

G. Quinn attended an ASTM meeting of Committees F-34, Bearings and also Committee E-28 on hardness in Washington in November 2004. He also gave a presentation at the HardMeko conference held at the same time.

Mr. Quinn also gave an invited presentation on machining cracks in silicon nitride at the fractography of Advanced Ceramics conference in Slovakia in October.
We had contact with several groups were on the status of flexural strength testing of round rods.

Publications and Presentations

1. G. D. Quinn, R. J. Gettings, and L. K. Ives, "A Standard Reference Materials for Vickers Hardness of Ceramics and Hardmetals," presented at and to be published in the proceedings of the IMEKO Hardness Conference, NIST, 11-12 Nov. 2004.
2. G. D. Quinn, L. K. Ives, and S. Jahanmir, "Machining Cracks in Finished Ceramics," presented at and to be published in the proceedings of the conference on *Fractography of Advanced Ceramics, II*, ed. J. Dusza, TransTech Publ., Zurich, 2005.

Surface Modification of Engineering Materials for Heavy Vehicle Applications

Stephen Hsu
National Institute of Standards and Technology

Objectives

- Organize an international cooperative research program on an integrated surface modification technology under the auspice of the International Energy Agency (IEA)
- Design and identify surface features and patterns that can achieve friction reduction and enhanced durability for heavy duty diesel engine components.
- Develop understanding and appropriate models to explain the texturing effects on frictional characteristics. Develop appropriate thin films and coatings to achieve synergistic and complementary relationship with texturing to enhance performance.
- Discover and develop surface chemistry for protecting the films and coatings which work in synergy with the coatings.

Approach

- Determine the effect of size, shape, pitch, and patterns of surface textural features on friction under 1) high speed, low load regime; 2) high load high speed regime; 3) high load low speed regime.
- Develop cost effective fabrication technologies for creating surface textural features on various surfaces including metals, ceramics, and coatings.
- Develop test methodology to measure the effects of the textures on friction
- Conduct research to develop an integrated system approach to combine the best practices in thin films, coating, and surface chemistry for performances unrealizable by individual approach alone.
- Concurrently, organize an international cooperative research program under the auspice of the International Energy Agency (IEA) to pool resources and share this energy conservation technology worldwide.

Accomplishments this quarter

- Establish linkage with COST 532 (European Cooperative Research consortium on Triboscience and Tribotechnology). Made a presentation to the management committee in Ghent, Belgium in Oct. 2004 and the management committee voted to participate in the IEA surface texturing task. The consortium consists of some thirty organizations from 14 countries in Europe.
- Obtained China as a participant in the IEA surface texturing task. The participants are from the Chinese Academy of Sciences, Lanzhou Institute of Chemical Physics. I made a presentation to the members of the Chinese Institute of Tribology in Nov. 2004 in Xian, China.
- Demonstrated for the first time that friction reduction from boundary lubrication regime to a friction level typical of hydrodynamic lubrication regime can be achieved using steel surfaces. Now we have demonstrated that surface texturing can indeed be used in practical systems, at least in principle, to achieve energy savings.

Introduction

Frictional losses are inherent in most practical mechanical systems. The ability to control friction offers many opportunities to achieve energy conservation. Over the years, materials, lubricants, and surface modifications have been used to reduce friction in automotive and diesel engine applications to promote energy efficiency. However, in recent years, progress in friction reduction technology has been slow since much inefficiency has been eliminated already. A new avenue is needed.

Recently, laser ablated dimples on surfaces have shown friction reduction properties and have been demonstrated successfully in conformal contacts such as seals where the speed is high and load is low. The effect of dimples on friction reduction appears to depend on dimple size, pattern of dimples, and density of dimples on the contacting surfaces. However, this friction reduction property has not been shown to be effective under high load, low speed conditions. Nevertheless, the use of surface texture has opened a new avenue to explore friction reduction in engine applications.

The objective of this project, therefore, is to explore the possibility of surface texture designs to achieve friction reduction in energy transmission devices in conjunction with thin films and coatings under a broad range of contact conditions and develop design guidelines for technology implementation world wide.

To achieve world wide energy conservation, a concomitant international cooperative research under the auspice of the International Energy Agency will be launched to pool resources from various countries to accelerate this technology development. Towards this end, UK, Germany, Finland, Sweden, Israel, and Japan have agreed to participate under the IEA annex IV on this activity.

Approach

During the last fiscal year, experiments were conducted to examine various surface textures on steel surfaces using photolithography and chemical etching. Using the same area coverage (% of area occupied by the surface textural features), surface features such as grooves, triangles, ellipses, circles were compared under high speed low load conditions similar to those used by surface seals. Results indicated that 1) surface feature shape had great influence on friction reduction; 2) friction reduction also depended strongly on the orientation of the surface features with respect to the direction of sliding. This suggested that conventional theory of hydrodynamic lift was not adequate to explain these observations. A new theory is needed. Therefore, an in situ video camera was set up to observe the lubricant flow pattern in a single dimple under different operating conditions. The magnification, however was inadequate to clearly define the detailed flow patterns to deduce the friction reduction mechanism, we are in the process of purchasing a high speed high resolution video camera system to be installed this year to observe directly the flow patterns. A modeling was also initiated this quarter to examine contact mechanics model for a single dimple.

For high load low speed conditions, the same surface textural features yielded higher friction than untextured surfaces due to increased surface roughness. A collaborative effort with Northwestern University using a sophisticated elastohydrodynamic friction model confirmed

our experimental observations. Basically, under boundary lubricated conditions (high load low speed), the edge stresses around the dimple increase friction rather than decrease friction. A new surface textural feature with an inclined plane at the bottom of the feature was developed using a mechanical scribing technique by a triboindenter. Because of the triboindenter had limited load range, soft metals such as aluminum, copper, and brass were used. Since the pin-on-disk apparatus was limited by load, a four-ball wear tester with the configuration of ball-on-three-flat was used to generate high contact pressures. Using this kind of features, elongated dimples on soft metals were successful in achieving significant friction reduction under high contact pressures exceeding one GPa. This quarter, we achieved high load capacity of the triboindenter so we conducted a series of experiments on steel surfaces to see whether surface textures could lower the friction. Another objective was to start the experiment in the boundary lubrication regime and observe friction reduction by the textured surface. The soft metals had low friction coefficients to begin with.

Technical highlight

When we used hard metals such as 52100 steel, the initial high contact pressure caused severe wear damaging the surface textures and the friction reduction results were erratic. To overcome this issue, we developed a wear-in procedure to create a smooth crater surface of approximately 0.5 mm diameter and the texture was fabricated on the surface of this crater. This way, a controlled initial contact surface was created to avoid wear-in. The surface textures were applied to this slightly curved surface using the high load triboindenter. The process was labor intensive and it took about one week to texture the three bottom disks for a single experiment. A special lubricant was used for this set of experiment. Previously, we had used either white oil or commercial motor oil. The white oil caused severe wear under this set of conditions while the commercial motor oil contained friction modifier additives which made the data analysis difficult. To fully evaluate the friction reduction capability of the surface textures, white oil with an antiwear additive and an antioxidant was blended for this series of experiments. This lubricant allowed wear prevention and stable operation without prejudicing the friction results.

A series of experiments designed to measure the effect of crater depth and feature density was conducted using hard steel materials (52100 steel on 52100 steel). The surface textural features were elliptical in shape and the crater depth ranged from 0.1 micron to 0.5 micron and the texture density was varied 4 times. Table 1 illustrated the experimental design.

Table 1. Experimental design

Feature depth/ Number of features	0.13 µm ± 0.02 µm	0.23 µm ± 0.02 µm	0.50 µm ± 0.05 µm
9 x 13	Texture 11		Texture 13
12 x 18		Texture 22	
17 x 26	Texture 31		Texture 33

The load was varied from 10 Kg to 30 Kg and the speed was varied from 500 rpm (0.19 m/s) to 3500 rpm (1.34 m/s). The apparent initial contact pressures ranged from 200 MPa to 600 MPa with the asperity contact pressure considerably higher than the apparent contact pressure.

All of the initial coefficients of friction for the untextured surfaces were from 0.08 to 0.1 signifying that the test condition was in the boundary lubricated condition.

The data is summarized in Figure 1 using a Stribeck curve format even though under boundary lubrication conditions, this format is really not applicable.

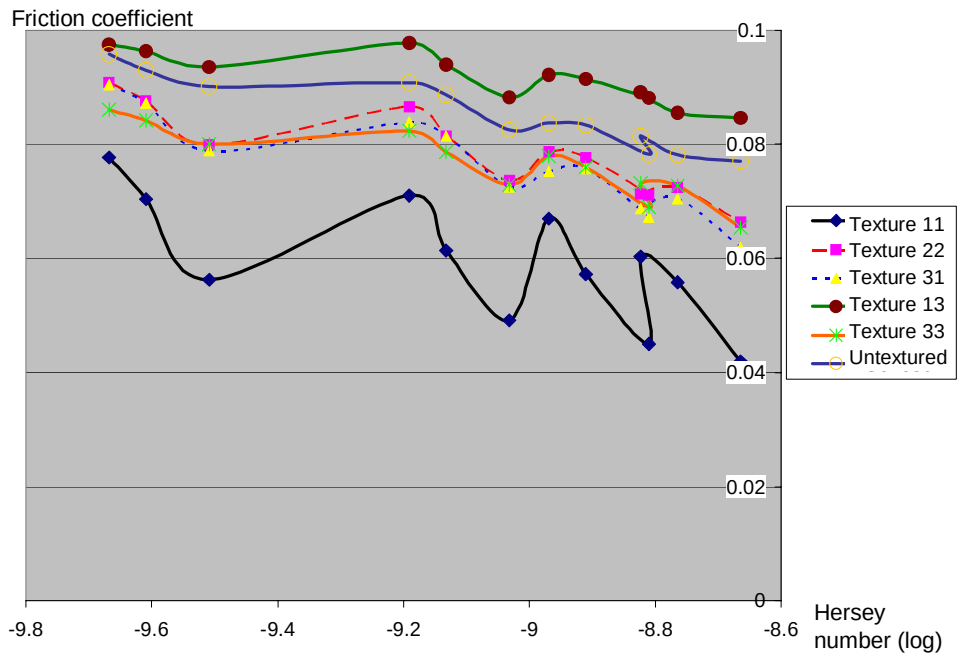

Fig. 1. Comparisons of various surface texture patterns and their friction reduction

The Hersey number used in Figure 1 is defined by:

$$H_s = \frac{\eta\omega}{p}$$

Where η = dynamic viscosity

ω = rotational speed (rps)

p = contact pressure (Pa) – Hertz elastic contact pressure: $p = \frac{2}{3}\left(\frac{6WE^{*2}}{\pi^3 R^2}\right)^{1/3}$

W = load on each disk: $W_t / \sqrt{6}$

$$\frac{1}{E^*} = \frac{1-\nu_1^2}{E_1} + \frac{1-\nu_2^2}{E_2}$$

R = ball radius

As illustrated in Fig. 1, texture 11 achieved the best friction reduction ranging from 20 to 30% as compared to the untextured surface. Texture 13 consistently shows higher friction coefficients than the baseline. Texture 22 achieved about 10% friction reduction and texture 31 and 33 have approximately the same results. This suggests that fewer features and deeper depth cause friction to rise above the baseline case. Increasing feature density (pattern 31 and 33) helps but the optimum may be in the shallow textural features. This result is preliminary in nature and many of the details need to be confirmed in further experiments.

While the conclusion is somewhat tentative, this is the first set of experimental results that demonstrates for the first time that boundary lubricated friction can be reduced by using surface textures.

Publications/Presentations

Presentations:

S. M. Hsu, "An integrated approach to design intelligent surfaces for heavily loaded contacts," International Joint Tribology Conference, Ponte Vedra, FL., Oct. 27-29, 2003.

S. M. Hsu, "An integrated surface texture design with surface modification techniques and thin lubricating films," Smart Surfaces in Tribology: Advanced additives and structured coatings Conference, Zurich, Switzerland, Sept. 10-12, 2003.

S. M. Hsu, "An integrated surface technology international program under IEA" International Energy Agency Executive Committee meeting, Oakland, CA. Oct. 20-23, 2003.

S. M. Hsu, "Surface texturing under boundary lubrication for friction control," STLE annual meeting, Toronto, Canada, May 17-20, 2004.

Jorn Larson Basse, X. Wang, L. Ives, S. M. Hsu, "Some friction experiments with textured surfaces," Nordic Symposium on Tribology, Troms, Norway, June 2004.

Jorn Larson Basse, X. Wang, L. Ives, S. M. Hsu, "Some friction experiments with dimpled surface texture," The fourth China International Symposium on Tribology, Xian, China, Nov. 8-11, 2004.

S. M. Hsu, "An Integrated surface modification technique to control friction: a new paradigm," Keynote speaker, the 4th China International Symposium on Tribology, November 8-11, 2004, Xian, China.

Y. Chae, X. Wang, S. M. Hsu, "The size effect of surface texture on lubricated friction," The First International Conference on Advanced Tribology, Singapore, Dec. 1-3, 2004.

Publications:

Jorn Larson Basse, X. Wang, L. Ives, S. M. Hsu, "Some friction experiments with textured surfaces," Proceedings of Nordic Symposium on Tribology, Troms, Norway, June 2004.

X. Wang, S. M. Hsu, “An Integrated surface modification technique to control friction: a new paradigm,” Keynote paper, the 4th China International Symposium on Tribology, November 8-11, 2004, Xian, China.